DEVELOPMENT OF ULTRASOUND AND PHOTOACOUSTIC IMAGING TOOLS FOR TRACKING OF CELLS AND PARTICLES

A Dissertation
Presented to
The Academic Faculty

By

Kelsey Paige Kubelick

In Partial Fulfillment
of the Requirements for the Degree
Doctor of Philosophy in the
Wallace H. Coulter
Department of Biomedical Engineering

Georgia Institute of Technology
Emory University
May 2020

DEVELOPMENT OF ULTRASOUND AND PHOTOACOUSTIC IMAGING TOOLS FOR TRACKING OF CELLS AND PARTICLES

Approved by:

Dr. Stanislav Y. Emelianov, Advisor
School of Electrical and Computer Engineering
The Wallace H. Coulter
Department of Biomedical Engineering
Georgia Institute of Technology
Emory University School of Medicine

Dr. Eleanor Donnelly
School of Medicine
University of Limerick

Dr. C. Ross Ethier
The Wallace H. Coulter
Department of Biomedical Engineering
Georgia Institute of Technology
Emory University School of Medicine

Dr. Andrés García
The George W. Woodruff
School of Mechanical Engineering
Georgia Institute of Technology

Dr. Francisco Robles
The Wallace H. Coulter
Department of Biomedical Engineering
School of Electrical and Computer Engineering
Georgia Institute of Technology
Emory University School of Medicine

Dr. Krishnendu Roy
The Wallace H. Coulter
Department of Biomedical Engineering
Georgia Institute of Technology
Emory University School of Medicine

Date Approved: December 13, 2019

To my mother and father with the greatest love

ACKNOWLEDGEMENTS

My family frequently uses the saying, “Be thankful for what you have. Be thankful for what you don’t have.” Reflecting on the last five years, I am thankful for all of the wonderful opportunities and lessons learned throughout graduate school. Most importantly, I am thankful for the support of countless colleagues, friends, and family.

I would like to acknowledge the incredible support of my advisor, Stanislav Emelianov. I could not have succeeded without his guidance. I am most thankful for his encouragement to pursue research directions and interests outside of my comfort zone. While I loved living in Austin, it was a wonderful experience, opportunity, challenge, and change to relocate to Atlanta. Furthermore, I would like to thank all members, past and present, of the Ultrasound Imaging and Therapeutics Research Laboratory. Research contributions of specific individuals are highlighted following each chapter.

I would like to acknowledge the support of my thesis committee members, Drs. Eleanor Donnelly, Ross Ethier, Andrés García, Francisco Robles, and Krishnendu Roy. I appreciate their advice throughout this process, and their insights have greatly improved this research.

I have had the privilege of working with many excellent collaborators. I specifically would like to thank Dr. Ross Ethier, who has been substantially involved in my research from the start. I specifically would also like to thank Eric Snider, a previous graduate student in the Ethier Lab, who I greatly enjoyed working with.

Outside of my research, I have had many wonderful experiences working with the Georgia Tech Capstone Program. I specifically would like to thank Profs. James Rains and James Stubbs for giving me opportunities to pursue other professional outlets during my time at Georgia Tech.

Lastly, I would like to thank my friends and family for their unconditional support. Specifically, I would like to thank my mom and dad. There are not enough words to express my gratitude for their encouragement, and I am eternally grateful to always have them in my corner during any pursuit, big or small.

TABLE OF CONTENTS

LIST OF TABLES

LIST OF FIGURES

LIST OF ABBREVIATIONS

2D	Two-dimensional
3D	Three-dimensional
a.u.	Arbitrary units
AgQ	Aggregating/quenching
AI	Anterior iris
AuNR	Gold nanorod
AuNS	Gold nanosphere
bPEI	Branched polyethyleneimine
CFSE	Carboxyfluorescein succinimidyl ester
CPE	Ciliary pigmented epithelium
CT	Computed tomography
DEVD	Aspartate-glutamate-valine-aspartate
DIUF	Deionized ultra-filtered
DMEM	Dulbecco's modified eagle medium
FBS	Fetal bovine serum
Hb	Deoxygenated hemoglobin
HbO_2	Oxygenated hemoglobin
IACUC	Institutional animal care and use committee
IOP	Intraocular pressure
iPSC	Induced pluripotent stem cell
IVIS	*In vivo* imaging system

LLS	Linear least squares
MCOCT	Molecular contrast optical coherence tomography
mPLP	micro-sized pathogen-like particle
MRI	Magnetic resonance imaging
MSC	Mesenchymal stem cell
MSME	Multi-slice multi-echo
nPLP	Nano-sized pathogen-like particle
OCT	Optical coherence tomography
OD	Optical density
OPO	Optical parametric oscillator
OR	Operating room
PA	Photoacoustic
PBNC	Prussian blue nanocube
PBS	Phosphate buffered saline
PDI	Polydispersity index
PET	Positron emission tomography
PI	Posterior iris
PLGA	Poly(lactide-co-glycolic acid)
PLP	Pathogen-like particle
PVA	Poly-vinyl alcohol
RPE	Retinal pigmented epithelium
SCS	Suprachoroidal space
sPA	Spectroscopic photoacoustic

SPION	Superparamagnetic iron oxide nanoparticle
SQUID	Superconducting quantum interference device
TE	Echo time
TM	Trabecular meshwork
TR	Repetition time
US	Ultrasound

SUMMARY

Development of novel therapies relies heavily on histology to evaluate outcomes. While histology provides detailed information at the molecular level, drawbacks include highly invasive, destructive sample preparation. Clinical translation of novel therapies would be expedited by further developing minimally invasive, longitudinal imaging methods.

Combined ultrasound (US) and photoacoustic (PA) imaging augmented with contrast agents is an excellent option to address this need. Complimentary information provided by US/PA imaging allows morphological, functional, and cellular/molecular assessment of tissue. US signals are produced by backscattering of acoustic waves. Generation of PA signals relies on the photoacoustic effect, where acoustic waves are produced upon absorption of light. Based on this unique contrast mechanism, a variety of endogenous and exogenous absorbers exist for PA imaging to suppress background signals and facilitate molecular, cellular, or tissue-level imaging.

This thesis describes development of a US/PA imaging toolbox, consisting of contrast agents, imaging hardware, imaging protocols, and detection algorithms, that can be customized for variety of applications where longitudinal, *in vivo* imaging of specific cells or particles is beneficial. To demonstrate versatility, these US/PA imaging tools were developed and combined in different ways to facilitate implementation in three distinct applications: 1) stem cell monitoring in ophthalmology to aid development of glaucoma therapies; 2) intra- and post-operative monitoring to guide stem cell therapies of the spinal cord; and 3) monitoring particle trafficking to inform vaccine design. Although the

applications investigated were extremely different, common themes were identified throughout, highlighting versatility of the US/PA imaging toolbox and similar research needs for later development. Overall, the tools developed here lay the foundation for design of customized imaging platforms in future applications.

CHAPTER 1. INTRODUCTION

Development of novel therapies relies heavily on histology to evaluate outcomes. While histology provides detailed information at the molecular level, drawbacks include highly invasive, destructive sample preparation.[1–3] As a result longitudinal monitoring is challenging, making it difficult to fully understand therapeutic outcomes. Clinical translation of novel therapies would be expedited by further developing minimally invasive, longitudinal imaging methods for tracking.

Currently many imaging technologies exist at the preclinical or clinical stage to address this need, including magnetic resonance imaging (MRI), x-ray/computed tomography (CT), optical imaging, positron emission tomography (PET), and ultrasound (US) imaging. MRI has been widely used for longitudinal, *in vivo* monitoring of stem cells for a variety of neural and vascular applications, including stroke,[4] spinal cord injury,[5] and myocardial infarction.[6] Bioluminescence is an excellent optical method for small animal cellular-level imaging.[7,8] CT is best-suited for monitoring structural and anatomical changes, but gold nanoparticles have been used to label stem cells and T-cells for tracking.[9,10] PET is often employed to monitor cell function, where uptake of fluorodeoxyglucose, a glucose analog that generates PET contrast, is an indicator of cell metabolism.[2,11]

In the above examples, each modality was employed based on individual advantages and drawbacks. Compromises are always made between resolution, sensitivity, acquisition speed, penetration depth, contrast, safety, and cost. MRI allows high spatial resolution, non-ionizing, whole body imaging, but it suffers from high cost and slow image

acquisition. CT also allows high spatial resolution, whole body imaging, but use of ionizing radiation raises safety concerns. PET is an excellent option for highly sensitive molecular imaging; however, spatial resolution is extremely poor. Thus, PET cannot provide detailed information on localization for tracking applications. Optical methods allow high sensitivity, high resolution, high contrast molecular imaging, but *in vivo* monitoring is hindered by limited penetration depth.[2,12]

The ideal qualities of a longitudinal, *in vivo* tracking platform include high spatial resolution, high contrast, high sensitivity, safe, deep, real-time imaging to facilitate tracking of cells and particles in a variety of scenarios. Another desirable feature is the ability to monitor functional outcomes at the molecular, cellular, or tissue-level. Overall, no single modality is perfect for addressing all of these requirements. Instead, multiple modalities can be combined to provide complimentary information and create a synergistic approach to develop cell and particle trafficking platforms. Combining optical and acoustic methods is an excellent option based on the desired features listed above. One specific example is ultrasound-guided photoacoustic (PA) imaging.[13–15] In previous work, US/PA imaging has been successfully implemented in a few examples of tracking cells and particles *in vivo.*[16–18] This thesis expands on this work by describing development of a versatile US/PA imaging toolbox that can be applied to wider range of applications where tracking cells and particles is desired to aid development and translation of novel therapies.

1.1 Overview of ultrasound and photoacoustic imaging

Ultrasound is widely used in clinic to assess anatomy and tissue function. Advantages include portability, low cost, adaptable resolution, deep imaging, and safety. Real-time imaging also makes ultrasound appealing for longitudinal monitoring

applications. Ultrasound signals are generated by backscattering of acoustic waves due to differences in acoustic impedance, a tissue property that describes resistance to acoustic wave propagation.[19] However, all soft tissues are primarily water- and fat-based with similar acoustic properties. As a result different tissues have similar acoustic impedance. Thus, ultrasound suffers from inherently poor contrast, which hinders exclusive use of ultrasound for tracking cells and particles. However, photoacoustic imaging, an analog of ultrasound, can address this shortcoming.

PA imaging combines the best qualities of acoustics and optics to provide high contrast, high resolution functional information at imaging depths of several centimeters, and absorption-based contrast of PA imaging compliments scattering-based contrast of ultrasound. PA imaging relies on the photoacoustic effect, where acoustic waves are produced upon absorption of light. When an optical absorber is irradiated by a nanosecond pulsed laser, heat deposition causes rapid thermoelastic expansion of the surrounding tissue to produce an acoustic wave. The resulting wave can be detected using a traditional ultrasound imaging transducer, which simplifies integration of this multi-modal approach.[12,13,20] Together with ultrasound, the multi-modal approach provides combined anatomical and functional information for longitudinal tracking of cells and particles.

The use of an optical absorber is a key requirement for photoacoustic imaging. A wide variety of endogenous and exogenous optical absorbers exist and serve as PA contrast agents.[15] Endogenous absorbers include melanin, oxygenated hemoglobin, and deoxygenated hemoglobin. Exogenous absorbers can be broadly classified as dyes, nanoparticles, or composites. There are countless available combinations within these groups. For example, nanoparticle size, shape, and material can be customized.

Nanoparticle size can range from several nanometers to micrometers. Nanoparticle shapes include shells, rods, cubes, cages, spheres, plates, stars, etc. Nanoparticle materials include silver, carbon, gold, and copper. Different combinations of these properties result in a unique optical absorbance spectrum, and in turn, produce a distinct PA spectrum, which can ultimately be distinguished from background absorbers with multi-wavelength PA imaging techniques and spectroscopic analysis.[21–26]

Multi-wavelength PA imaging and spectroscopic analysis can distinguish multiple optical absorbers in heterogeneous tissue, where the PA signal at each pixel is a superposition of individual PA signals from endogenous and exogenous absorbers.[27] The foundation of spectroscopic PA imaging is illustrated in Figure 1. The PA spectrum of melanin, blood, and gold nanorods all have distinct optical signatures. However if a PA image was acquired with a single wavelength, for example 800 nm, it would be impossible to distinguish all species since each absorber simultaneously contributes to the PA signal. This problem is mathematically equivalent to having multiple unknowns and one equation. By using many wavelengths and spectroscopic analysis, it becomes possible to distinguish multiple absorbers based on the unique absorbance spectrum of each species.

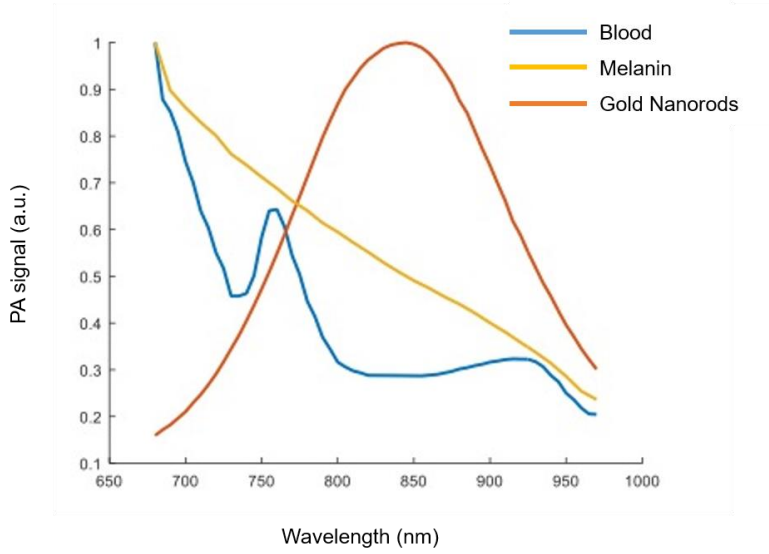

Figure 1. PA spectrum of blood (blue line), melanin (yellow line), and gold nanorods (orange line). The PA spectrum of each absorber corresponds to the absorbance spectrum.

Determining multi-wavelength PA imaging protocols, tailoring detection algorithms and spectroscopic analysis techniques, and development/synthesis of exogenous contrast agents, are critical aspects of developing longitudinal US/PA imaging platforms. These individual US/PA imaging tools can be developed to create a universal toolbox for tracking cells and particles, and individual tools can be combined in different ways to create custom imaging platforms that are relevant to many applications.

This thesis describes development of a US/PA imaging toolbox and demonstrates use in three unique applications: 1) stem cell monitoring in ophthalmology to aid development of glaucoma therapies; 2) intra- and post-operative monitoring to guide stem cell therapies of the spinal cord; and 3) monitoring particle trafficking to inform vaccine design. In spite of the clear differences in these application, the same basic approach was used throughout and similar tools were required:

- Spectroscopic properties of imaged tissues were evaluated to determine the optical properties of an appropriate exogenous contrast agent.
- The contrast agent was synthesized.
- An approach was determined to label the cell or particle with the contrast agent.
- A US/PA imaging protocol was developed to detect the PA signal of interest.
- Images were post-processed using spectroscopic analysis and other algorithms.

The thesis is organized as follows. The remainder of Chapter 1 describes the motivation for addressing the above applications. Chapters 2 and 3 describe the ophthalmic research. Chapter 4 describes the spinal cord research. Chapter 5 describes the vaccine particle research. Each chapter concludes with a section on future work specific to each application. Chapter 6 describes common conclusions and future needs identified throughout to highlight overarching themes for continued research. Overall results demonstrate versatility of the platform and lay the groundwork for further development of the US/PA imaging toolbox.

1.2 Monitoring stem cell therapies

Stem cell therapy for regenerative medicine holds great promise for many applications, especially those with few treatment options. In spite of significant research efforts, few stem cell therapies have reached clinical translation. While there are many challenges to address, one major limitation is lack of knowledge of stem cell behavior *in vivo*.[2,28] At the research stage, histology is the primary tool for evaluating therapy progression, but assessment at multiple time points is challenging. Thus, development is inherently inefficient as histology provides an incomplete view of experimental success or

failure. At the clinical stage, longitudinal monitoring is critical for translation by providing clinicians with feedback on therapy progression to inform modifications and increase the likelihood of a positive outcome. For these reasons, there is a critical need for *in vivo* longitudinal monitoring of stem cell therapies, which can be addressed by US/PA imaging tools. Previous researchers have demonstrated US/PA imaging to monitor stem cell therapies and macrophage interactions in muscle using gold nanospheres (AuNSs) and gold nanorods (AuNRs).[16,17,28,29] The current work seeks to extend these techniques to new applications in ophthalmology and the spinal cord. Both applications have a new set of requirements to address, and results can extend beyond these applications and even beyond stem cell tracking.

1.2.1 Monitoring stem cells in ophthalmic applications

Glaucoma is the second leading cause of blindness in the world, estimated to impact more than 70 million people.[30] Disease progression is associated with cell death at the trabecular meshwork (TM), a fluid drainage tissue in the anterior eye.[31–33] TM dysfunction can result in increased intraocular pressure (IOP), a frequently observed characteristic of the disease. However, there is no cure for glaucoma, and existing treatment methods focus on symptom management.

A promising therapy is to deliver stem cells to the TM to regenerate the tissue and restore normal function. Both induced pluripotent stem cells (iPSCs) and mesenchymal stem cells (MSCs) have been investigated in several different models of glaucoma.[34–37] Results showed stem cells decreased IOP and restored TM function. However conclusions on how stem cells interacted with the environment to induce a therapeutic response were contradictory.[36,37] One study found MSCs reduced IOP over 20 days, but histology showed

no MSCs were present in the TM by 96 hours post-delivery. [36] In another study, IOP was reduced immediately following MSC delivery, but increased again after 15 days. However, in this case, histology detected MSCs in the TM and other anterior tissues for 23 days post-delivery.[37] It is difficult to explain these conflicting results with information from a single time point. Many questions could be answered if a longitudinal monitoring technique was available to monitor the stem cells.

A variety of longitudinal imaging technologies exist for ophthalmic applications. In particular, optical coherence tomography (OCT) is widely used in clinic. OCT is analogous to ultrasound, except contrast is based on optical scattering. [38,39] Thus, OCT has similar disadvantages to ultrasound, and poor contrast limits the use of OCT to monitor stem cell therapies. Beyond stem cell monitoring, there is a broader need for anterior segment and specifically TM imaging technologies, which are currently lacking.[31] In general, purely optical methods prove challenging for TM imaging due to light attenuation from melanin absorption and scleral scattering.

As a combined optical and acoustic method, PA imaging addresses both needs: 1) it is a favorable option for anterior segment imaging because it will be less affected by light attenuation compared to purely optical methods; and 2) high contrast from optical absorption allows stem cell detection. PA imaging has been demonstrated in the anterior and posterior segments, but current research is limited.[40,41] In addition, ultrasound imaging is already used in clinic for ophthalmic applications and therapeutic use of lasers is common, which simplifies the addition of PA imaging.[42] For these reasons, combined US/PA imaging is an excellent option to monitor stem cells in the anterior segment to aid development of novel glaucoma therapies.

1.2.2 Stem cell monitoring in the spinal cord

Amyotrophic lateral sclerosis (ALS) is a neurodegenerative disease of the brain and spinal cord, characterized by degeneration of motor neurons. Stem cell therapies are of interest for treating ALS due to their ability to directly and indirectly regenerate tissue through differentiation into motor neurons or inducing a pro-regenerative response by secreted factors.[43] Significant research efforts have shown some success in preclinical and clinical studies, but major hurdles remain.[44–46] Similar to issues described in using stem cells for glaucoma treatment, there is a limited understanding of the therapeutic mechanism, including stem cell migration patterns and interactions with the microenvironment. On a more basic level, it is difficult to know if stem cell delivery was successful.

The most promising delivery method is direct injection of the MSCs into the gray matter of the ventral horn, where cell bodies of motor neurons are localized. Direct injection is risky, but increases likelihood of a successful outcome.[45–47] Great care needs to be taken during the injection, as a small misstep could have dire consequences. Pre- or intraoperative MRI can help guide the injection. Pre-operative MRI can be used to determine injection coordinates, but this has minimal benefit because surgeons may need to adapt coordinates during the procedure. Intraoperative MRI is expensive, challenging to implement, and many research and clinical facilities will not have this system.

For these reasons, alternative imaging methods are needed to intraoperatively guide the MSC injection in real-time. To allow direct injection into the spinal cord, a lumbar laminectomy is performed.[44,45,47] A convenient acoustic and optical window is created by removing the overlying bone (laminae) to allow US/PA imaging. Spectroscopic PA

imaging can provide additional guidance by helping to navigate vasculature and distinguish white vs. grey matter.[48,49] Lastly, immediate feedback on injection success can be provided by labeling stem cells with optical absorbers to allow PA imaging.

Post-operatively, longitudinal monitoring is needed to monitor MSCs as therapy progresses. Longitudinal information can provide researchers with a better understanding of stem cell behavior to assist with therapy development or can provide physicians with feedback on therapy progression. MRI has been used for tracking stem cells tagged with superparamagnetic iron oxide nanoparticles (SPIONs) in the spinal cord and brain.[50–52] Significant stem cell migration was observed and varied according to injection site and type of injury. MRI has been able to detect stem cells for several months post-injection.[50,51] One study found a detection limit of 1000 cells *in vitro*.[50]

Though MRI is the gold standard for central nervous system (CNS) imaging, lengthy image acquisition time makes real-time assessment of three-dimensional volumes difficult. US/PA imaging can be a valuable research tool for monitoring stem cell therapies in the spinal cord. US/PA imaging allows real-time imaging and acquisition of three-dimensional volumetric images. Furthermore *in vitro* studies of AuNS-tagged-MSCs also showed 200 cells could be detected with PA, meaning more sensitive detection may be possible.[53] Overall, longitudinal stem cell tracking in the spinal cord using US/PA imaging address shortcomings of existing methods. US/PA imaging may assist in therapy development and translation by providing a tool for intraoperative and post-operative guidance of stem cell therapies.

1.3 Monitoring Particles

US/PA imaging platforms can similarly be developed for longitudinal monitoring of particles using the same research approach and tools. By labeling a particle of interest with an optical absorber for PA imaging, particles can be tracked using multi-wavelength PA imaging and spectroscopic analysis. Longitudinal monitoring of particles is of interest for vaccine development.

Recent research in designing next-generation vaccines investigates the best strategy to present immunomodulatory molecules to stimulate a robust immune response.[54] Development of particulate vaccines which mimic pathogens, termed pathogen-like particles (PLPs), are of great interest to control delivery of vaccine components.[54–57]. One type of PLP, composed of poly(lactide-co-glycolic acid) (PLGA), can be synthesized to have a diameter of 1 μm (mPLPs) or 300 nm (nPLPs). Physical qualities of PLPs induce different immune responses.[54–58]

Subsets of dendritic cells, a particular type of antigen-presenting cell, preferentially interact with m- or nPLPs.[54,58,59] To assess these interactions, in previous work PLPs were labeled with fluorescent markers, injected subcutaneously, and allowed to traffic to the lymph node *in vivo*. After 24 hours lymph nodes were harvested for histology. Fluorescent microscopy showed both types of PLPs were localized to the T cell zones, indicating cellular transport. mPLPs were also localized along the periphery of lymph nodes, indicating passive transport.[54] However, having longitudinal information would more holistically explain trafficking to the lymph node, thus facilitating more efficient design of vaccines to induce a particular response.

Two-photon intravital imaging, where the skin is removed and replaced with a transparent viewing window, has been widely used for *in vivo* longitudinal imaging of the lymph node. This modality has high resolution, can monitor complex cellular interactions in and around the lymph node, and has drastically advanced *in vivo* understanding of immunology.[60,61] However, the imaging procedure requires a specialized surgery, is highly invasive, and may cause an unwanted immune response.

PA imaging offers a minimally invasive alternative for lymph node imaging and has been implemented with a wide variety optical absorbers, including nanodroplets, metallic nanoparticles, endogenous absorbers, and dyes.[12,62–65] However, PA imaging has not been used for longitudinal monitoring of vaccine particles. By tagging different formulations of PLPs with optical absorbers, multi-wavelength PA imaging and spectroscopic analysis can be used to detect PLP trafficking to the lymph node, including localization, particle kinetics, and changes in blood flow. Ultrasound provides additional information by visualizing changes in lymph node morphology. Overall longitudinal monitoring of PA-tagged PLPs will aid vaccine development by providing a better understanding of potential mechanisms of action. In this thesis, the US/PA imaging platform was demonstrated using two formulations of nPLPs. However, the tools developed here are relevant to monitoring countless vaccine formulations, including various particle sizes, materials, surface coatings and molecule density.[58]

CHAPTER 2. PHOTOACOUSTIC PROPERTIES OF ANTERIOR OCULAR TISSUES

The chapter is adapted from an article published in the Journal of Biomedical Optics:

Kubelick, K. P., Snider, E. J., Ethier, C. R., & Emelianov, S. (2019). Photoacoustic properties of anterior ocular tissues. *Journal of Biomedical Optics*, *24*(5), 056004.

2.1 Abstract

Clinical imaging techniques for the anterior segment of the eye provide excellent anatomical information, but molecular imaging techniques are lacking. Molecular photoacoustic imaging is one option to address this need, but implementation requires use of contrast agents to distinguish molecular targets from background photoacoustic signals. Contrast agents are typically selected based on *a priori* knowledge of photoacoustic properties of tissues; however, photoacoustic properties of anterior ocular tissues have not been studied yet. Herein, anterior segment anatomy and corresponding photoacoustic signals were analyzed in brown and blue porcine eyes *ex vivo*. Measured photoacoustic spectra were compared to known optical absorption spectra of endogenous chromophores. In general, experimentally measured photoacoustic spectra matched expectations based on absorption spectra of endogenous chromophores reported in the literature, and similar photoacoustic spectra were observed in blue and brown porcine eyes. However, unique light-tissue interactions at the iris modified photoacoustic signals from melanin. The measured PA spectra established herein can be used for a variety of applications in

molecular PA imaging, such as detecting photoacoustically labeled stem cells in the anterior segment for glaucoma treatment.

2.2 Introduction

The most-investigated approaches for noninvasive assessment of internal ocular structures have been ultrasound (US) and optical imaging techniques.[66–74] Clinical use of ultrasound biomicroscopy and optical coherence tomography (OCT) are well-established in ophthalmology.[66,67,75] OCT provides excellent anatomical information by measuring changes in backscattered light.[71] Advances in OCT now allow real-time imaging, wide-field imaging, higher resolution detection, and assessment of other tissue optical properties, such as birefringence.[75–79] Overall OCT research has drastically improved the quality of anatomical imaging in ophthalmology. However, molecular imaging techniques are lacking. Accordingly, development of molecular contrast OCT (MCOCT) seeks to address this need by manipulating backscattering properties to distinguish molecular targets.[80–82] One approach is to introduce exogenous contrast agents that increase backscattering. However, high background signals from surrounding tissue still make it difficult to distinguish molecular targets. As a result, researchers have invented other clever solutions, including magnetomotive OCT and US, spectroscopic-OCT, pump-probe OCT, and photothermal OCT.[82–84]

Significant effort has recently been dedicated to development of photothermal OCT for the retina.[85–88] In photothermal OCT, an optical absorber is irradiated with light. Heat deposition causes thermoelastic expansion of the surrounding tissue and ultimately changes the optical path length measured by OCT.[85] Thus, photothermal OCT obtains molecular

information by indirectly measuring changes in backscattering resulting from an absorption event. A more straightforward approach may be to use an imaging modality that directly measures optical absorption, such as photoacoustic (PA) imaging.

PA imaging is similar to photothermal OCT in that irradiation of an optical absorber results in heat deposition and thermoelastic expansion of surrounding tissues. However, conditions used in PA imaging produce transient acoustic waves detected by a traditional ultrasound transducer.[13,89,90] Thus PA imaging combines advantages of optical and acoustic modalities to allow high resolution, high contrast, real-time, molecular imaging. A variety of endogenous and exogenous optical absorbers produce PA signals.[91] These optical absorbers serve as PA contrast agents and are detected using multi-wavelength spectroscopic PA imaging. Because PA contrast is based on absorption, molecular information compliments anatomical information provided by scattering-based modalities such as OCT or ultrasound. Thus, ultrasound and photoacoustic (US/PA) imaging systems are frequently combined, which is advantageous due to the established use of ultrasound in clinical ophthalmology.[70,74,92] Similarly, a multi-modal PA/OCT system has also been demonstrated for molecular imaging at the posterior segment to assess the retina.[93,94]

Our work focuses on extending molecular PA imaging to the anterior segment of the eye, i.e. tissues anterior to the vitreous humor. Anterior segment imaging techniques, such as OCT, slit-lamp microscopy, and ultrasound biomicroscopy, primarily provide anatomical information.[75] There is a need for molecular imaging techniques that could aid diagnosis, guide therapies, and improve understanding of anterior ocular diseases, including glaucoma, uveitis, and iridial pathologies.[82] Implementation of molecular PA imaging requires endogenous or exogenous contrast agents that must be carefully selected

based on *a priori* knowledge of PA properties of anterior segment tissues to ensure the contrast agent or interventional devices can be distinguished from background PA signals.[95–97] Although PA imaging has been demonstrated at a select few wavelengths in the anterior segment,[98–100] exploration of PA properties over a broad range of wavelengths is required to inform contrast agent selection for molecular PA imaging.

Thus, the goal of the work presented here was to establish PA spectral properties for the anterior segment over a range of wavelengths corresponding to the ideal tissue optical window.[91] In some cases, PA spectra in biological tissues directly correspond to optical absorption spectra of endogenous chromophores, i.e. melanin, oxygenated, and deoxygenated hemoglobin. Alternatively, PA spectra can be modified by light-tissue interactions.[101] We hypothesized the latter scenario may occur in the anterior segment due to the role of anterior tissues to control light propagation. Differences in eye color, resulting from unique combinations of scattering and melanin absorption at the iris, may also modify PA spectra.[102,103] For these reasons, we systematically measured the PA spectral properties of anterior segment structures in blue and brown porcine eyes, which are a relevant model of human anatomy and pigmentation. Results can aid development of molecular PA imaging strategies in the anterior eye, specifically by informing contrast agent selection to detect stem cells for glaucoma treatment.[36,104,105]

2.3 Materials and Methods

2.3.1 Eye preparation

All experiments used enucleated porcine eyes (Holifield Farms, Covington, GA). Blue and brown porcine eyes were studied to represent the two extremes in the range of

eye color from light to dark. Blue or brown eye color was determined by visual inspection, and no other colors were observed in samples from the slaughterhouse. Fresh and fixed eye globes were imaged. Eye globes were fixed by submersion in 10% neutral buffered formalin overnight before imaging, then maintained in phosphate buffed saline (PBS) prior to use. In total, 10 brown (3 fresh and 7 fixed) and six blue porcine eyes (2 fresh and 4 fixed) were imaged. Minimal differences between PA spectra of fresh and fixed samples were observed (data not shown).

2.3.2 Imaging protocol

The Vevo LAZR imaging system (FUJIFILM VisualSonics, Inc.) imaging system, incorporating ultrasound and photoacoustic (US/PA) imaging modes, was used for all imaging experiments. US/PA images were acquired using a 256-element transducer array operating at 20 MHz (LZ250) or 40 MHz (LZ550) center frequencies. The laser source was a Q-switched Nd:YAG laser pumped optical parametric oscillator (OPO) system (PRF = 20 Hz, 7 ns pulse duration). PA images were acquired within the 680 - 970 nm wavelength range at a frame rate of 5 Hz. Variations in laser pulse energy were corrected at the time of data acquisition using built in features of the Vevo LAZR.

In the first set of brown eye data, US/PA images were acquired at 1 degree increments as the eye was rotated 360°. Data was collected using both the 20 MHz and 40 MHz transducers, and the wavelength was varied from 680 nm to 970 nm in increments of 10 nm. The transducer was oriented either on-axis or perpendicular to the trabecular meshwork for translimbal light delivery for a total of 4 datasets. Preliminary analysis confirmed ultrasound-determined anatomy and PA spectra were similar in all views. Thus,

data acquisition at every degree was unnecessary. Adjustments were made to permit acquisition of more wavelengths and compile more thorough spectroscopic information. Specifically, US/PA images were acquired every 45 degrees at wavelengths from 680 nm to 970 nm in 5 nm increments. US/PA images were post-processed in MATLAB (MathWorks, Inc.) to determine the PA spectrum at anatomical landmarks.

2.3.3 Calculating and analyzing PA spectra

The average PA spectra for the anterior and posterior iris, trabecular meshwork, and sclera were determined to establish PA spectral properties specific to anatomy of the anterior segment. Each spectrum was determined by calculating the average PA signal over each region of interest. Each region of interest was isolated using spatial masks determined by manual segmentation based on anatomical information depicted in US/PA images. Variations in mask size and shape had minimal impact on PA spectra; specifically, the magnitude of the variation in the PA spectra between masks was comparable to the variations in the PA spectra between eyes and was thus not considered significant. The spectrum for each region of interest was then low-pass filtered using a 10-point moving average. The resulting spectra are henceforth referred to as "measured PA spectra". Measured PA spectra were compared to established optical absorption spectra for deoxygenated hemoglobin (Hb), oxygenated hemoglobin (HbO_2), and melanin.[106–112]

2.3.4 PA analysis in phantom experiments of pigment and scattering

The measured PA spectrum for the posterior iris required further analysis to evaluate effects of optical scattering. Following methods described elsewhere, melanin was isolated from dissected irises of fresh brown porcine eyes by collecting tissue in 10 ml

of water and mechanically disrupting to release pigment.[113,114] Pigment samples were size separated via centrifugation and isolated particles were resuspended in 2 ml of PBS for US/PA imaging.

A 10 x 10 cm plastic container held isolated pigment samples for US/PA imaging. Two small holes were drilled on opposite sides of the container and a silicone tube (Helix Medical) with an inner diameter of 0.062" and an outer diameter of 0.095" was fed through each hole and secured. The thickness of the iris was approximately 1 mm based on anatomical ultrasound images, slightly smaller than the inner diameter of the silicone tube. The tube was loaded with the following samples for US/PA imaging: PBS, iris pigment alone, and the same iris pigment with a piece of sclera wrapped around the tube. In the PA images of the circular cross-section of the tube, three regions of interest (top, middle, and bottom of the tube) were identified. The average PA signal was determined for each region of interest to assess changes in the PA spectrum of pigment due to light attenuation as a function of depth.

2.3.5 Analysis of local tissue composition using spectroscopic PA processing

The PA signal at each pixel, i.e., pressure $P(x, y, \lambda)$, is expressed as described elsewhere[48,90,115–117] and is reproduced in Equation 1:

$$P(x, y, \lambda) = \Gamma F(x, y, \lambda) \sum_{i=1}^{n} \mu_{a_i}(x, y, \lambda) \quad (1)$$

where λ is the wavelength, $\mu_a(\lambda)$ is the optical absorption coefficient, $F(x, y, \lambda)$ is the fluence, and Γ is the Grüneisen parameter. For heterogeneous tissue the total PA signal at each pixel is a superposition of each PA signal from n optical absorbers.

Spectroscopic PA datasets were pre-processed to correct for wavelength-dependent fluence attenuation in the iris. Fluence, $F(z, \lambda)$, is expressed as[101,118]:

$$F(z, \lambda) = F_o(\lambda) e^{-\mu_{eff}(\lambda) \cdot z} \quad (2)$$

where z is the imaging depth and F_0 is the fluence at the iris surface. Effective attenuation, $\mu_{eff}(\lambda) = \sqrt{3\mu_a(\lambda)\,(\mu_a(\lambda) + \mu_s(\lambda)(1 - g(\lambda))}$, was calculated based on: (i) the coefficient of anisotropy, $g(\lambda) = 2.25 \cdot \lambda^{-0.155}$,[119] and (ii) the optical scattering coefficient, $\mu_s(\lambda)$, of 10% intralipid,[120] and (iii) $\mu_a(\lambda)$ of melanin at the retinal pigmented epithelium (RPE).[107,108]

Unfortunately published iris-specific absorption and scattering values were not available for our wavelength range. The best alternatives to estimate μ_{eff} at the iris were to use generic scattering (intralipid) and melanin absorption in the RPE. For brown eyes, $\mu_a(\lambda\,[nm]) = 8 \cdot 10^{10}\,\lambda^{-3.48}\,[cm^{-1}]$, and for blue eyes, $\mu_a(\lambda\,[nm]) = 6.5 \cdot 10^{10}\,\lambda^{-3.48}\,[cm^{-1}]$.[107,108] The exponent of λ from the expression for $\mu_a(\lambda)$ is the critical parameter to describe the melanin absorption spectrum and was taken directly from published data for the RPE.[107] However, concentrations of melanin vary by orders of magnitude in ocular tissues, and the values of the leading coefficient in the expression for $\mu_a(\lambda)$ were reduced to accommodate different melanin concentrations and distributions at

the iris compared to the RPE.[107] The leading coefficients were incrementally adjusted until artifacts at the posterior iris were minimized. However, processing was conservative, and some artifacts were deliberately kept. Fluence correction is a complex technical issue and further work is required in the future.[101,118] Using Eq. 2, $F(z,\lambda)$ was calculated to produce a spatial distribution map of fluences in the iris. The PA signal, P, in Eq. 1 was multiplied by $1/F(z,\lambda)$ to correct for wavelength and depth-dependent fluence attenuation.[101,118]

After fluence correction, spectroscopic PA datasets were filtered using a 3 x 3 pixel (41 μm x 45 μm) median filter to remove large noise spikes. Images were then low pass filtered using a 6 x 9 x 3 pixel (depth x width x wavelength) moving average filter, approximately corresponding to 252 μm x 405 μm and a wavelength range of 15 nm. Photoacoustic signals below the noise floor, defined by $min(P) + 0.025(max(P) - min(P))$, were eliminated.

After filtering, spectroscopic PA datasets were analyzed using the linear least squares (LLS) regression method. LLS regression creates a spatial distribution map of each optical absorber in tissue. Concentration, C, of each absorber was estimated by separating contributions of each absorber to the total PA signal at each pixel. According to LLS regression methods described elsewhere,[90,121,122] the optical absorption coefficient, $\mu_a(\lambda)$, in Eq. 1 can be expressed as the product of the concentration of the absorber, $C_i(x,y)$, and the optical cross-section of the absorber, σ_a. Eq. 1 is rewritten as:

$$P(x,y,\lambda) = \Gamma\, F(x,y,\lambda) \sum_{i=1}^{n} C_i(x,y)\, \sigma_{a_i}(\lambda) \qquad (3)$$

The optical cross-section describes the likelihood an absorption event will occur, and σ_{a_i} is a matrix whose rows and columns correspond to wavelength and the normalized absorption spectrum of each pre-selected optical absorber, respectively. For our studies, two matrices of optical cross-sections were determined *a priori* for LLS regression. The first matrix of optical cross-sections was obtained from the normalized absorption spectra of melanin, HbO_2, and Hb, which are reported in the literature and represent optical properties of generic tissue.[106–112] The second matrix of optical cross-sections was obtained from our normalized measured PA spectra, which were specific to anterior ocular tissues. Thus, the same images were processed with LLS regression to produce two sets of concentration maps based on absorption spectra from the literature or based on our measured PA spectra.

Other research has established that it is theoretically ideal to use the maximum number of wavelengths for LLS regression of spectroscopic PA datasets.[123,124] In practice, such an approach may introduce inaccuracies due to laser energy stability, noise, and overlap of optical spectra.[123,124] Thus a subset of acquired wavelengths, $\lambda = 720 - 970\ nm$, was used for LLS regression of spectroscopic PA datasets. This range captured a majority of wavelengths acquired, eliminated wavelengths with energy instability, and preserved distinct features of all spectra.

2.4 Results

Brown porcine eyes were imaged *ex vivo* to evaluate PA response from constituent tissues. Ultrasound images resolved anatomical features in the anterior segment, such as the sclera, cornea, lens, and iris (Figure 2A and 2B). Histology aided proper identification

of structures (Figure 2C). Heavy pigmentation was also noted at the posterior iris (Figure 2C). By ultrasound, the cornea appeared slightly darker compared to other tissues, consistent with its relative transparency, and the interface between the cornea and sclera was distinct, reflecting differences in composition and microstructural organization of the cornea relative to other tissues. As expected, other tissues, such as the TM, could not be unequivocally identified due to similar scattering and ultrasound speckle patterns, confirming low ultrasound contrast between most tissue types.

PA images were acquired at 700 nm wavelength and consecutive 45° cross-sections. PA signals were observed in melanin-rich tissues, namely the anterior and posterior iris and TM (Figure 2D-G). Although the ciliary pigmented epithelium (CPE) is melanin-rich, no PA signal was present in this tissue due to strong attenuation of light by the overlying iris and sclera, resulting in low fluence at the CPE. PA signal was observed in some views in the scleral region, possibly corresponding to the suprachoroidal space (SCS) (Figure 2E and G). Although the sclera and SCS are not pigmented, the PA signal at these locations may result from sub-surface fluence.

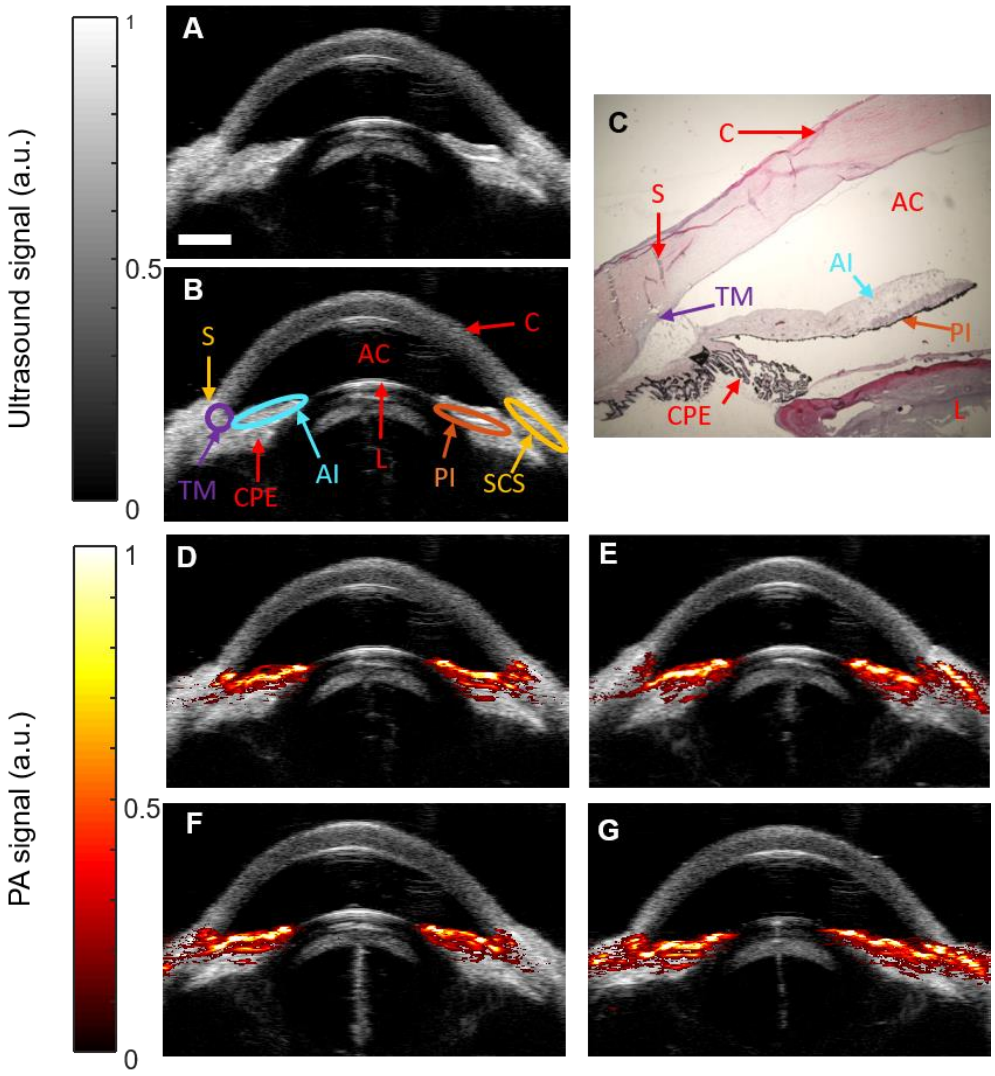

Figure 2. Visualization of anatomy and PA signals in the anterior segment. (A, B) Grayscale ultrasound images showing anatomy of the *ex vivo* porcine eye. S= sclera, AC = anterior chamber, C = cornea, L= lens, TM = trabecular meshwork, AI = anterior iris, PI =posterior iris, SCS = suprachoroidal space, and CPE = ciliary pigmented epithelium. (C) Corresponding histologic image of the porcine anterior segment stained with hematoxylin and eosin. (D-G) Overlay of ultrasound and PA (color scale) images at different locations (scans at 0°, 45°, 90°, and 135°) at λ = 700 nm. PA signals appeared at melanin-rich regions, such as the TM and throughout the iris, and consistently appeared at the same anatomical landmark in all frames. Scale bar = 3 mm.

Spectroscopic PA datasets were acquired in brown eyes at the anterior iris and posterior iris, scleral region, and TM from λ = 680 - 970 nm. Representative PA spectra

were plotted for fixed brown porcine eyes and distinct PA spectra were observed for each region (Figure 3A). To assess impact of fixation on the PA spectra, average PA spectra and standard deviations were calculated for multiple fresh brown porcine eyes (Figure 3B and 2C). PA spectra were similar between fresh and fixed eyes. The measured PA spectrum at the anterior iris closely followed the absorption spectrum of melanin reported in the literature (Figure 3B). Unexpectedly, the measured PA spectrum at the posterior iris did not follow the spectrum of melanin (Figure 3C) and showed more similarities to the literature absorption spectrum of oxygenated hemoglobin (HbO_2). Although HbO_2 was not expected in *ex vivo* tissue, comparison with the measured PA spectrum at the posterior iris was important. Similarities between the absorption spectrum of HbO_2 and the PA spectrum at the posterior iris (Figure 3C) highlight a potential source of PA imaging artifacts, and in turn impact use of these PA spectra to identify endogenous absorbers, select contrast agents, and facilitate molecular PA imaging, such as stem cell tracking.

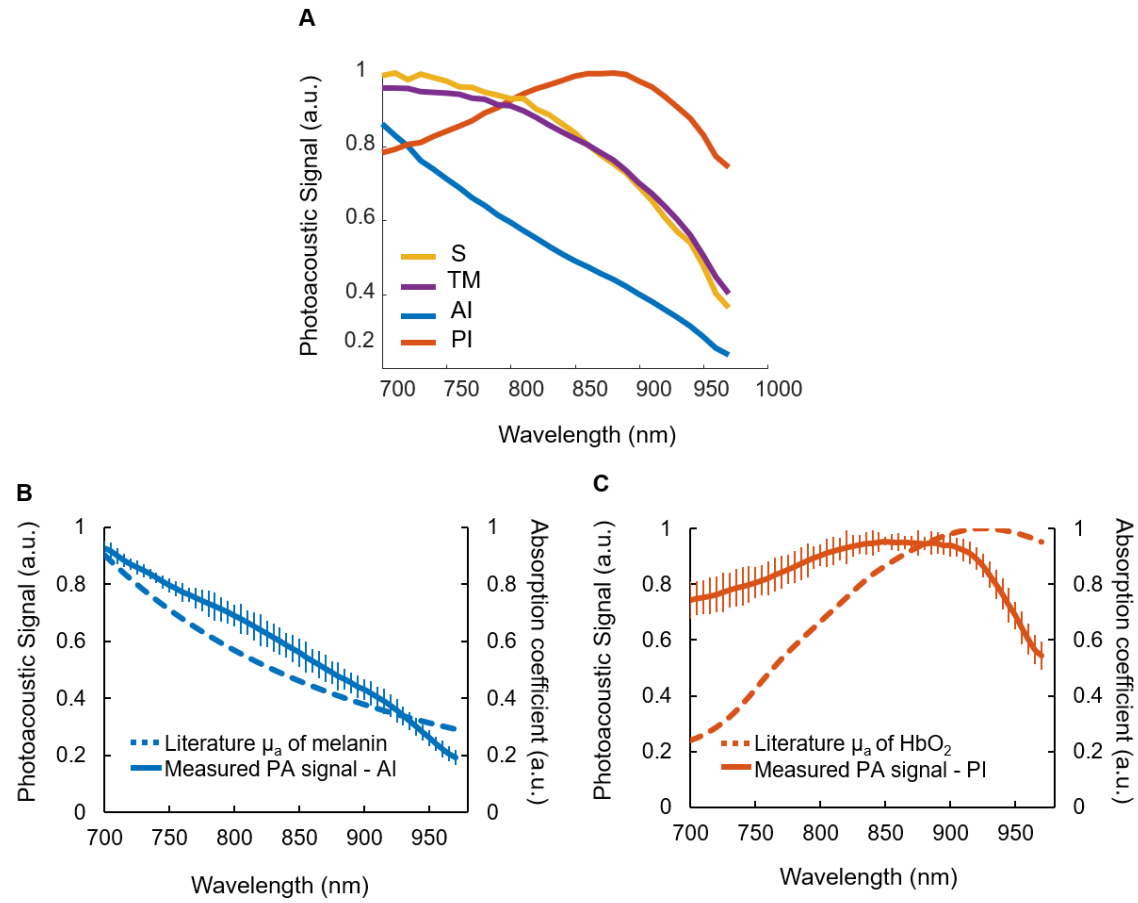

Figure 3. Photoacoustic spectra in fixed and fresh brown porcine eyes. (A) Representative PA spectra for the scleral region (S), TM, anterior iris (AI), and posterior iris (PI) for fixed brown porcine eyes. Average PA spectra and standard deviations were also calculated for the anterior iris (B) and posterior iris (C) in multiple fresh brown porcine eyes. PA spectra appeared similar in fixed and fresh eyes. The measured PA spectrum (solid blue line) of the anterior iris was compared to the reported absorption spectrum of melanin (dashed blue line). (C) The measured PA spectrum (solid orange line) of the posterior iris was compared to the reported absorption spectrum (dashed orange line) of HbO_2 to highlight a potential source of PA imaging artifacts following spectroscopic analysis.

We suspected the measured PA spectrum at the posterior iris actually represented a PA signal from melanin modified by wavelength-dependent fluence reaching the posterior iris. Therefore, fluence attenuation due to tissue absorption and scattering was studied in a silicone tube phantom. Cross-sectional US/PA images of the tube filled with

purified pigment were acquired and divided into three regions of interest to study fluence attenuation and the effect on the PA spectrum of melanin at increasing depths (Figure 4A). At the top of the tube, the PA spectrum matched the literature absorption spectrum of melanin. As light was attenuated by overlying pigment, the spectrum of melanin shifted and a peak appeared at 850 nm at the bottom of the tube (Figure 4A). Additional scattering from scleral tissue further modified the PA spectrum of melanin (Figure 4B). Specifically, compared to attenuation primarily by optical absorption (Figure 4A), the spectrum shifted at shallower depths, and a peak was observed in the middle of the tube (Figure 4B). The spectrum in the bottom region of interest further shifted with a peak closer to 900 nm. We suspected similar fluence attenuation occurred for light propagating from the anterior to posterior iris *in situ*. In other words, even though the measured PA spectrum at the posterior iris should match the literature absorption spectrum of melanin, the observed PA spectrum at the posterior iris (Figure 3C), resulted from wavelength-dependent light-tissue interactions.

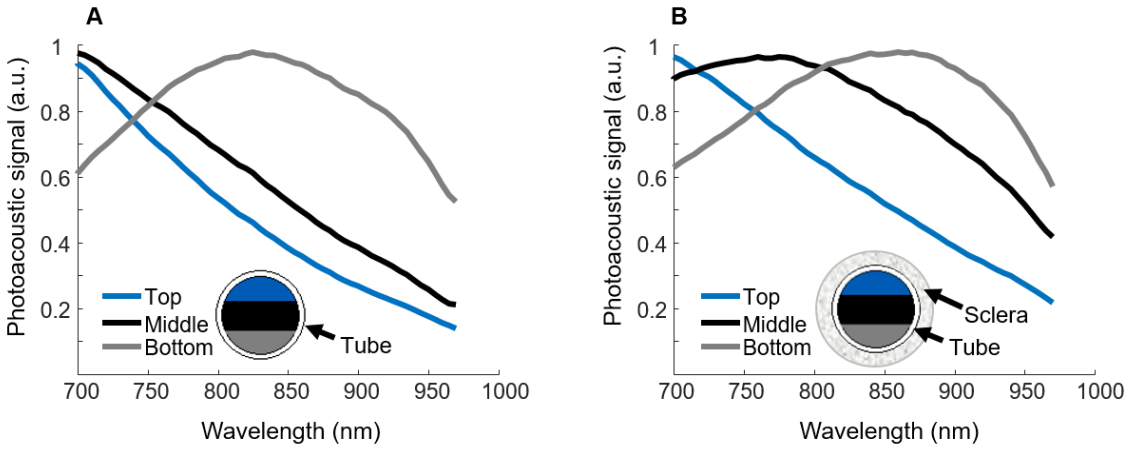

Figure 4. Photoacoustic spectrum of fresh pigment as a function of depth. A silicone tube was filled with purified pigment and cross-sectional US/PA images were acquired. The PA spectrum was analyzed within different regions of interest. "Top" and "Bottom" indicate locations closest to, and further from, the transducer with the least and most light attenuation, respectively. (A) The PA spectrum of melanin was modified by depth due to light absorption of melanin, causing a significant change in the PA spectrum. (B) The experiment was repeated with the addition of a scattering layer (sclera), resulting in further modification of the measured PA spectrum of melanin.

The literature absorption spectra of melanin, HbO_2, and Hb (Figure 5A) were compared to the measured PA spectra (Figure 5E) by processing spectroscopic PA datasets from brown eyes using the LLS regression method. The set of literature absorption spectra and measured PA spectra were used to obtain two different matrices of optical cross-sections. A spectrum for Hb could not be measured in brown eyes due to high melanin content; thus, the absorption spectrum of Hb from the literature was used instead (Figure 5E). The goal of this study was to compare each set of concentration maps, generated using the literature absorption spectra, serving as the "ground truth", or our experimentally obtained measured PA spectra.

Using either set of spectra, melanin was localized as expected at the anterior iris, posterior iris, and TM (Figure 5B and 5F). Because HbO_2 was not expected in post-mortem

tissue, pixels indicating presence of HbO_2 were determined to be image artifacts (Figure 5C). Agreement between the concentration maps for HbO_2 (Figure 5C) and the posterior iris (Figure 5G) indicated the artifact occurred due to the measured spectrum at the posterior iris being most similar to that of HbO_2 among the species we considered (melanin, Hb, HbO_2) although clearly the match is only very approximate (Figure 3C). Although the posterior iris is a melanin rich-tissue, the PA spectrum was modified by fluence attenuation. Without fluence correction, LLS regression predicted a prominent HbO_2 distribution at the posterior iris (data not shown). By implementing fluence correction, melanin was accurately localized to the anterior iris (Figure 5B and 5F) and the presence of HbO_2 was minimized at the posterior iris (Figure 5C and 5G). Hb was primarily localized to the posterior iris, but some discrepancies were observed between distribution maps (Figure 5D and 5H). LLS regression of sPA datasets from multiple brown eyes produced similar results, indicating PA properties were similar across various colorations of brown eyes from light to dark. Agreement between both sets of concentration maps (Figure 5B–D and 5F–H) impacts future use of measured PA spectra for molecular PA imaging. Similar concentration maps across multiple brown eyes indicated our measured PA spectra can be used to inform contrast agent selection for a particular application according to endogenous absorber distribution.

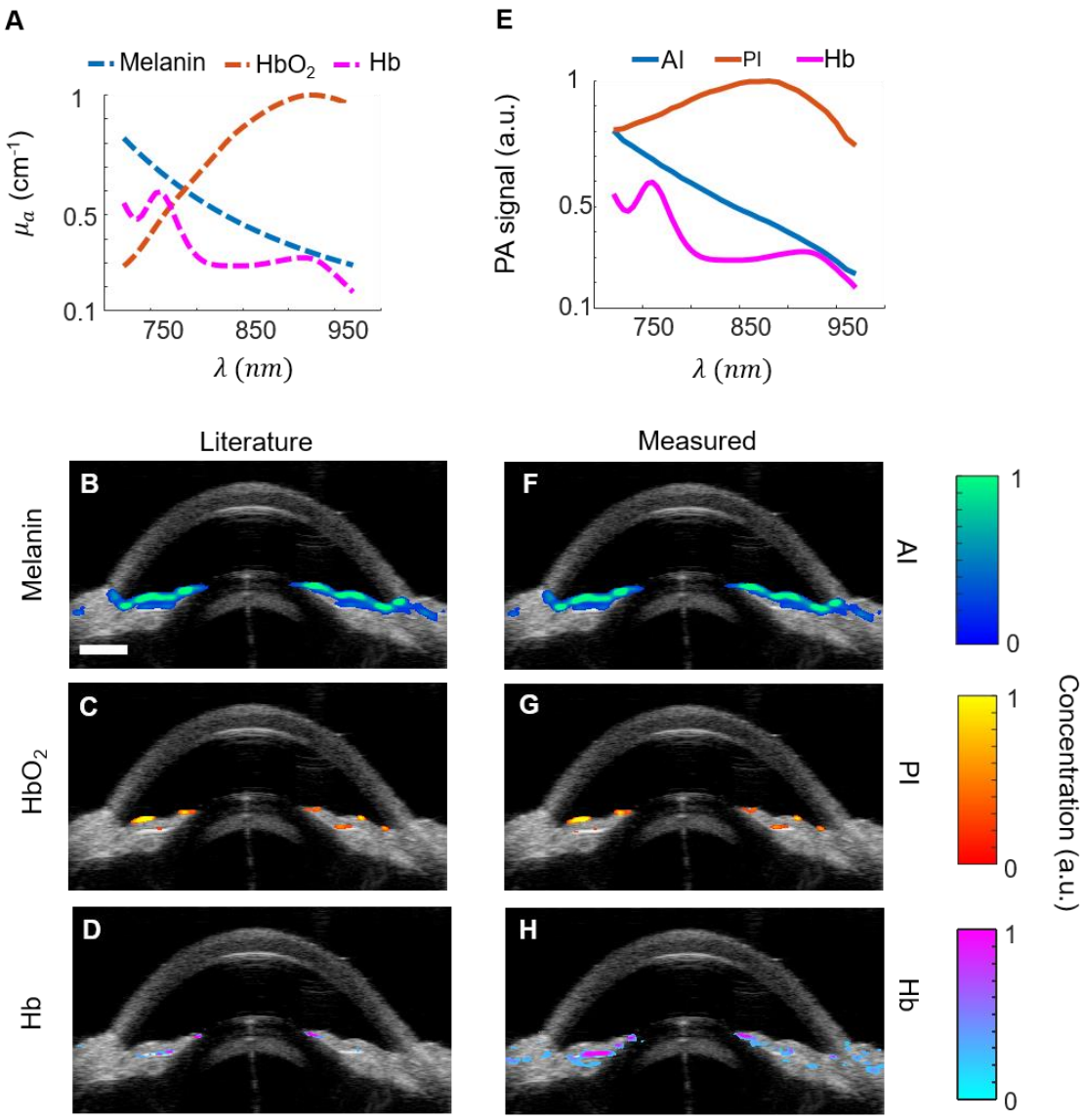

Figure 5. Spectroscopic photoacoustic analysis using LLS regression in brown porcine eyes. (A) Absorption spectra from literature used for sPA analysis, and resulting computed distributions of melanin (B), HbO_2 (C), and Hb (D). (E-H) as in (A-D), but using measured PA spectra. Overlay of ultrasound (grayscale) and spectroscopic PA images showed localization of melanin (blue color scale), HbO_2 (orange color scale), and Hb (pink color scale). Melanin was localized as expected. Absorption spectra from the literature and measured by photoacoustic imaging produced similar results. Some artifacts remained in the HbO_2 images (C and G). Scale bar = 3 mm.

Characterization and analysis of PA properties was repeated in blue porcine eyes (Figure 6). Each spectrum in brown and blue eyes was normalized according to its peak

absorption to better visualize the photoacoustic properties in different eye colors. Results do not depict differences in magnitude of PA signals. The posterior iris was the only structure to consistently show a PA signal in the blue eye at the 700 nm wavelength (Figure 6A). Due to less melanin than in brown eyes, PA signals were not evident in other tissues. The PA signal from melanin at the posterior iris was modified by fluence attenuation, and thus a similar artifact was observed in the blue eye (Figure 6B) as in brown eyes. Other types of PA spectra were also occasionally observed in blue eyes (Figure 6C and 6D), but were not localized to a consistent location, i.e., the spectrum shown in Figure 6B was most prevalent in blue eyes.

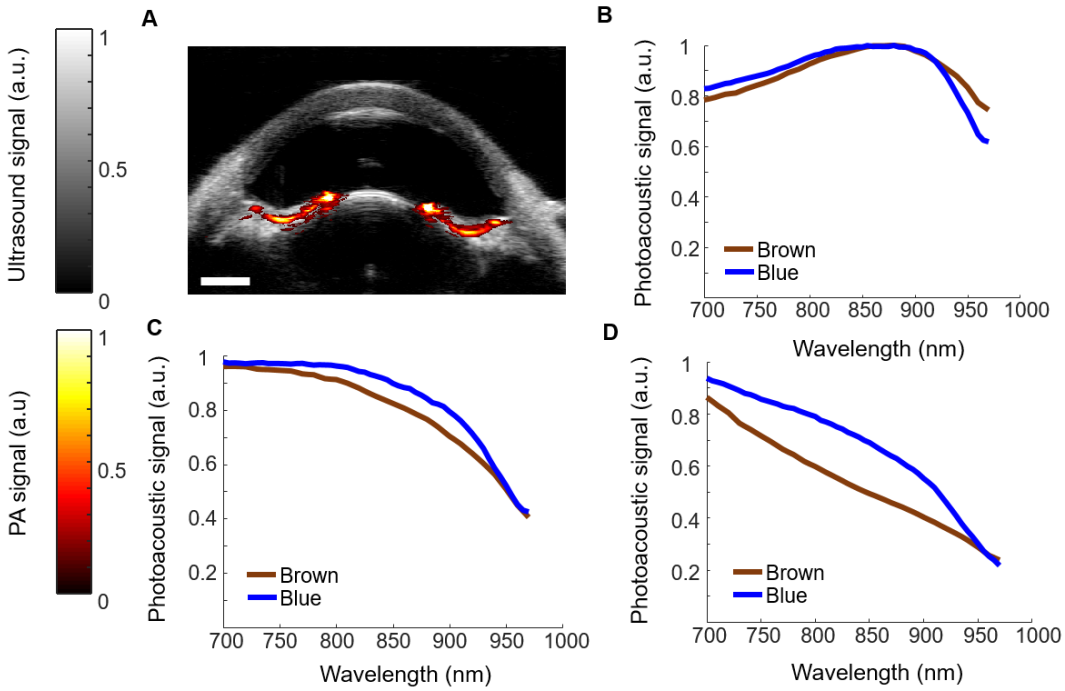

Figure 6. Comparison of measured PA spectra in blue and brown eyes. (A) Overlay of ultrasound (grayscale) and photoacoustic (color scale) images in a blue porcine eye. PA signal was localized to the posterior iris. (B-D) Spectra were separated based on results from brown porcine eyes. (B) A modified melanin spectrum, resembling that of oxygenated hemoglobin, was isolated to the posterior iris in both eye colors and was the dominant spectrum observed in blue eyes. (C and D) Other types of spectra were observed in blue eyes, but were not localized to a consistent location. (D) The PA spectrum resembling melanin was most prevalent in brown eyes. Scale bar = 3 mm.

Spectroscopic PA analysis using the LLS regression method was repeated for blue eyes (Figure 7). In the case of blue eyes, sPA analysis was conducted using the measured PA spectra from brown eye datasets, except for the spectrum of Hb, which was possible to isolate in a blue eye. Spectroscopic PA datasets from the blue porcine eyes were similarly processed using either the literature absorption spectra (Figure 7A) or the measured PA spectra (Figure 7E) to identify absorbers. After correcting for wavelength-dependent fluence attenuation, melanin was accurately localized at the iris (Figure 7B and 7F). Some effects of fluence attenuation remained (Figure 7C and 7G). However, fluence correction

increased melanin localization at the posterior iris (Figure 7B and 7F) and minimized the presence of HbO_2 (Figure 7C) and the modified melanin spectrum at the posterior iris (Figure 7G). Hb was also identified (Figure 7D and 7H). sPA analysis in blue eyes accurately localized absorbers, and agreement between concentration maps (Figure 7B–D and 7F–H) indicated conservation of PA properties across drastically different eye colors.

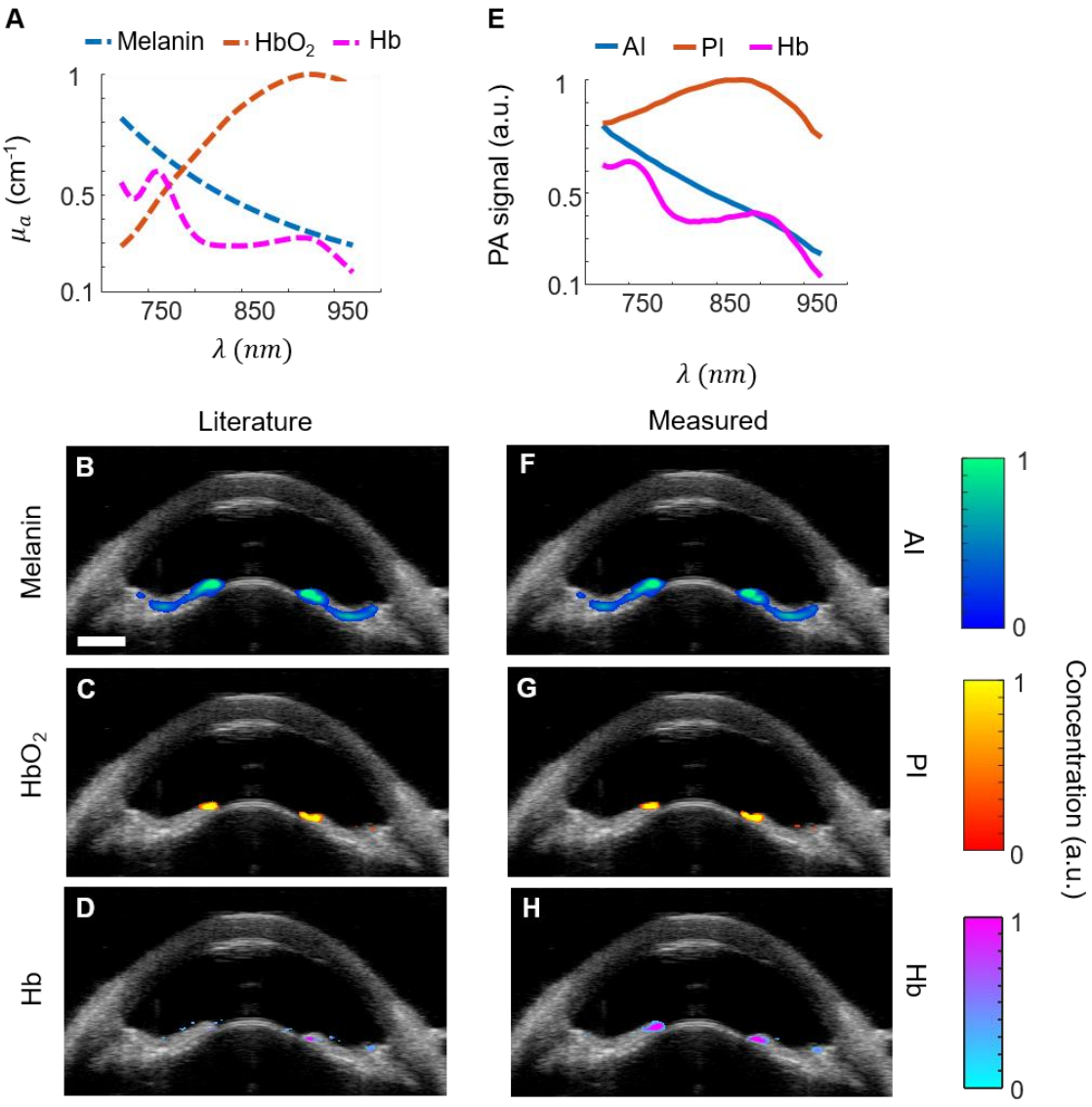

Figure 7. Spectroscopic PA analysis using LLS regression in blue porcine eyes. (A) Literature absorption spectra used for sPA analysis. (B-D) sPA analysis using the literature absorption spectra. (E) Measured PA spectra used for sPA analysis, which were compiled from brown eye datasets, except for the spectrum of Hb. (F-H) sPA analysis using the measured PA spectra. Overlay of ultrasound (grayscale) and spectroscopic PA images showed localization of melanin (blue color scale), HbO_2 (orange color scale), and Hb (pink color scale). Absorbers were localized as expected according to known anatomy. Literature absorption spectra or measured photoacoustic spectra produced similar results, and either can be applied for sPA analysis. These results show that the PA spectra can be used for sPA analysis in both brown and blue eyes. Scale bar = 3 mm.

2.5 Discussion

Clinically available ophthalmic imaging modalities such as OCT and ultrasound provide excellent anatomical information for ocular tissues.[74,75,125] However molecular imaging techniques have not developed as rapidly for the anterior segment.[81,82] PA imaging is one option to address the need for molecular imaging in the anterior eye. Implementation of molecular PA imaging requires use of endogenous or exogenous contrast agents.[13,91] Contrast agents must be carefully selected based on the application of interest and PA properties of the surrounding tissues. Without prior knowledge of PA properties of anterior segment tissues, it is impossible to ensure a contrast agent can be distinguished from background PA signals. Thus, the first step to extend molecular PA imaging to the anterior eye is to establish PA spectral properties.

We here systematically analyzed PA properties of anterior segment tissues to produce a set of measured PA spectra in the first optical window between 680 – 970 nm to facilitate molecular PA imaging. Distinct PA spectra were observed at the TM, anterior iris, posterior iris, and scleral region in brown porcine eyes. Similar PA spectra were observed at the posterior iris in blue porcine eyes. These measured PA spectra were compared to literature absorption spectra by analyzing sPA datasets of blue and brown porcine eyes using LLS regression to produce concentration maps of each absorber. Good agreement was observed between absorber maps, which validates future use of our PA spectra to facilitate molecular PA imaging *in vivo*.

Each measured PA spectrum was expected to match a known absorption spectrum of an endogenous absorber, specifically melanin. However, this was only true for the

anterior iris in brown eyes. In other tissues, the PA spectrum was modified by wavelength- and depth-dependent fluence attenuation. These effects were most prominent at the posterior iris, especially in blue eyes. The impact of fluence attenuation on the PA spectrum at the iris was consistent with results from a simplified phantom experiment. Without fluence correction, sPA analysis using LLS regression contained many artifacts and mistakenly attributed PA signals to light absorption by HbO_2, which coincidentally has a spectrum similar to the fluence-modified melanin spectrum. Wavelength- and depth-dependent fluence correction allowed better PA identification of melanin in the anterior segment and minimized artifacts.

Further improvement to the fluence correction method is possible. Specifically, we assumed a uniform concentration of melanin, but concentration varies spatially throughout the iris. In addition, at the wavelengths of interest (680 - 970 nm), information on melanin absorption and scattering at the iris were unknown. Thus, optical properties of the iris were estimated based on available data for the RPE and a general model of scattering (intralipid) as substitutes.[106–108,119,120] This motivates further study so that parameters specific to the iris can be determined. We anticipate the effects of fluence attenuation observed here will impact molecular PA imaging strategies in the future.

Comparison between blue and brown porcine eyes indicated that the set of measured PA spectra were independent of eye color, at least in the near infrared region. This result was fortuitous but not obvious *a priori*. Although blue and brown eyes have the same type of pigment, in the visible spectrum differences in melanin concentration and scattering produce variations in eye color. In spite of distinct optical properties in the visible regime, PA properties in the near-infrared regime were similar across eye colors.

This result was important to confirm our measured PA spectra were applicable to both extremes in eye color (blue and brown). Thus, a single set of measured PA spectra can possibly inform molecular PA imaging strategies across the full spectrum of eye colors. Each eye color does not appear to require a unique set of spectra to predict endogenous absorber distribution and background PA signals to inform contrast agent selection. If this were the case, implementing molecular PA imaging in the anterior eye would likely be impractical.

2.6 Conclusions

Photoacoustic tissue properties were analyzed throughout the anterior segment. Measured PA spectra were compiled based on distinct PA spectra observed in the anterior and posterior iris, TM, and sclera. These spectra were compared to existing published absorption spectra. sPA analysis using both the measured PA spectra and published absorption spectra accurately localized absorbers throughout the anterior segment. In addition, the measured PA spectra from the brown eye were used for sPA analysis of datasets from the blue eyes. Although there are many eye colors in the visible range, our comparison of blue and brown porcine eyes indicated anterior segments are photoacoustically similar in the near infrared wavelength range. Results have important implications for development of molecular PA imaging strategies and other light-based imaging techniques and therapies in the anterior segment, including our particular application of interest, stem cell tracking for glaucoma treatment.

CHAPTER 3. A STEM CELL TRACKING PLATFORM FOR OPHTHALMIC APPLICATIONS USING US/PA IMAGING

The chapter is adapted from an article published in Theranostics:

Kubelick, K. P.,* Snider, E. J.,* Ethier, C. R., & Emelianov, S. (2019). Development of a stem cell tracking platform for ophthalmic applications using ultrasound and photoacoustic imaging. *Theranostics*, *9*(13), 3812. **Equal contribution*

3.1 Abstract

Glaucoma is the second leading cause of blindness in the world. Disease progression is associated with reduced cellularity in the trabecular meshwork (TM), a fluid drainage tissue in the anterior eye. A promising therapy seeks to deliver stem cells to the TM to regenerate the tissue and restore its function. However, like many stem cell-based regenerative therapies, pre-clinical development relies heavily on histology to evaluate outcomes. To expedite clinical translation, we are developing an ultrasound/photoacoustic (US/PA) imaging platform for longitudinal tracking of stem cells in the anterior eye. Mesenchymal stem cells (MSCs) were pre-labeled with gold nanospheres *in vitro* and injected through the cornea of *ex vivo* porcine eyes. Physiological pressure was imposed to mimic *in vivo* conditions. AuNS-labeled MSCs were injected through the cornea while single-wavelength US/PA images were acquired. At 5 hours post-injection, three-dimensional multi-wavelength US/PA datasets were acquired and spectroscopic analysis was used to detect AuNS-labeled MSCs. US/PA results were compared to fluorescent microscopy. The US/PA imaging platform was able to provide real-time monitoring of the

stem cell injection and distinguish AuNS-labeled MSCs from highly absorbing background tissues in the anterior segment. Our US/PA imaging approach can inform preclinical studies of stem cell therapies for glaucoma treatment, motivating further development of this theranostic imaging tool for ophthalmic applications. Several future research directions were also identified from these studies and were explored: 1) assessing laser safety *in vivo*; 2) custom focused-light delivery systems; and 3) use of photomagnetic nanocubes to improve delivery efficiency.

3.2 Introduction

Glaucoma is the second leading cause of blindness in the world, estimated to affect more than 70 million people.[30] Disease progression is frequently associated with elevated intraocular pressure (IOP), which in turn is associated with reduced cellularity in the trabecular meshwork (TM), a fluid drainage tissue in the anterior eye.[31–33] There is no cure for glaucoma, and existing treatments focus on slowing disease progression.

A promising therapeutic approach is to deliver stem cells to the TM to regenerate this tissue and restore its function, so as to lower IOP. To this end, induced pluripotent stem cells and mesenchymal stem cells (MSCs) have been investigated as therapeutics to renormalize IOP in glaucoma.[34–37] Although stem cell delivery decreased IOP and restored TM function, conclusions on how stem cells caused a positive therapeutic outcome were inconsistent and contradictory.[36,37]

In this case, like many other regenerative therapies using stem cells, preclinical development relies heavily on histology to evaluate outcomes.[2,3] Although histology provides detailed information at the cellular and molecular level, drawbacks include highly

invasive, destructive sample preparation.[1–3] A related approach is fluorescent imaging of pre-labeled cells in whole tissue using confocal microscopy [2,126], which is somewhat less time-consuming than traditional histology but is also destructive and typically suffers from poor imaging resolution at depths beyond the sub-millimeter scale due to strong optical scattering by the overlying tissues.[2] As a result, longitudinal monitoring is challenging, making it more difficult to interpret results and inform future therapy design. Development and clinical translation of this novel stem cell therapy would thus be expedited by developing a minimally invasive, longitudinal stem cell tracking platform for the anterior eye.

A variety of imaging technologies exist at the preclinical or clinical stage to address this need, including magnetic resonance imaging (MRI), X-ray/computed tomography (CT), optical imaging, positron emission tomography (PET), and ultrasound. Each has its own advantages, and compromises are always made between resolution, sensitivity, image acquisition speed, penetration depth, contrast, safety, and cost. Specific to ophthalmology, optical coherence tomography (OCT) and ultrasound are widely used clinically [39,42,73,127–129], with contrast based on backscattering of optical and acoustic waves, respectively.[38,41,71] Both modalities provide excellent anatomical information, but their contrast is inherently poor. OCT faces an additional challenge for anterior segment imaging due to light penetration through highly scattering ocular tissues, such as the sclera.[130–132]

One preclinical imaging modality, photoacoustic (PA) imaging, has been explored for anterior and posterior segment imaging in ophthalmology, but current research is limited.[100,133–135] Unlike OCT and ultrasound, PA imaging is advantageous because contrast is based on optical absorption that significantly varies between different tissue

types. In PA imaging, a pulsed laser irradiates an optical absorber, such as an exogenous contrast agent. Heat deposition upon absorption causes thermoelastic expansion of the surrounding tissue to create transient acoustic waves, which can be detected with a traditional ultrasound transducer.[12,13,15,20] PA imaging combines advantages of acoustic and optical modalities to provide cellular- or molecular-level information with high resolution and contrast at increased imaging depths.[2,3] Furthermore, combined ultrasound and photoacoustic (US/PA) imaging simultaneously provides anatomical and functional information.[12,13] This multi-modal imaging approach is even more appealing due to existing clinical use of ultrasound in ophthalmic applications.[128]

In this work, we describe development of a combined US/PA imaging platform to track stem cells in the anterior eye. We first compare the detection capabilities of a traditional optical modality (confocal microscopy of fluorescently labeled cells) with photoacoustic imaging in a simplified phantom system where the number of cells was known *a priori*. We then proceed to image cells in whole, intact tissue using US/PA imaging. Although PA imaging has been used to successfully monitor stem cells in other applications, translation of US/PA imaging of stem cells in the anterior segment of the eye has to satisfy several unique requirements involving the optical properties of anterior ocular tissues, selection of a contrast agent to label stem cells, light-tissue interactions, and laser safety.[18,53,136–139] We show proof-of-principle of the US/PA imaging platform to monitor stem cell location in real-time and to distinguish stem cells from highly absorbing background tissues in the anterior segment of the eye. This work will inform future development of stem cell therapies for glaucoma treatment and lays the groundwork for a novel theranostic imaging tool in ophthalmology.

3.3 Materials and Methods

3.3.1 Cell culture

Human adipose-derived MSCs (Lonza) were grown in α-minimum essential medium supplemented with 20% fetal bovine serum (FBS), penicillin, streptomycin, and L-glutamine. At 80-90% confluency, MSCs were detached using 0.05% Trypsin/EDTA and seeded in fresh T75 cell culture flasks at a density of 5,000 cells/cm^2. In all experiments, MSCs were used at passage numbers five or six. Each MSC donor strain was validated by Lonza for expression of MSC surface markers (CD13, CD29, CD44, CD73, CD90, CD105, and CD166) and minimal expression of negative MSC markers (CD14, CD131, CD45). Each MSC donor strain was also previously characterized in our lab for adipogenic, chondrogenic, and osteogenic differentiation potential, as well as CD90 expression following expansion.[140]

3.3.2 Synthesis of gold nanospheres

Gold nanospheres (AuNSs) were synthesized following the citrate reduction method, as detailed in previous reports.[141] Briefly, hydrogen tetrachloroaurate (III) hydrate (Alfa Aesar) and sodium citrate tribasic dihydrate (Sigma-Aldrich), were used as received. AuNSs, 20 nm diameter, were synthesized via the citrate reduction method as described elsewhere.[142] Briefly, 0.5 ml of a 1% w/v solution of hydrogen tetrachloroaurate was added to 47 ml of deionized ultrafiltered (DIUF) water. The solution was brought to a boil while stirring, then 2.5 ml of a 1% w/v solution of sodium citrate was added. After approximately 15 minutes, the solution appeared red and was cooled to room temperature. UV-Vis spectrophotometry (Synergy HT microplate reader, BioTek Instruments) between 400 nm

to 995 nm was used to validate the absorbance spectrum. Transmission electron microscopy (TEM; Hitachi HT7700 TEM, IEN/IMAT Materials Characterization Facility, Georgia Institute of Technology) was used to validate particle size and morphology. Carbon formvar TEM grids (Electron Microscopy Sciences) were prepared by drop casting 3 μl of particle solution and drying overnight at room temperature. Images were acquired at an accelerating voltage of 100 – 120 kV. The hydrodynamic diameter and zeta-potential of AuNSs were assessed (Malvern Zetasizer Nano ZS). Dynamic light scattering (DLS) measurements to determine hydrodynamic diameter were performed at 25˚C using a disposable cuvette. Six recordings were obtained, each consisting of 13 measurements. Zeta-potential measurements were performed using a Folded Capillary Zeta Cell (Malvern) to determine the surface charge of AuNSs. Six recordings were obtained, each consisting of at least 12 measurements.

3.3.3 Labeling cells with gold nanospheres

AuNSs were sterilized under UV light for at least 12 hours prior to stem cell labeling experiments. Adipose-derived MSCs (Lonza) were incubated for 24 hours with AuNSs at an optical density of 2, a measure of concentration according to light absorbance, which corresponds to approximately 200 μg/ml of gold/ml of media, in α-minimum essential medium (Mediatech) supplemented with 20% FBS, 2mM L-glutamine, and 1x penicillin/streptomycin. AuNSs were previously determined to have minimal cytotoxic effects on stem cell viability and multipotency.[142] We also carried out Alamar blue tests and confirmed that, for the AuNS concentration used in this study, stem cell metabolic activity was not impacted. Following uptake, gold nanosphere-labeled stem cells (hereinafter referred to as AuNS-labeled MSCs) were collected and used for cell tracking

experiments. AuNS-labeled MSCs were washed with phosphate buffered saline (PBS) to remove excess nanoparticles, detached with Trypsin-EDTA, and centrifuged (300 x g, 10 minutes) to separate free AuNSs from AuNS-labeled MSCs. Successful labeling was confirmed by measuring cellular side scatter by flow cytometry (Attune NxT flow cytometer, Thermo Fisher) as previously described [126,143], brightfield microscopy (Zeiss Axio Observer) of naïve (unlabeled) and AuNS-labeled MSCs stained with eosin *in vitro*, and UV-Vis spectrophotometry measurements (Evolution 220 Spectrophotometer, Thermo Scientific) of AuNS-labeled MSCs and naïve MSCs. For fluorescent cell detection, in addition to AuNSs, MSCs were also labeled with 5 μM carboxyfluorescein succinimidyl ester (CFSE, Affymetrix) for fifteen minutes at 37^{o}C, followed by washing with cell culture media to remove excess CFSE (hereinafter referred to as double-labeled MSCs).

3.3.4 Assessing stem cell multipotency after gold nanosphere labeling

MSCs were seeded in a 6-well plate with maintenance media and allowed to adhere to the plate overnight. Maintenance media was changed the following day, and MSCs were incubated with fresh media containing AuNSs as described above (see Section 3.3.3). After 24 hours, the AuNS-containing media was removed and AuNS-labeled MSCs were rinsed three times with PBS to remove residual nanoparticles. Then, two of the wells underwent osteogenic differentiation, two of the wells underwent adipogenic differentiation, and two of the wells were fed maintenance media.

Osteogenic induction media consisted of Dulbecco's Modified Eagle Medium (DMEM; Corning), 10% FBS, 1% penicillin/streptomycin, 100 nM dexamethasone (Sigma-Aldrich), 10 nM beta-glycerophosphate (Calbiochem), and 50 μg ascorbic acid

(Sigma-Aldrich). AuNS-labeled MSCs were fed osteogenic induction media every three days for two weeks. A Von Kossa staining kit (Millipore Sigma) was used to evaluate presence of calcium deposits indicative of osteogenesis. AuNS-labeled MSCs were stained per the manufacturer's protocol. Briefly, media was aspirated, and the AuNS-labeled MSCs were washed with PBS (w/o Ca^{2+} or Mg^{2+}) followed by fixation in 10% neutral buffered formalin for 10 minutes. The formalin was aspirated, and cells were washed with PBS again. Cells were covered with 5% silver nitrate for 40 minutes under UV light. The silver nitrate solution was aspirated, and cells were rinsed with distilled water. Cells were covered with 5% sodium thiosulfate for 2 minutes, followed by rinsing in running tap water. Cells were covered with nuclear fast red stain for 5 minutes, followed by rinsing in running tap water. Staining was assessed with brightfield microscopy (Leica).

For adipogenic differentiation, AuNS-labeled MSCs were grown in maintenance media until reaching 100% confluence. At this point, AuNS-labeled MSCs were then fed adipogenic induction and adipogenic maintenance media. Adipogenic maintenance media consisted of DMEM supplemented with 10% FBS, 1% penicillin/streptomycin, and 10 μg/ml insulin (Sigma-Aldrich). Adipogenic induction media consisted of DMEM supplemented with 10% FBS, 1% penicillin/streptomycin, 1 μM dexamethasone (Sigma-Aldrich), 10 μg/ml insulin (Sigma-Aldrich), 100 μM indomethacin (Sigma-Aldrich), and 10 μg/ml 3-isobutyl-1-methylxanthine (IBMX; Sigma-Aldrich). AuNS-labeled MSCs were cultured in adipogenic induction media for 3 days followed by two days in adipogenic maintenance media. This cycle was repeated three times followed by 7 additional days in the adipogenic maintenance media. Oil Red O staining (Sigma-Aldrich) was used to evaluate presence of lipid deposits indicative of adipogenesis. A stock solution of Oil Red

O was prepared by adding 300 mg of Oil Red O to 100 mL of 99% isopropanol. The working solution consisted of 3 parts stock solution and 2 parts DIUF. The working solution sat at room temperature for 10 minutes, followed by filtration. To stain the AuNS-labeled MSCs, the media was aspirated, and cells were rinsed with PBS. AuNS-labeled MSCs were then fixed with 10% neutral buffered formalin for 10 minutes. The formalin was aspirated, and cells were washed again with PBS. Each well was then covered with 60% isopropanol. After 4 minutes, the isopropanol was poured off, and the cells were covered with the Oil Red O working solution. After 5 minutes, cells were rinsed with running tap. Staining was assessed with brightfield microscopy (Leica).

3.3.5 Overview of Vevo LAZR imaging system

A Vevo LAZR (FUJIFILM VisualSonics, Inc.) imaging system, incorporating ultrasound and photoacoustic (US/PA) imaging modes, was used for all imaging experiments. US/PA images were acquired using a 256 element transducer array operating at 20 MHz (LZ250) center frequency. The laser source was a Q-switched Nd:YAG pumped optical parametric oscillator (OPO) laser (pulse repetition frequency = 20 Hz, 7 ns pulse duration). PA images were acquired within the 680 - 970 nm wavelength range at a frame rate of 5 Hz. Variations in laser pulse energy were corrected at the time of data acquisition using built-in features of the Vevo LAZR. All three-dimensional (3D) US/PA images were produced using a translational motor stage.

3.3.6 Analyzing PA signals of labeled cells in a tissue-mimicking phantom

To verify successful cell labeling, AuNS-labeled MSCs were imaged in a tissue-mimicking gelatin phantom [144]. The base of the phantom consisted of 8% (w/v) gelatin

and 0.2% (w/v) silica (Sigma-Aldrich). Inclusions were made by adding 16% (w/v) gelatin to an equal volume of AuNS-labeled MSCs. Each inclusion was imaged over a range of wavelengths (λ = 680 nm to 970 nm at 5 nm increments). Data was exported and post-processed in MATLAB (MathWorks, Inc.).

3.3.7 Comparing PA imaging and fluorescent microscopy in agarose gels

Double-labeled MSCs (AuNSs and CFSE) were collected, fixed in 10% neutral buffered formalin for 10 minutes, and suspended at concentrations of 0, 1k, 5k, 10k, 25k, 50k, 100k, 250k and 500k cells/ml in 1% (w/v) agarose gels (Sigma Aldrich). Triplicates of each gel were formed in 48 well plates. Once solidified, the gels were removed from the well plate and stained using DAPI (Thermo Fisher; see section 4.3.10 for detailed protocol). Each gel was imaged using confocal microscopy (LSM 700, Zeiss) followed by US/PA imaging at a wavelength of 700 nm to produce three-dimensional images for both modalities. Total fluorescent signal, total PA signal, and cell counts from DAPI labeling were determined. Although the cylindrical gels had a depth of approximately 17 mm, analysis could only be performed for a smaller region of interest with a depth of 0.5 mm due to limited light penetration of confocal microscopy. The region of interest was selected according to the optimum light focal depth for each modality, and cells were evenly distributed throughout the gel.

3.3.8 Ex vivo studies in whole porcine eyes

For ocular delivery experiments, porcine eyes from a slaughterhouse (Holifield Farms, Covington, GA) were used within 3 to 4 hours after enucleation. Eyes were secured on top of a tissue-mimicking phantom base composed of 1% (w/v) agarose. To maintain

physiological pressures during cell injection, a reservoir containing serum-free, phenol red-free DMEM (supplemented with 1x penicillin, 1x streptomycin, 1x amphotericin, and 2 mM L-glutamine) was connected to each eye by cannulating the anterior chamber using a 23-gauge needle passing through the cornea. The elevated reservoir was placed 10 to 16 cm above the limbus (cornea-sclera transition region) to clamp IOP at 8 to 12 mmHg. A 250 µL suspension of double-labeled MSCs at concentrations of 1000, 2000, or 4000 cells/µl were injected into the anterior chamber through the cornea using a 27-gauge needle. After injection, eyes remained pressure clamped at a physiological pressure of 8 to 12 mmHg and were stored in a cell culture incubator for 5 hours. During this time, media from the elevated reservoir flowed into the anterior chamber and then out through the trabecular meshwork, which naturally drains fluid from the anterior chamber; thus allowing for continuous stem cell circulation in the anterior chamber and complete exchange of the anterior chamber fluid. The schematic of the perfusion set up is presented in Figure 8. Eyes were then fixed by submersion in a 10% neutral buffered formalin solution for 24 hours.

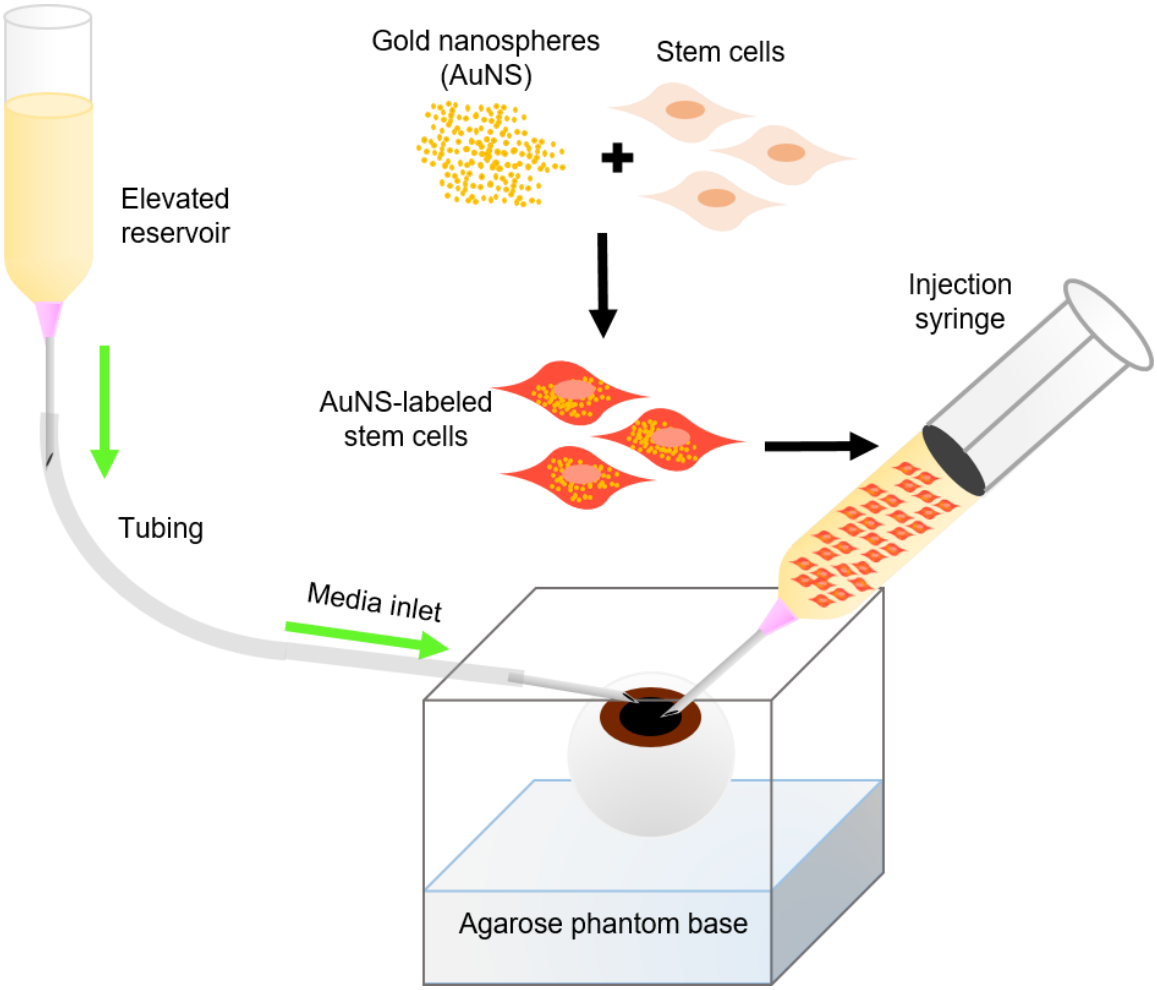

Figure 8. Perfusion set up. *Ex vivo* porcine eyes were hydrostatically clamped using an elevated reservoir to mimic the *in vivo* situation, specifically by maintaining physiological IOP and fluid flow rates within the anterior segment and through the aqueous outflow pathway. AuNS-labeled MSCs were injected using a separate syringe. The elevated reservoir remained in place during the injection and 5 hour incubation period. Stem cells circulated in the anterior chamber because inflowing media from the elevated reservoir drained through the TM, which is part of the eye's natural fluid outflow pathway.

Eyes were fully submerged in PBS for US/PA imaging. In a subset of eyes, two-dimensional (2D) US/PA images were continuously acquired during cell injections at 680 nm wavelength. Spectroscopic US/PA images were also acquired within the 680 – 970 nm wavelength range in 5 nm increments for the first 15 minutes post-injection. After 5 hours post-injection, eyes were fixed, and then 3D spectroscopic US/PA datasets were acquired

in all eyes (n=4 for each cell concentration). Due to hardware limitations, 3D US/PA images were acquired at a subset of wavelengths (680 – 710 nm wavelength range, 5 – 10 nm increments). All datasets were exported to MATLAB for post-processing. Three-dimensional volumetric US/PA images were produced using AMIRA (Thermo Fisher).

3.3.9 Trabecular meshwork dissection studies

Five-hours after cell injection, fixed eyes were dissected to isolate the anterior segment, similar to previously reported methods [145,146], to specifically assess double-labeled MSC localization at the TM. Briefly, orbital connective tissue was removed, and eyes were hemisected with a razor blade to isolate the front half of the eye. The vitreous humor and lens were removed, the iris was cut radially back to the iris root and pectinate ligaments until the TM was revealed, and the ciliary processes were carefully removed while preserving the TM. Any remaining vascularized or pigmented tissue was removed. Dissected anterior segments (n=4 for each cell concentration) were marked with stickers of black printed letters and two small pieces of dowel rod to act as fiducial markers for both fluorescent microscopy and US/PA imaging.

For US/PA imaging, dissected anterior segments were secured with the cornea facing down on top of a tissue-mimicking phantom base composed of 1% (w/v) agarose and were fully submerged in PBS. This orientation was required to maintain light delivery consistent with that of the inverted confocal microscope. Three-dimensional spectroscopic US/PA datasets were acquired in all dissected eyes (n=4 for each cell concentration) and exported to MATLAB for post-processing.

For fluorescent microscopy, anterior segments were placed in PBS on a 50 mm glass-bottomed dish (Ted Pella). Additional scleral tissue posterior to the TM was removed as needed to bring the TM in contact with the glass bottomed dish. Micrographs of the entire TM circumference were captured by confocal microscopy (LSM 700, Zeiss) as z-stacks of tile scans at 50x. Brightfield overlays were also captured. Maximum intensity projections were created for each *en face* image for further processing.

3.3.10 Spectroscopic analysis of multi-wavelength PA datasets

All PA datasets were post-processed using MATLAB. Initially, all PA datasets were spatially filtered using a 41 µm x 45 µm (3 x 3 pixel) median filter to suppress large noise fluctuations. Then, for two-dimensional spectroscopic PA datasets, a moving average filter with a spatial kernel of 252 µm x 405 µm, roughly three times the axial and lateral resolution, and a wavelength kernel of 15 nm was used. For three-dimensional spectroscopic PA datasets, the spatial kernel was extended in the elevational dimension (267 µm or 3 imaging slices), and no wavelength filtering was performed. Finally, PA signals below the noise threshold, defined as $P_{min} + 0.025\,(P_{max} - P_{\min})$ were eliminated from the dataset, where $P_{\min}$ and P_{max} are the lowest and the largest values of the PA signals, respectively.

Following filtering, PA datasets were analyzed with spectroscopic analysis using Equation 3 above (see Section 2.3.5). In this case, the resulting PA signal at each pixel, $P(x, y, \lambda)$, was assumed to be a superposition of individual PA signals from melanin, the primary endogenous absorber in the anterior eye, and AuNS-labeled MSCs. Therefore $\sigma_{a_i}(\lambda)$ is a matrix of optical cross-sections for i absorbers, melanin and AuNS-labeled

MSCs. Optical cross-sections were determined *a priori* [147], and linear least squares regression was used to produce separate concentration maps $\{C_i; i = 1,2\}$ depicting melanin or AuNS-labeled MSC localization in the anterior eye. The concentration maps, C_i, were restricted to positive values.

3.3.11 Locating stem cells in photoacoustic images

For whole, *ex vivo* porcine eyes, PA datasets were further processed to eliminate signals from stem cells that had accumulated on the lens, thus highlighting stem cells localized to the iris and the TM region, as follows. The 3D concentration maps of melanin and stem cells, obtained from spectroscopic analysis, were integrated with respect to anterior-posterior depth, thus projecting the PA signals onto a 2D plane showing absorber distribution (melanin or cells) around the circumference of the eye. To eliminate PA signals from the anterior lens, the map of melanin distribution was used to define an annular ring mask, as follows: the mask's inner border was taken to be .5 mm exterior to the inner edge of the melanin map, representing the pupillary margin, and the mask's outer border was taken as 3 mm exterior to the inner border of the mask. The map of cell distribution was then multiplied by this annular ring mask to isolate cells at the iris and in the angle.

For dissected anterior segments, the 3D concentration maps were also integrated with respect to depth to produce 2D maps of absorber distribution, and the map of melanin distribution was used to create an annular ring mask defining the TM region. Unlike the situation in whole eyes, the iris had been removed from the dissected anterior segments; thus, the melanin distribution essentially coincided with the TM, as the only remaining melanin-rich tissue. The inner border of the mask was defined to be the inner edge of the

melanin map, i.e. the anterior margin of the TM (nearest to the cornea). The outer border of the mask was defined as 1 mm exterior to the inner border to match the fluorescent image processing technique (see Section 3.3.12 below). The map of cell distribution was multiplied by this annular ring mask to isolate cells in the TM region. The signals resulting from the stickers and dowel rods, which were adhered to the cornea as fiducial markers, were removed during image processing.

3.3.12 Locating stem cells in fluorescent images

Due to inherent differences between visualization of anatomical landmarks in PA imaging vs. fluorescent microscopy, different masking methods were required to visualize stem cell distribution in the TM region by fluorescent microscopy. In dissected anterior segments an annular ring mask was created with the inner border defined to be the corneal margin, as observed in brightfield images. The outer border of the mask was defined to be 1 mm exterior to the inner border of the mask, to match the mask created for PA images. Fluorescent images were masked and exported to MATLAB for further processing. Images were filtered with the same approach used for PA image processing. Specifically, a 3 x 3 pixel median filter was used to remove noise spikes, followed by filtering using a moving average with a kernel size of 400 µm x 400 µm. The signals resulting from the stickers and dowel rods, which were adhered to the cornea as fiducial markers, were removed.

3.3.13 Evaluating laser safety in vivo

All experiments involving animals were performed under the guidelines of the Institutional Animal Care and Use Committee (IACUC) of the Georgia Institute of Technology. Female nude rats (RNU; n=2; Charles River Laboratories) with pigmented

eyes were used in these studies. Anesthesia was induced with 5% isoflurane at approximately 500 mL/min and maintained at approximately 2% isoflurane. The right eye was imaged with the Vevo LAZR system and combined US/PA images were acquired using a 50 MHz transducer. The entire eye was scanned using a three-dimensional translation motor and multi-wavelength sweeps from 700 nm – 950 nm in increments of 25 nm. The left eye was not irradiated with the laser and served as a control. After laser irradiation, rats were monitored for gross changes in ocular morphology, indicative of laser damage, and any behavioral changes. Photographs were taken of both eyes before imaging, 24 hours after laser light irradiation, and 1 week after laser light irradiation. US/PA datasets were exported to MATLAB for post-processing. Three-dimensional volumetric images were created using AMIRA.

3.3.14 Synthesis of Prussian blue nanocubes

Prussian blue nanocubes (PBNCs) were produced using previously reported methods.[148] All reaction components were used as received. Briefly, PBNCs were synthesized via a seed-mediated method using superparamagnetic iron oxide nanoparticle (SPION) precursors (Ocean NanoTech). SPIONs with a 10 nm diameter served as a source of iron to form cubic nanoparticles. The reactant, 5% by potassium hexacyanoferrate (II) trihydrate (Sigma-Aldrich) by mass in DIUF water, and catalyst, 5% by volume of 37% HCl (Sigma-Aldrich) in DIUF water, were prepared. While stirring, 60 mg of SPIONs were added to 150 ml of DIUF water, followed by 7.5 ml of the reactant and 2.5 ml of the catalyst. The reaction was stirred for at least 1 hour. PBNCs were dextran coated by adding 10 mg of dextran/mg of Fe. TEM (Hitachi HT7700 TEM, IEN/IMAT Materials Characterization Facility, Georgia Institute of Technology) was used to characterize PBNC

morphology. The optical absorption spectrum was measured using UV-Vis spectrophotometry (Evolution 220 Spectrophotometer, Thermo Scientific). MSCs were labeled with PBNCs at an optical density of 2 following the same protocol used for labeling stem cells with gold nanospheres (see Section 3.3.3 above).

3.3.15 Image-guided magnetic delivery of stem cells in vivo

All experiments involving animals were performed under IACUC guidelines of the Georgia Institute of Technology. Albino, female nude rats (NIH; n = 2; Taconic) were used in these studies. Thus, eyes were not pigmented. To prepare for the procedure, ring magnets (H125D; Amazing Magnets) were submerged in a vial containing 70% ethanol overnight. In addition, a nitrile glove was cut into small squares (approximately 1 cm x 1 cm). Each square had a small slit cut in the middle, which was approximately the size of a rat eye, and were submerged into a second vial containing 70% ethanol to clean. Anesthesia was induced with an injection of ketamine (75 mg/kg) and dexdomitor (.5 mg/kg). Only half of the recommended dose was administered, and then the rat was prepared for the procedure. The rat was placed on its side on a heating pad covered with a sterile drape under a dissecting microscope. A tetracaine drop was delivered to the surgical eye (the right eye). Once the rat reached the surgical plane, the right eye was injected with PBNC-labeled MSCs. One rat received PBNC-labeled MSCs only. The second rat received PBNC-labeled MSCs and a ring magnet placed around the TM for three hours. The contralateral eye (left eye) of both animals was untreated. Injections were delivered as follows.

A 31G insulin syringe (BD) was filled with a 25 µl volume of PBNC-labeled MSCs at 1000 cells/µl. One of the pre-cut squares was removed from the ethanol and dried on the sterile drape. The right eye was proptosed by pushing the eye through the slit in the middle of the square. Next, the needle was carefully inserted through the cornea from the nasal side of the eye with the bevel facing up. The syringe plunger was quickly depressed. After the injection, the needle remained in the eye for 1 minute to avoid reflux. The needle was then removed, and the square was pulled off of the eye. For the rat that received a ring magnet, prior to the injection the magnet was removed from the ethanol vial, briefly dried, and placed around the proptosed right eye. Thus, the eye was injected while the magnet was in place. After the injection, the ring magnet was briefly removed to pull off the square, but was immediately returned to the eye. Sterile saline drops were administered to both eyes to moisturize. After 3 hours post-injection in both animals, 3D volumetric US/PA datasets were acquired with the Vevo LAZR system using the 50 MHz transducer from 700 – 950 nm wavelengths in 25 nm increments. The diagram in Figure 9 depicts the method used in the aforementioned *in vivo* studies.

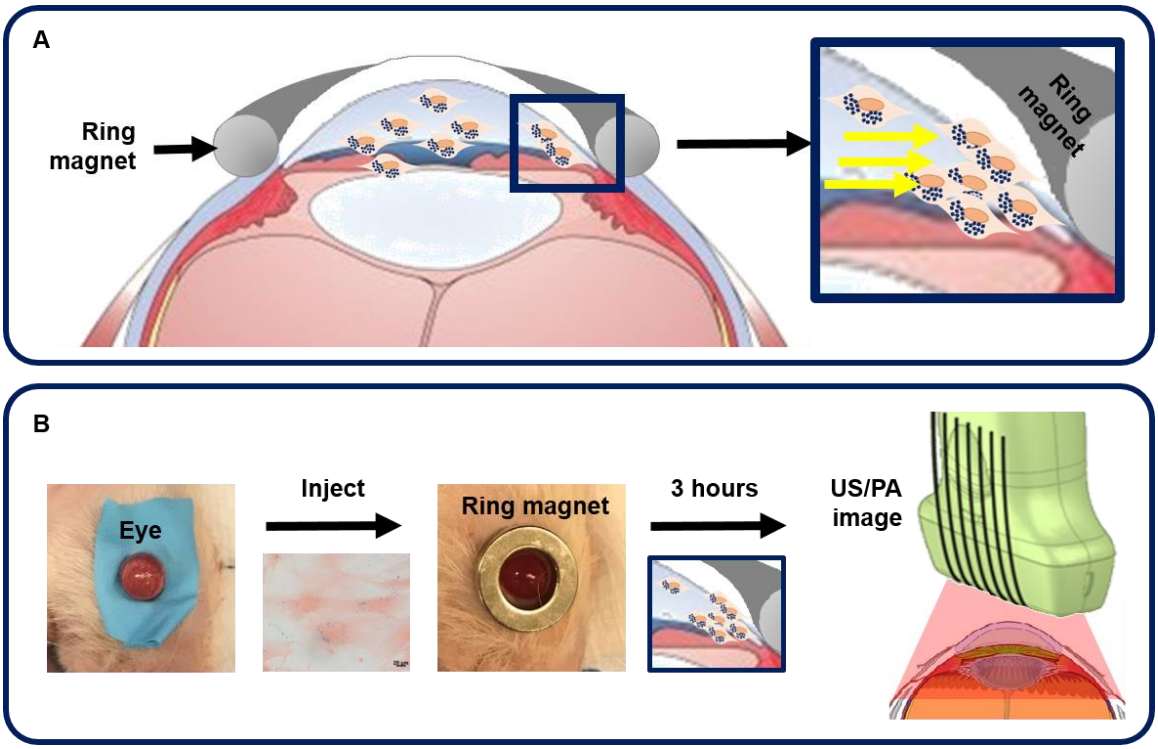

Figure 9. Diagram of the method of image-guided magnetic delivery of PBNC-labeled stem cells to the TM. Cartoon depicts PBNC-labeled stem cells being pulled to the TM using a ring magnet (A). Schematic of the *in vivo* procedure in rats (B). The eye was proptosed, and a ring magnet was placed over the eye while 25 µl of PBNC-labeled stem cells (1000k cells/µl) were injected into the eye. The magnet was in place for 3 hours post-injection followed by US/PA imaging.

Photographs were taken before and after injections and US/PA imaging. After imaging, rats were sacrificed, and eyes were enucleated. US/PA datasets were exported for post-processing using MATLAB, and 3D volumetric images were created in AMIRA.

3.4 Results

3.4.1 Characterization of gold nanospheres and stem cell labelling

Gold nanospheres to label stem cells for photoacoustic imaging were successfully synthesized, as verified by TEM (Figure 10A) and UV-Vis spectrophotometry (Figure

10B). The average hydrodynamic diameter and surface charge of AuNSs were determined using DLS and zeta-potential, respectively. The AuNSs had an average hydrodynamic diameter of 17.89 nm +/- 6.4 nm with an average poly-dispersity index of 0.106 +/- 0.020. The average surface charge of AuNSs was -29.7 mV +/- 11 mV. Both results agreed with previous reports [142].

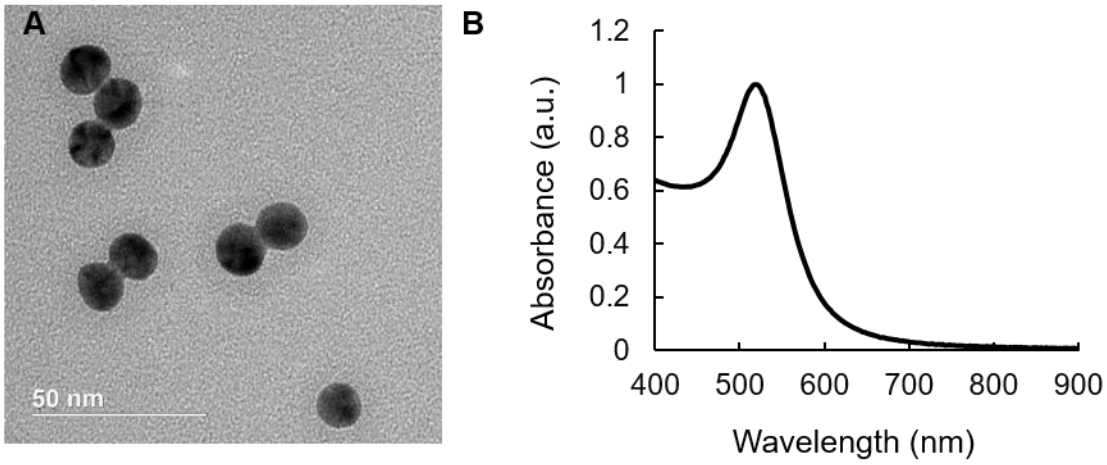

Figure 10. Characterization of gold nanospheres. (A) TEM confirmed uniform particle morphology and particle diameter of approximately 20 nm. (B) UV-Vis spectrophotometry of AuNSs with a peak absorbance at 520 nm.

Brightfield microscopy confirmed successful labeling of stem cells with AuNSs after incubation with nanoparticles for 24 hours *in vitro* (Figure 11C–E) compared to naïve (unlabeled) stem cells (Figure 11A–B). UV-Vis spectrophotometry further confirmed successful stem cell labeling based on changes in optical properties (Figure 11F). AuNS-labeled MSCs showed a peak at ~700 nm. Although AuNSs typically absorb at ~520 nm wavelength, surface plasmon resonance coupling upon particle endocytosis caused a red-shift in the peak absorption [149].

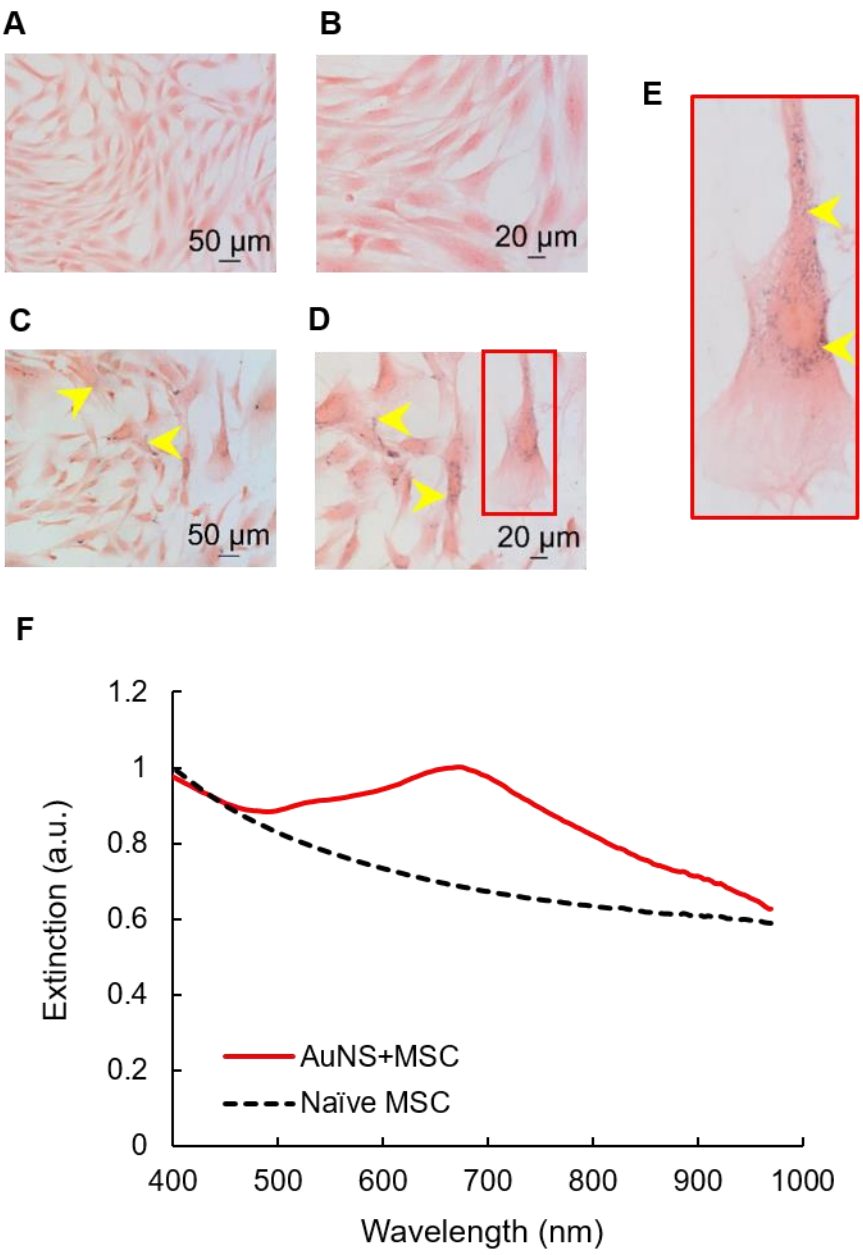

Figure 11. MSC labeling with gold nanospheres. Brightfield micrographs of eosin-stained naïve (unlabeled) MSCs (A, B) and AuNS-labeled MSCs (C–E). (E) Enlarged image of the region of interest defined by the red box in (D). Yellow arrows identify AuNSs (black spots). (F) UV-Vis spectrophotometry comparing the spectral signature of naïve (black, dashed line) and AuNS-labeled MSCs (red, solid line).

Prior to proceeding with imaging experiments, AuNS-labeled MSCs were further characterized by assessing differentiation to assure the nanoparticles did not impact

multipotency (Figure 12). Adipogenic or osteogenic differentiation were induced in AuNS-labeled MSCs. Brightfield microscopy showed changes in cell morphology upon differentiation (Figure 12A and 12D) compared to naive MSCs (Figure 12G). Oil Red O staining confirmed adipogenesis (Figure 12C), indicated by red stained lipid vesicles (Figure 12C). Von Kossa staining confirmed osteogenesis, indicated by black staining of calcium deposits (Figure 12E). Overall, gold nanospheres did not appear to impact stem cell multipotency, which agrees with previous results.[150,151]

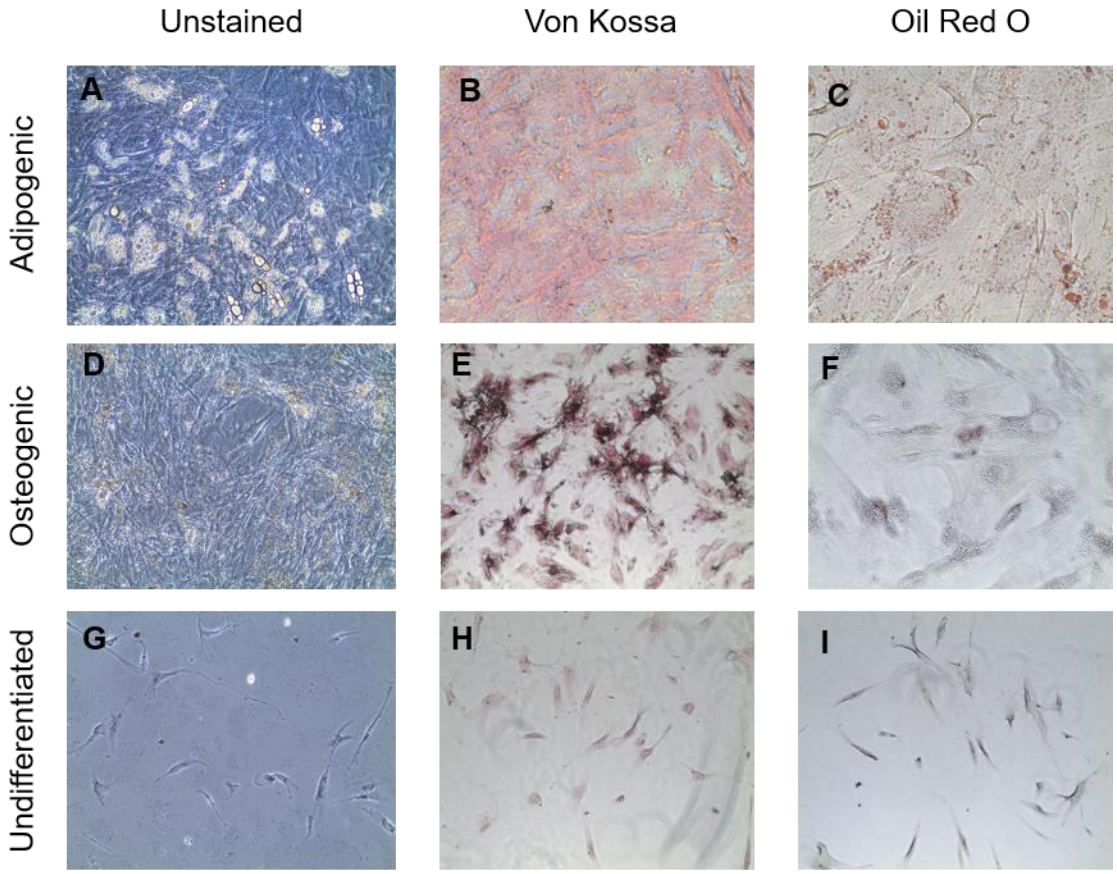

Figure 12. AuNS-labeled MSCs maintain multipotency. MSCs were labeled with AuNSs followed by adipogenic (A – C) or osteogenic (D – F) differentiation and compared to AuNS-labeled MSCs that were fed maintenance media on the same schedule (G – I). Columns left to right: no (A, D, G), Von Kossa (B, E, H), and Oil Red O staining (C, F, I).

After characterizing nanoparticles and labeled stem cells, photoacoustic properties of AuNS-labeled MSCs were assessed. Tissue-mimicking phantom experiments showed that AuNS-labeled MSCs had an increased PA signal at 700 nm wavelength compared to naïve MSCs (Figure 13A and 13B). A representative PA spectrum of AuNS-labeled MSCs was compared to melanin, the primary endogenous absorber in the anterior segment (Figure 13C).[147] Surface plasmon resonance coupling, initially observed from UV-Vis spectrophotometry, was also observed with photoacoustic imaging, indicated by absorption of AuNS-labeled MSCs well-beyond 700 nm wavelength (Figure 13C). Most importantly, the PA spectra were distinct, e.g., having different slopes. This supported the feasibility of AuNS labeling to identify and track stem cells within the anterior segment without interference from melanin signal.

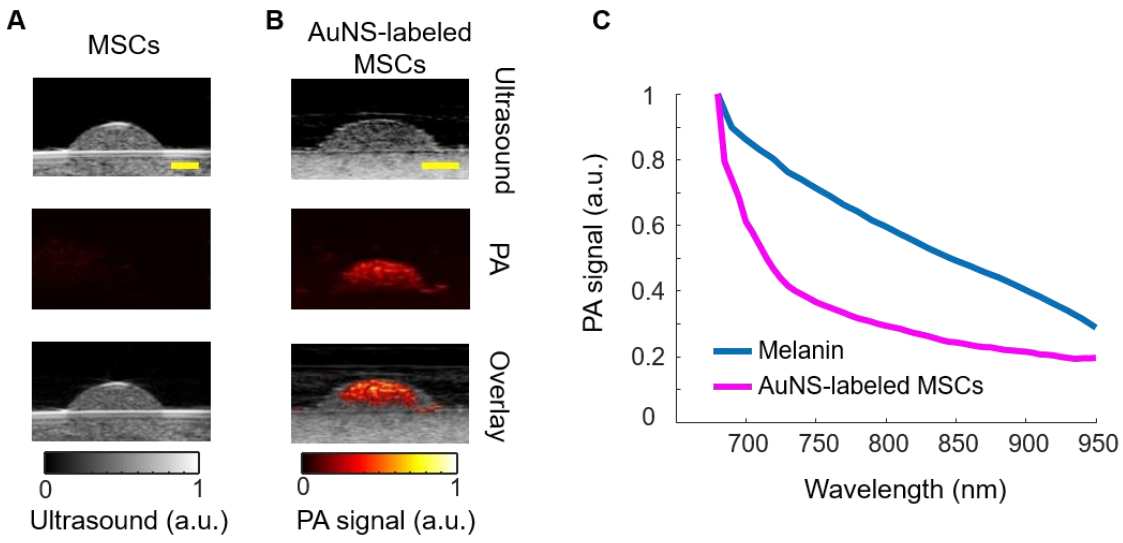

Figure 13. Photoacoustic properties of AuNS-labeled MSCs. Ultrasound (grayscale), photoacoustic (color scale), and overlay images at 700 nm wavelength for (A) unlabeled MSCs and (B) AuNS-labeled MSCs. Scale bar = 2 mm. (C) Representative PA spectrum of melanin at the iris and AuNS-labeled MSCs. The distinct spectra, notably differences in slope, make AuNSs a promising contrast agent choice for stem cell tracking in the anterior segment, where melanin is the major PA signal source.

Further *in vitro* analysis was conducted with stem cells in agarose phantoms, a simplified system that allowed us to evaluate the ability of US/PA imaging to detect cells under well-controlled conditions and compare to fluorescent microscopy (Figure 14). Cells were labeled with both CFSE, a fluorescent dye, and AuNSs (termed "double-labeled MSCs"). Known numbers of double-labeled MSCs were suspended in agarose gel phantoms at several different concentrations. Triplicates were prepared for each cell concentration. All agarose gels were imaged by confocal microscopy and PA imaging to produce 3D datasets. Although our PA imaging system has a light penetration depth of more than 20 mm, a region of interest with a depth of 0.5 mm was used to enable a fair comparison to confocal fluorescent microscopy, which has more limited light penetration. When comparing total PA signal to cell number loaded into the phantom, a linear relationship was observed ($R^2 = 0.94$), as was the case when comparing fluorescent signal to cell number ($R^2 = 0.98$). The lower detection limits were approximately 10k cells/ml and 5k cells/ml for PA and fluorescence, respectively. Therefore, PA imaging is a viable option for minimally invasive, longitudinal monitoring, and information provided is comparable to that of existing fluorescent cell tracking techniques, with the added benefit of increased light penetration.

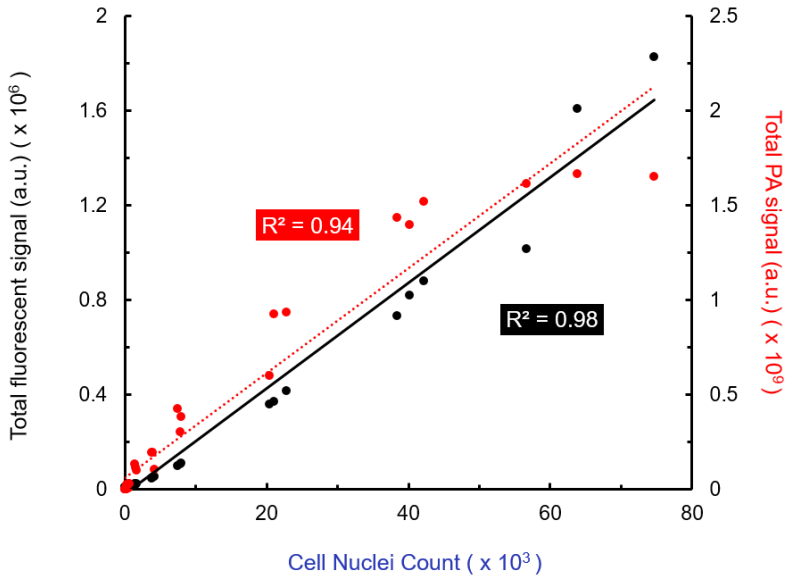

Figure 14. PA and fluorescent imaging signals vs. cell number loaded into agarose gel phantoms. Double-labeled MSCs (labeled with AuNSs and CFSE) were suspended at known concentrations in agarose gels formed in 48 well plates. Triplicates were prepared for each cell concentration. Total fluorescent and total PA signal were compared to cell nuclei count (DAPI staining) over a depth of 0.5 mm. Each point represents total signal for one gel. PA and fluorescent microscopy produced similar results, which further motivates use of minimally invasive PA imaging to track stem cells in the anterior segment.

3.4.2 Stem cell detection in perfused porcine eyes

We next carried out studies in perfused whole porcine eyes, which are an excellent model system due to similar pigmentation and anatomy to the human eye [152,153]. A physiological pressure was imposed using an elevated reservoir to mimic the *in vivo* secretion and flow of aqueous humor throughout the anterior chamber (Figure 8). Thus, after injection, stem cells were allowed to circulate in the anterior chamber because inflowing media from the elevated reservoir continuously flowed out through the trabecular meshwork, which is part of the eye's natural fluid drainage pathway.

AuNS-labeled MSCs were injected through the cornea into the anterior chamber. Real-time, single wavelength PA imaging visualized the stem cell injection and circulation

through the chamber for the first 15 minutes post-injection (Figure 15A – D), showing potential for image-guided delivery. However, single-wavelength PA imaging did not distinguish the AuNS-labeled stem cells from background signals from melanin-rich tissues, such as the iris and TM (Figure 15A). Thus, multi-wavelength PA imaging and spectroscopic analysis were required.

We distinguished AuNS-labeled MSCs from background (melanin) signal using multi-wavelength PA imaging and spectroscopic analysis. Prior to injection of AuNS-labeled MSCs, melanin was accurately localized to the iris and TM (Figure 15E), and no cells were identified (Figure 15I), indicating minimal cross-talk between the spectra of melanin and AuNS-labeled MSCs. Immediately post-injection, AuNS-labeled MSCs and melanin could also be distinguished (Figure 15F–H and 15J–L). Some PA artifacts were also observed. For example, because the imaging plane was positioned to visualize the syringe needle, it was not necessarily centered over the pupil and was closer to the pupillary margin, where out-of-plane light absorption from the iris can occur. This created a PA signal artifact that appeared at the surface of the lens (Figure 15A), which can be removed by 3D imaging of the eye. In addition, the syringe needle produced a PA signal at the center of the anterior chamber (Figure 15E–H) [154].

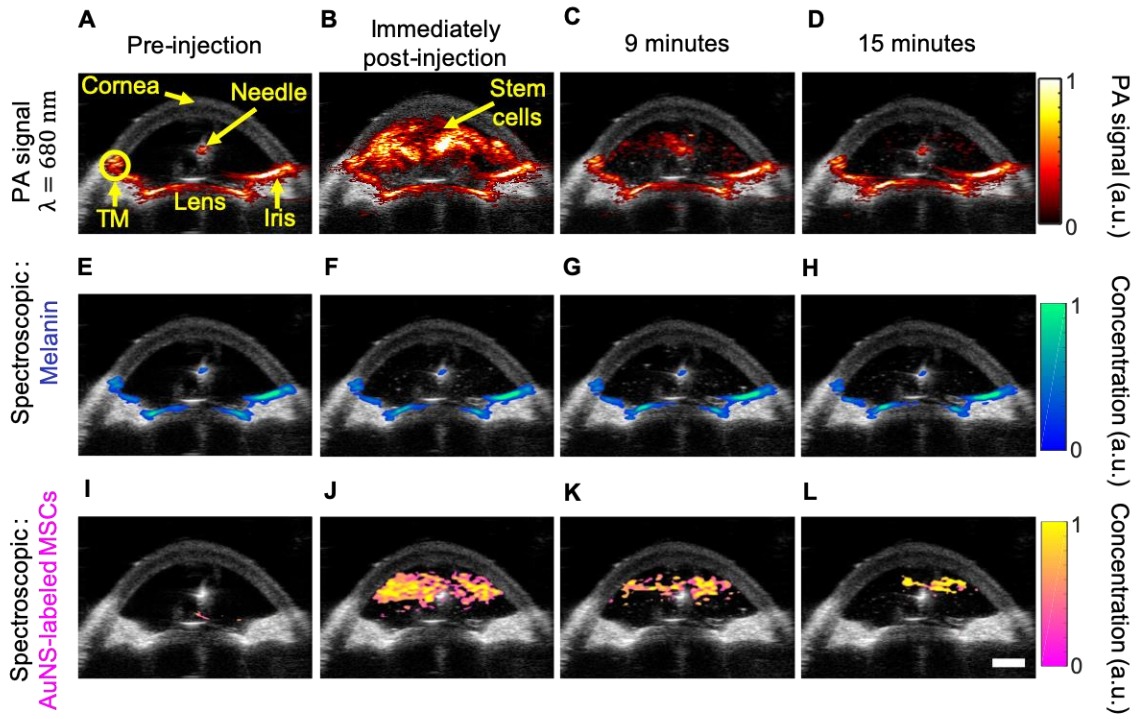

Figure 15. Ultrasound and photoacoustic imaging of AuNS-labeled MSCs delivered into the anterior chamber of perfused porcine eyes *ex vivo*. (A) Anatomical landmarks were identified, including the TM. PA datasets were analyzed before injection, and immediately, nine, and fifteen minutes post-injection (columns left to right). (A - D) PA imaging at 680 nm wavelength. (E - L) Spectroscopic analysis of multi-wavelength PA datasets distinguished signals from endogenous absorbers and AuNS-labeled MSCs. Pixels identified as melanin (E – H) and AuNS-labeled MSCs (I - L). Scale bar = 3 mm.

Stem cells were similarly injected into the anterior chamber of perfused porcine eyes and allowed to circulate for 5 hours, which is sufficient time for complete exchange of all fluid in the anterior chamber due to flow resulting from fluid drainage through the trabecular meshwork. To assess differences in delivery efficiency, injections were carried out with low, medium, and high cell numbers (250k, 500k and 1000k cells, respectively). Multi-wavelength US/PA imaging and spectroscopic analysis was able to distinguish melanin and stem cells at 5 hours post-injection (Figure 16). When 250k stem cells were injected, few cells were visible at 5 hours, and those that could be seen were primarily

localized to the anterior lens (Figure 16C and 16D). As cell numbers increased, stem cells began to coat the iris and reach the angle (Figure 16F and 16H). In general, poor delivery efficiency was observed.

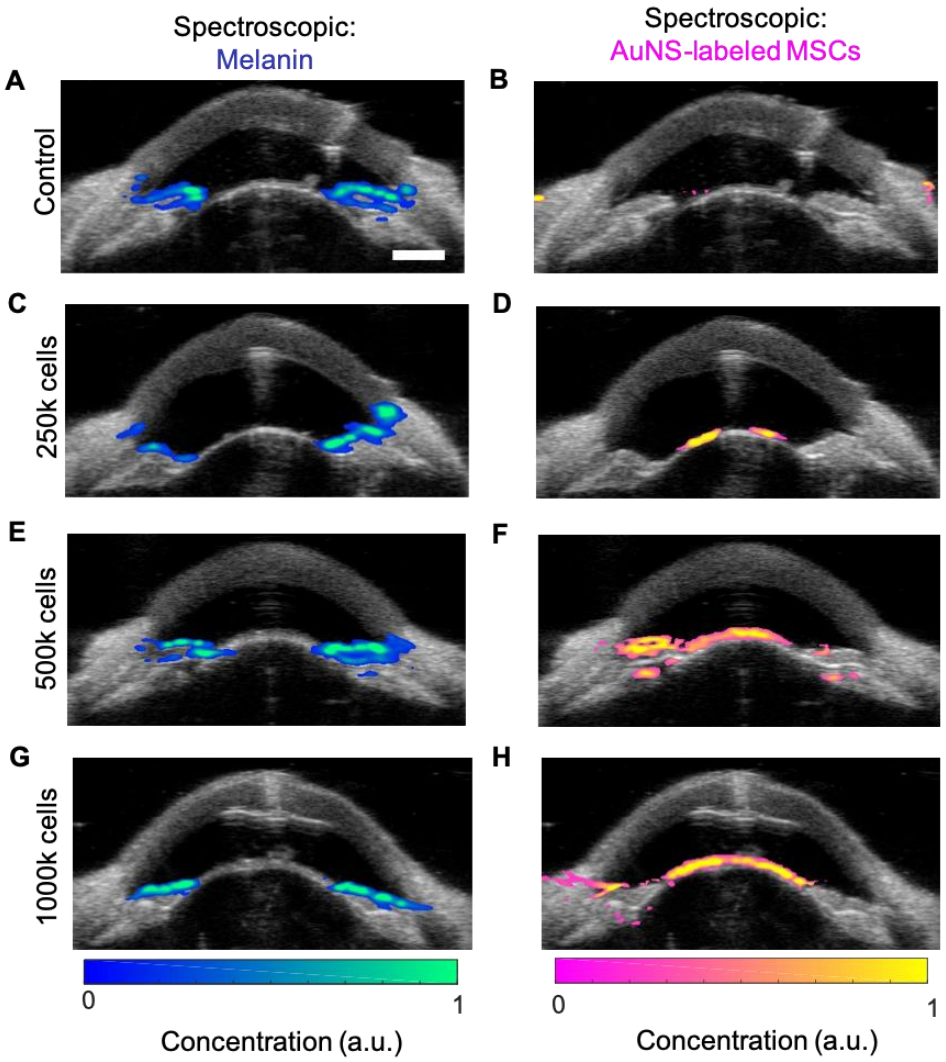

Figure 16. Ultrasound and PA imaging detects AuNS-labeled MSC location five hours post-injection in perfused porcine eyes *ex vivo*. Multi-wavelength PA datasets were processed with spectroscopic analysis. The left and right columns show PA signals separated according to contribution of melanin (A – G) and AuNS-labeled MSCs (B – H). Each row corresponds to different numbers of cells injected: (A, B) control (perfused with media for 5 hours, no cells injected), (C, D) 250,000 cells, (E, F) 500,000 cells, and (G, H) 1,000,000 cells. Most AuNS-labeled MSCs were detected on the anterior lens, but some reached the angle for the 500k (F) and 1000k (H) cell injections. Scale bar = 3 mm.

Although the 2D US/PA imaging results above provided useful information, 3D imaging was required to more accurately localize stem cells, due to spatially non-uniform flow in the anterior chamber and through the TM. Three-dimensional multi-wavelength US/PA imaging at 5 hours post-injection and spectroscopic analysis confirmed 2D results (Figure 17A and 17B). Specifically, stem cells primarily accumulated on the anterior lens (Figure 17B). Three-dimensional volumes were then segmented via geometric masking to eliminate stem cell signals at the lens (Figure 17C), with the inner and outer margins of the ring mask corresponding to .5 mm external to the pupillary margin and the irideo-corneal angle, respectively. Strong stem cell signals at the lens suppressed weaker PA signals from stem cells at other anterior tissues, where fewer cells accumulated. Masking allowed better visualization of stem cell localization near the irideo-corneal angle, permitting circumferentially non-uniform stem cell distribution to be observed.

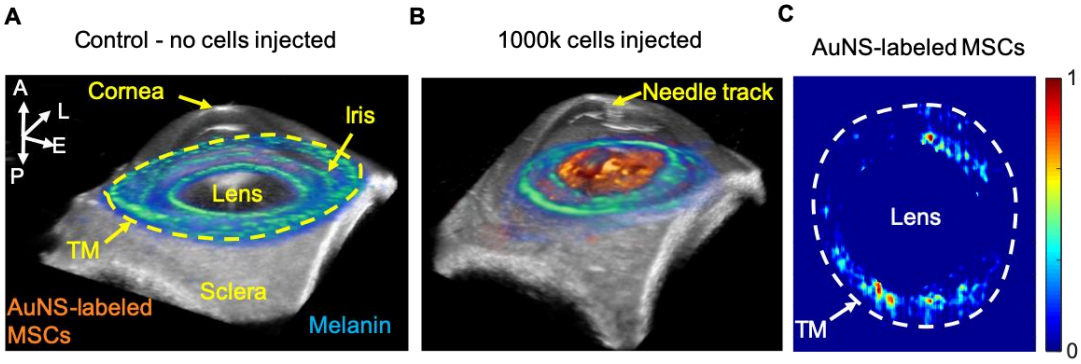

Figure 17. Three-dimensional US/PA imaging to detect location of AuNS-labeled MSCs at five hours post-injection. (A, B) Overlays of ultrasound (grayscale) and spectroscopic PA (color scale) images. Spectroscopic PA analysis distinguished melanin (cool color map) and AuNS-labeled MSCs (hot color map). (A) Control, (perfused with media, no cells injected). (B) 1000k cells injected. AuNS-labeled MSCs accumulated on the anterior lens and iris. (C) Spectroscopic datasets were further processed to identify AuNS-labeled MSCs at the iris and the TM region. Non-uniform stem cell delivery around the circumference of the iris and TM was observed. A = anterior; L = lateral; E = elevational; P = posterior.

At five hours post-injection, intact porcine eyes were hemisected, and extraneous tissues were removed to leave a shell containing only the TM, cornea, and anterior sclera. Dissected anterior segments were used to evaluate capabilities of existing fluorescent microscopy techniques and photoacoustic imaging to track double-labeled stem cells. Image post-processing and electronic masking specifically showed stem cells in the TM region (Figure 18). Four dissected anterior segments for each cell concentration were imaged using both modalities. Non-uniform stem cell distributions around the circumference of the TM were observed with both modalities, with some degree of, but less than perfect, overlap (see representative images in Figure 18).

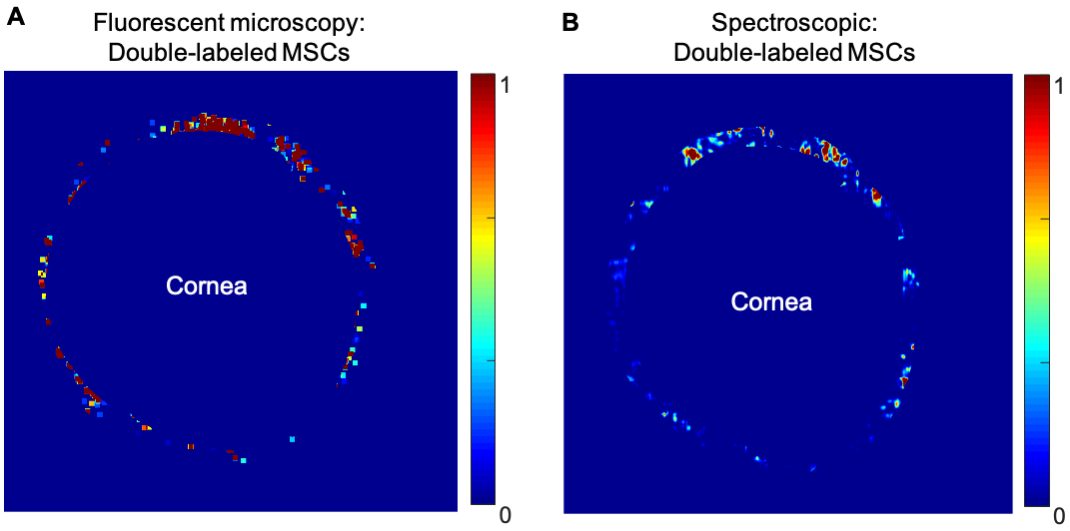

Figure 18. Comparison of the distribution of MSCs as visualized by confocal fluorescent microscopy (A) and spectroscopic PA imaging (B) in dissected porcine anterior segments. MSCs were double-labeled with a fluorescent marker (CFSE) and AuNSs. Images show stem cell distribution around the circumference of the TM.

3.5 Discussion

This study shows proof-of-concept for the ability of a US/PA tracking platform to longitudinally monitor stem cell delivery in the anterior eye. We labeled stem cells with

AuNSs for PA imaging and injected them into the anterior chamber of perfused porcine eyes *ex vivo*. We were able to detect stem cell delivery and circulation in the anterior chamber in real-time using single-wavelength PA imaging. The more powerful multi-wavelength PA imaging and spectroscopic analysis were able to distinguish AuNS-labeled MSCs from background signals, laying the groundwork for future *in vivo* studies. Results support further development of our US/PA platform as a tool to supplement information from existing tracking methods, with the significant advantage of allowing minimally invasive longitudinal imaging.

Gold nanospheres were used to label stem cells for several reasons. The first important aspect is cytocompatibility; AuNSs have previously been shown to have minimal effects on stem cell differentiation and viability [142]. Second, this is an efficient way to detect labeled cells due to surface plasmon resonance coupling of gold nanospheres upon endocytosis [149]. Without particle aggregation within cellular vesicles, free AuNSs absorb at ~ 520 nm and would not be detected within the 680 – 970 nm wavelength range. Third, the PA spectrum of AuNS-labeled stem cells was also distinct from background PA spectra of tissues in the anterior eye [147], further supporting the use of AuNSs to detect stem cells. Previous work showed AuNS-labeled MSCs injected in muscle could be detected at up to 10 days post-injection [53], indicating potential for longitudinal *in vivo* imaging in ophthalmic applications.

Although our initial studies were successful with AuNSs, many other contrast agents exist for labeling and tracking cells with PA imaging, including organic nanomaterials [155,156], dyes [157], other metallic nanoparticles [18,21,158], and photomagnetic nanoparticles [126,138]. The use of dyes is appealing because the small molecules can be cleared; however,

dyes are prone to photobleaching, which may limit longitudinal imaging [15]. Beyond gold nanospheres, nanoparticle material, shape, and size can be varied to produce a more distinct PA spectrum to better detect stem cells in the presence of background signal from adjacent tissues [15]. For ophthalmic applications, gold nanorods are also of interest; however, potential instability and cytotoxicity are disadvantages compared to gold nanospheres [159,160]. Beyond detection, the use of photomagnetic nanoparticles has appealing qualities for other purposes, such as multi-modal imaging or magnetic steering [126].

In agarose gel phantom experiments, fluorescent microscopy and PA imaging were equally effective at detecting double-labeled stem cells (AuNS and CFSE). These experimental conditions favored fluorescent microscopy, since no additional optical scatterers were introduced into the gel (unlike the situation in the eye) and a region of interest with a depth of only 0.5 mm was selected to accommodate the limited light penetration of fluorescent microscopy. In the anterior eye, the presence of highly scattering tissues, such as the sclera, and strong melanin absorption, will further reduce light penetration. Thus, implementing purely optical imaging methods to monitor stem cells in the anterior segment may be challenging. Although our current PA imaging system cannot detect single stem cells, clinically relevant cell concentrations could be detected in agarose gels and *ex vivo* porcine eyes with highly scattering tissues intact. The ability to image intact ocular tissues was a key advantage of PA imaging compared to confocal fluorescent microscopy, which required dissection of porcine eyes to image the TM and visualize stem cells. As a result, PA imaging can potentially facilitate minimally invasive, longitudinal stem cell tracking *in vivo* in the future.

In dissected samples from whole eyes, agreement between confocal fluorescent microscopy and PA imaging results was reasonable but not perfect, which we believe can be explained by several reasons. First, different masking methods were required for each modality because visualization of anatomical landmarks differed, and it was impossible to precisely align the masks despite our best efforts. Second, fluorescent microscopy could potentially detect single cells, while US/PA imaging detected groups of cells. Third, due to sensitivity of confocal imaging to light attenuation, which limits imaging depth, we had to dissect away tissue to visualize the TM because of the presence of highly scattering and pigmented tissues in the eye's anterior segment. This dissection may have also slightly disturbed the remaining tissues and the labeled cell distributions. For these reasons, we concluded that confocal fluorescent microscopy was unfortunately an imperfect comparison for our PA stem cell tracking platform in whole eyes. However, because fluorescent microscopy is currently used as an assessment tool for monitoring stem cell delivery and is also an absorption-based modality like PA imaging, we believe it was the most reasonable modality to attempt comparison.

Multi-wavelength PA imaging and spectroscopic analysis distinguished AuNS-labeled stem cells from background signals (primarily melanin) in 2D cross-sections and in 3D volumetric images. Although studies were conducted in *ex vivo* porcine eyes, we implemented flow in the eye to mimic the *in vivo* environment where there is a continuous circulation of fluid in the anterior eye. By 5 hours post-injection, AuNS-labeled MSCs accumulated primarily on the anterior lens. At higher cell numbers (500k and 1000k), some stem cells reached the angle, where the TM is located, but challenges with delivery efficiency were apparent. The US/PA tracking platform clearly highlighted poor delivery

efficiency to the TM target tissue. Thus, US/PA tracking provided valuable information regarding stem cell localization. As the platform is translated to longitudinal *in vivo* studies, correlating stem cell localization and migratory patterns with changes in intraocular pressure, one indicator of glaucoma risk, can provide valuable information to better design stem cell therapies.

3.6 Conclusions

We demonstrate a US/PA imaging platform that can provide longitudinal feedback to assess MSC delivery in the anterior eye. Compared to existing stem cell detection techniques in the anterior eye, namely histology and/or confocal microscopy, which requires time-consuming, destructive sample preparation, US/PA tracking was minimally invasive and could be implemented in intact porcine eyes. Thus, US/PA tracking can provide additional, more holistic information on therapy progression to researchers and clinicians. Initial results also showed poor stem cell delivery efficiency, highlighting opportunities for future development of a theranostic US/PA platform to expedite therapy development and clinical translation.

3.7 Future Work

The key next steps for advancing the US/PA imaging platform for monitoring stem cell therapies for the anterior eye are assessing laser safety, improving poor delivery efficiency, and executing *in vivo* studies in small animal models. Feasibility of all aspects have been assessed in preliminary experiments detailed herein.

Development of custom ophthalmic US/PA imaging hardware, specifically high frequency transducers and focused light delivery systems, will be critical for small animal imaging, clinical translation, and safety of anterior ocular US/PA imaging systems [161,162]. Our current imaging set up using the Vevo LAZR US/PA imaging system is not ideal for ophthalmic applications. One issue is the resolution of the transducer. The highest available transducer frequency for this system is 50 MHz, which leads to a resolution of approximately 100 μm. In clinical studies in humans, others report using 35 - 80 MHz transducers to visualize detailed anterior segment anatomy, such as the trabecular meshwork.[163] This highlights clear hardware inadequacies for small animal studies in rats and mice, where the diameter of the eye is only several millimeters compared to ~ 2 cm in large animal models and humans. Thus, compatibility of the US/PA imaging system with high frequency transducers is desired.

Another issue is light delivery. The current US/PA imaging system irradiated the entire anterior segment. For initial studies, this was beneficial by allowing assessment of off-target stem cell localization due to rapid acquisition of 3D datasets to create volumetric US/PA images. On the other hand, technical challenges were also introduced by irradiating the entire anterior segment. From an image processing perspective, stem cell detection was more challenging due to background PA signals outside the region of interest, the TM. More imaging artifacts were also introduced by irradiating extraneous tissues. Most importantly, irradiating the entire anterior segment raised safety concerns due to the potential for unintentional, unnecessary laser light irradiation of the retina.

To inform design of a custom light delivery and US/PA imaging system in the future, laser parameters of our existing system were compared to other laser-based

technologies specifically designed for ophthalmic applications. Table 1 summarizes parameters of a pulsed laser system designed for retinal imaging [164] and a clinical system [165–167] used for laser trabeculoplasty procedures. The retinal imaging system from the literature (referred to as the "literature system") evaluated ocular damage caused by a pulsed, femtosecond laser at 730 nm wavelength, and light was focused to a 3.5 μm diameter spot size directly onto the retina.[164] Our current system has a 2 cm^2 spot size that is focused at the anterior segment, which is inherently less risky. Results for the literature system indicated that average powers below 68 mW at the retina caused no damage to photoreceptors.[164] Although our system has an incident average power of 260 mW, the retina would be exposed to lower power due to light absorption from melanin and scattering at the sclera. Exact values for our system can be determined by modeling. However, it is important to note that PA signals were not observed at ocular structures posterior to the iris in our *ex vivo* porcine studies (Figure 2 and Figure 15), which indicated limited light delivery to the retina.

From a safety perspective, using the lowest possible laser power is ideal. However, from an imaging perspective, using the highest possible laser power is ideal to increase imaging sensitivity and detect low concentrations of stem cells. Developing a US/PA imaging system that focuses light at the angle to irradiate the TM can balance imaging and safety requirements. A relevant system to inform design is currently used in clinic for laser trabeculoplasty (Table 1).[165–167] In laser trabeculoplasty, a goniolens focuses light at the angle, where the TM is located. By focusing light at the TM, higher average power is allowed because risk of off-target irradiation at the retina is minimized. Compared to the Vevo LAZR and femtosecond retina system, laser trabeculoplasty has approximately a 5-

fold and 15-fold higher average power, respectively. Note that the goal of laser trabeculoplasty is to induce slight damage of the TM to stimulate healing. However, even at the high power used in laser trabeculoplasty, off target damage at the retina is avoided with focused light delivery, and higher laser powers are allowed with laser trabeculoplasty. Ultimately lower laser power would be needed for US/PA imaging purposes, but focused light delivery allows more flexibility in determining parameters. Overall, parameters for retinal imaging and laser trabeculoplasty provide an excellent starting point for design of our custom light delivery system in the future.

Table 1. Comparison of laser parameters used in relevant ophthalmic applications.

Parameter	Vevo LAZR	Literature report	Clinical system – laser trabeculoplasty
Wavelength (nm)	750 nm	730 nm	532 nm
Spot Size	2 cm^2	3.5 μm diameter	400 μm diameter
Pulse duration	7 ns	55 fs	3 ns
Energy/pulse	13 mJ	.85 nJ	.3 to 2.0 mJ
Exposure duration	200 ms	94 ms	300 ms
Peak power in one pulse	1.86 kW	15.5 kW	.467 kW
Average Power	260 mW	68 mW	1000 mW

Prior to developing any custom hardware, initial assessments were conducted *in vivo* using the Vevo LAZR system to assess safety of the current system in practice. Three-dimensional multi-wavelength US/PA datasets were acquired of the right eye in nude rats (n = 2) using the 50 MHz transducer at the highest laser power possible, 13 mJ, with the Vevo LAZR. The contralateral eye was not irradiated. Rats were observed for behavioral changes, and photographs were taken of both eyes before, 24 hours, and 1 week after laser

light irradiation to evaluate any gross changes in ocular morphology, especially opacity (Figure 19). No differences in behavior, morphological changes, or ocular clouding indicative of ocular damage were observed. The white line across the eye in Figure 19B is the rat's whisker. To fully characterize damage, histology is required to assess retinal changes and an optomotor response test can determine visual function. However, initial studies provided encouraging results as no obvious, extreme damage was observed.

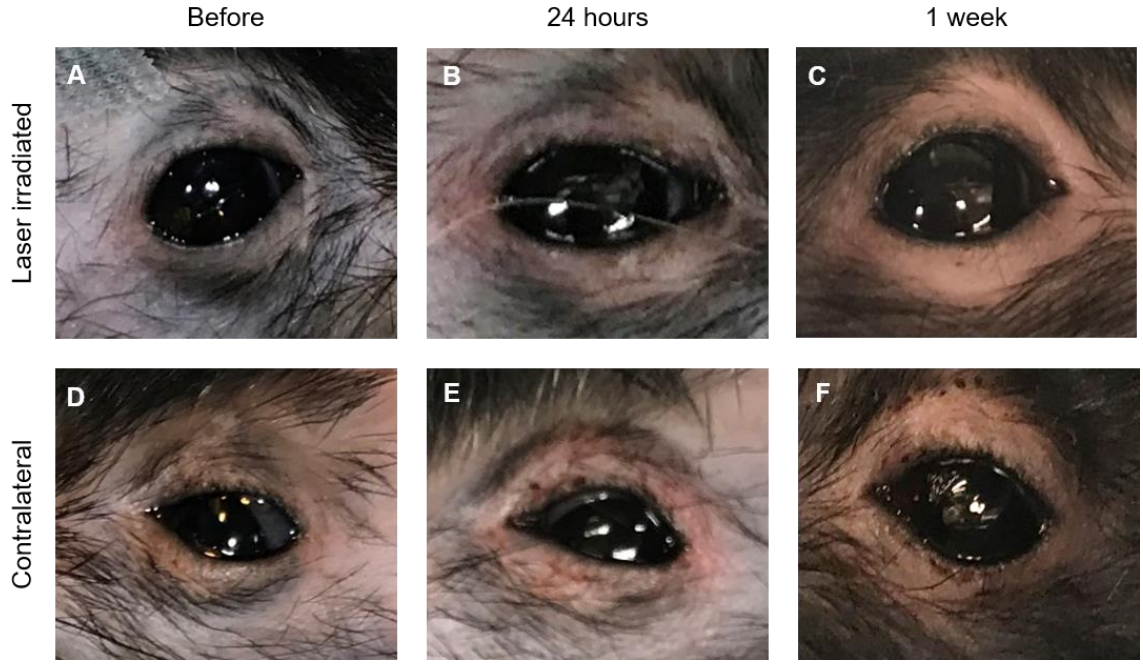

Figure 19. Assessing laser safety *in vivo.* Rats (n = 2) were anesthetized for combined US/PA imaging using the Vevo LAZR. The entire right eye was irradiated (A – C) according to the parameters in Table 1 from wavelengths of 700 – 950 nm in 25 nm increments. The contralateral eye was not irradiated (D – F). Photos were taken of both eyes before laser light irradiation (A, D), 24 hours (B, E), and 1 week after laser light irradiation (C, F). No gross changes indicative of ocular damage were observed in either eye.

In vivo US/PA datasets from the safety study were post-processed to assess image quality using the 50 MHz transducer and laser light irradiation of the entire anterior segment (Figure 20). Anatomical features, such as the cornea, iris, eye lid, and angle were

identifiable in two-dimensional US/PA images, and PA signals from melanin were also observed at the iris (Figure 20A). However, three-dimensional US/PA images were difficult to decipher (Figure 20). High background signals from black fur surrounding the eye created imaging artifacts and suppressed PA signals from relevant anterior segment structures. This can be noted by the fact that PA signals were not observed throughout the iris (Figure 20B). Overall, to strike a balance between safety, development of a clinical system, and improved image quality, focused light delivery is needed.

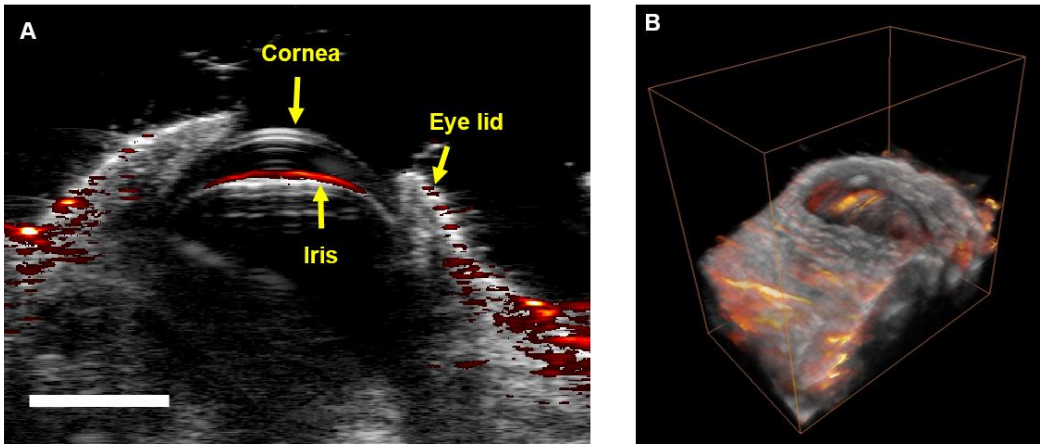

Figure 20. Ultrasound and photoacoustic images of rat eyes *in vivo*. Representative two- (A) and three-dimensional (B) ultrasound (grayscale) and PA (color scale) overlay images acquired with the Vevo LAZR and 50 MHz transducer. In 2D cross-sectional views, ultrasound depicted anatomy, including the cornea, eye lid, and iris, and PA signals were observed at the iris (A). Three-dimensional US/PA volumetric images depicted inconsistent PA signal at the iris and a potential source of imaging artifacts resulting from PA signals from black hair, which can inaccurately extend onto the eye (B). US/PA images may be improved by developing focused light-delivery systems. Scale bar = 3 mm.

In a proof-of-concept study using *ex vivo* porcine eyes, an early-stage focused light delivery system was implemented. An external 300 μm diameter optical fiber was coupled to a traditional ultrasound transducer, i.e. the transducer had no built-in optical fibers for PA imaging (Figure 21). The external optical fiber was positioned for transscleral light

delivery, and PA signals were isolated to the angle (Figure 21B), unlike images acquired with the Vevo LAZR (Figure 21C). Furthermore, the ability to easily implement transscleral light delivery, which is challenging with purely optical techniques like OCT, highlighted another benefit of PA imaging. Transscleral light delivery eliminates concerns of unintentional retinal irradiation and simplifies light delivery as sophisticated optical components are not required to direct light at the angle.

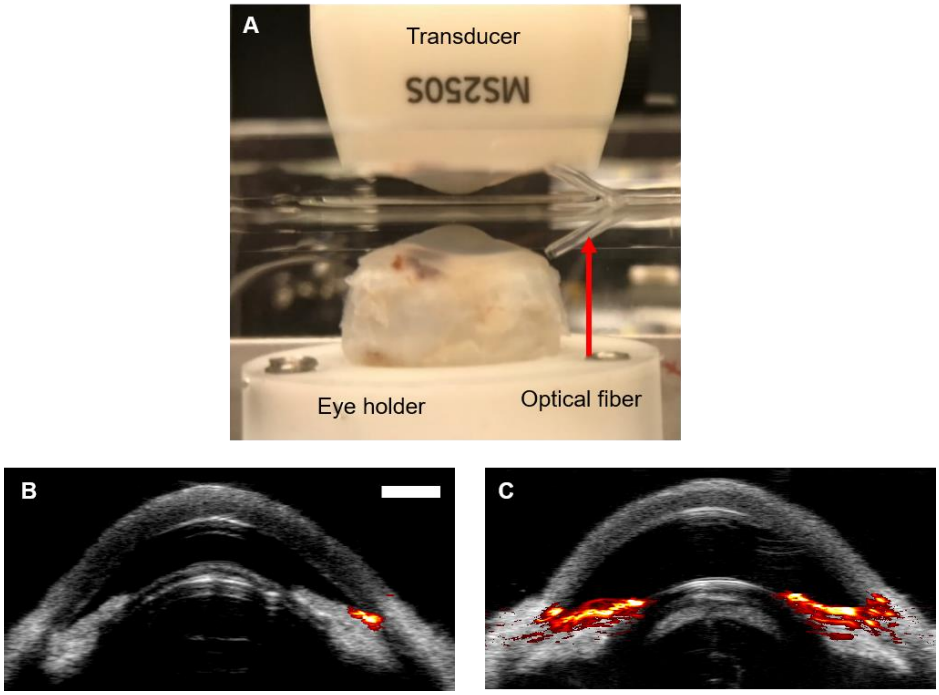

Figure 21. Demonstration of focused light delivery in a porcine eye *ex vivo*. Photograph of the imaging set up (A). An enucleated porcine eye was secured in a holder and submerged in PBS. A 20 MHz ultrasound only transducer was positioned above the cornea on-axis. Light was focused by positioning an external optical fiber for transscleral light delivery to the angle. Combined ultrasound (grayscale) and PA (color scale) images were acquired using the focused light delivery system (B) or the Vevo LAZR (C), which irradiates the entire anterior segment. Focused light delivery only produced PA signals at the region of interest - the angle and TM (B). Scale bar = 3 mm.

To address the issue of poor delivery efficiency, we are currently developing PBNCs with combined magnetic and optical properties [168]. Magnetic properties allow

PBNC-labeled stem cells to be pulled to a tissue target, such as the TM [126]. Optical properties allow detection of PBNC-labeled stem cells with PA imaging. Thus, PBNC-labeled stem cells may allow image-guided magnetic delivery in the future. Figure 22 shows initial characterization of PBNCs and verifies stem cell labeling. Further details on PBNC characterization are described in Chapter 4.

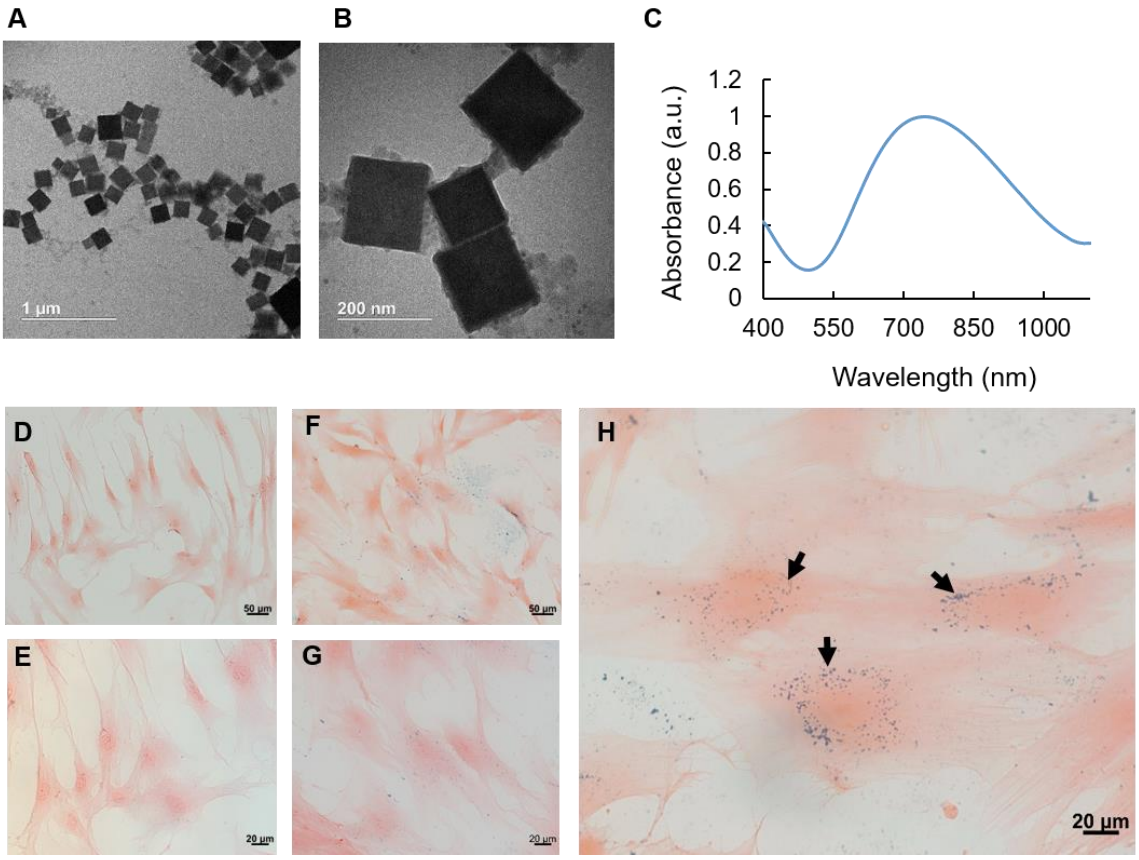

Figure 22. Characterization of photomagnetic PBNCs and labeled stem cells. (A, B) TEM of PBNCs with an edge length of ~200 nm. (C) Absorption spectrum of PBNCs, measured by UV-Vis spectrophotometry, with a peak at 734 nm wavelength. Histology of eosin-stained adipose-derived MSCs confirmed successful cell labeling with PBNCs (D-H). Naïve MSCs at 20x (D) and 40x (E) magnification. MSCs incubated with PBNCs at 1 OD at 20x (F) and 40x (G) magnification. MSCs incubated with PBNCs at 2 OD at 40x magnification (H). PBNCs are blue in color, indicated by black arrows. Proceeding studies were conducted with PBNCs at a concentration of 2 OD.

The first set of studies to assess image-guided magnetic delivery of PBNC-labeled stem cells were conducted using the *ex vivo* perfusion set up in porcine eyes. Since results with AuNS-labeled MSCs showed cells primarily fell to the lens, a disc magnet was placed on the cornea to essentially attempt to reverse the problem with PBNC-labeled MSCs (Figure 23). A 250 µl volume of PBNC-labeled stem cells at 1000k cells/µl was injected in the anterior chamber of perfused porcine eyes. The disc magnet was placed on the cornea for 24 hours while fluid in the anterior chamber continually circulated due to natural outflow through the TM. Minimal PA signal was observed at the lens after 24 hours, and PBNC-labeled stem cells were localized to the cornea at the location of the disc magnet.

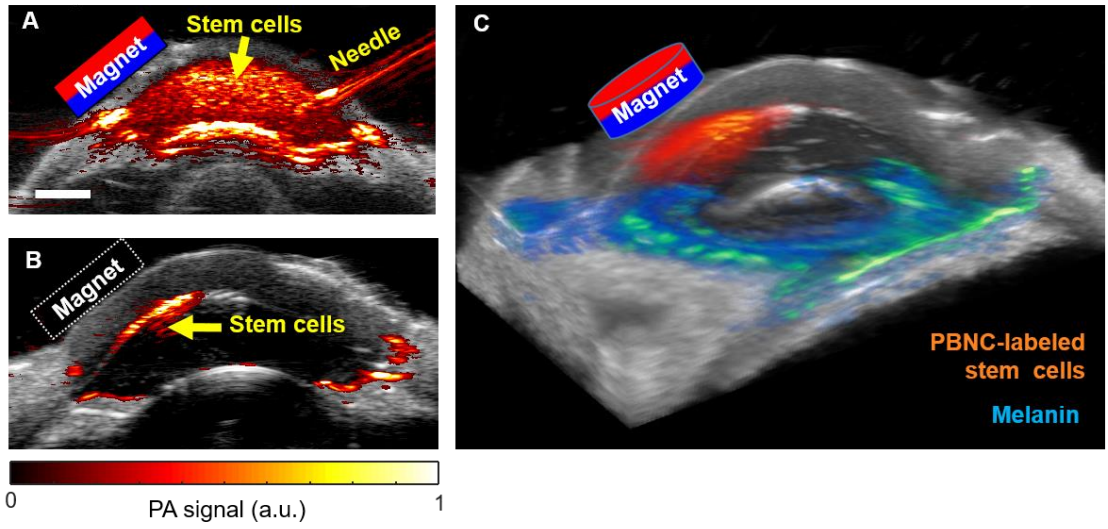

Figure 23. Photoacoustic imaging and magnetic delivery of PBNC-labeled stem cells in perfused porcine eyes *ex vivo*. Two-dimensional ultrasound (grayscale) and PA (color scale) overlay images of PBNC-labeled stem cells in the anterior chamber immediately post-injection (A). After 24 hours of magnet exposure, PBNC-labeled stem cells were pulled to the cornea at the location of the disc magnet (B). (C) Three-dimensional US/PA images confirmed 2D results, indicating initial feasibility of using PBNCs for magnetic guidance and imaging of MSCs. Scale bar = 3 mm.

Next, preliminary *in vivo* studies were conducted in nude rats (n = 2) to assess PBNC-labeled MSC guidance with a ring magnet. Note that these rats had an albino phenotype to focus attention on magnetic delivery and minimize challenges associated with *in vivo* detection and image processing, more specifically due to high background signals, modification of PA spectra from melanin (see Chapter 2), and high sensitivity required to detect a smaller amount of PBNC-labeled stem cells *in vivo* in small animals. Due to lack of melanin, minimal PA signals were observed in 2D and 3D images prior to delivery of PBNC-labeled MSCs (Figure 24A and 24B). A 25 μl volume of PBNC-labeled stem cells at 1000 cells/μl was injected into the anterior chamber of the right rat eye. One rat received no magnet (Figure 24C and 24D). The second rat received a ring magnet placed around the TM (Figure 24 E and 24F). The ring magnet had a power of 9.19 lbs, with a 0.281" thru hole diameter, and was axially polarized. Both animals were imaged after 3 hours. Without the magnet, PBNC-labeled stem cells were primarily localized at the center of the anterior segment and appeared to coat the lens and cornea (Figure 24 C and 24D). With the magnet, PBNC-labeled stem cells were detected closer to the angle, and less PA signal was observed at the center of the eye (Figure 24 E and 24F). Based on anatomy from ultrasound, PA signals located outside of the eye were disregarded (Figure 24C and 24E), i.e it is extremely unlikely that stem cells can accumulate on the surrounding eye lid. These PA signals were inconsistently observed across images and may come from changes in light fluence, transducer height above the eye, and transducer orientation.

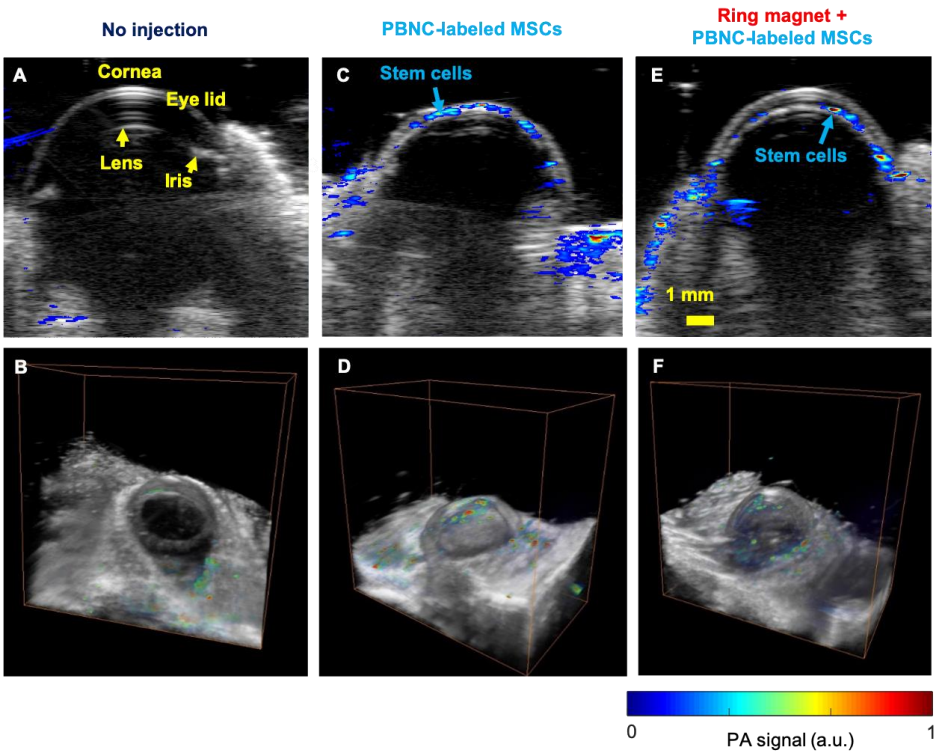

Figure 24. Image-guided magnetic delivery of PBNC-labeled MSCs to the TM *in vivo.* in nude rats. Two- (A, C, E) and three-dimensional (B, D, F) combined ultrasound (grayscale) and PA (color scale) datasets were acquired for eyes that received no injection (A, B); PBNC-labeled MSCs only (C, D); and PBNC-labeled MSCs and a ring magnet (E, F). Minimal background PA signals were observed in control eyes due to lack of melanin (A, B). PA signal from PBNC-labeled MSCs was visible in injected eyes (C - F), and more PBNC-labeled MSCs appeared near the angle after magnet exposure for 3 hours (E, F).

Initial results from *in vivo* magnetic delivery studies appeared promising. In addition, rats that received PBNC-labeled MSCs were observed for changes in ocular morphology indicative of laser damage (Figure 25). Although further assessment is required, no gross changes were observed, which was a positive result considering lack of melanin in albino rats, and thus less ocular protection from light. Together, optical and magnetic properties of PBNCs may facilitate image-guided magnetic stem cell delivery to the TM to improve therapeutic outcomes and clinical utility, adding to the theranostic potential of the US/PA platform in the future.

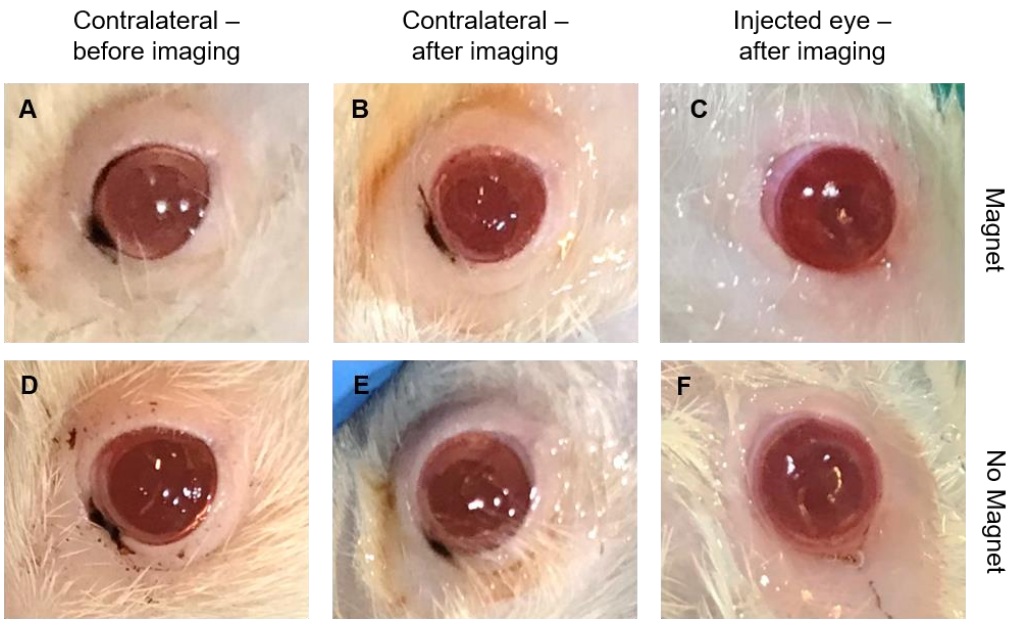

Figure 25. Photographs of eyes after image-guided magnetic delivery of PBNC-labeled MSCs *in vivo*. Top row (A – C): images from the rat that received PBNC-labeled MSCs and a magnet. Bottom row (D - F): images from the rat that received PBNC-labeled MSCs only. In both cases, the contralateral eye received no injection. Contralateral eye before (A, D) and after (B, E) imaging. (C, F) Injected eye after imaging. No gross changes in ocular morphology were observed in eyes that received injections and were imaged.

3.8 Contributions from collaborators

In this chapter, specific contributions were made by Eric Snider, Bailey Hannon, Heechul Yoon, and Andrei Karpiouk For the *ex vivo* porcine experiments using gold nanospheres, Eric Snider maintained and prepared cells, injected cells into porcine eyes, dissected porcine tissue, prepared agarose gels, and imaged with fluorescent microscopy. Bailey Hannon shared her expertise and provided training to execute *in vivo* ocular injections. Heechul Yoon shared gave advice on improving image-processing techniques. Andrei Karpiouk assisted in designing and building the focused-light delivery set up.

CHAPTER 4. TRIMODAL IMAGING TO GUIDE STEM CELL THERAPY OF THE SPINAL CORD USING PRUSSIAN BLUE NANOCUBES

This chapter is adapted from several articles which have been published or accepted for publication, are currently under review, or are in preparation:

Donnelly, E. M.,* Kubelick, K. P.,* Dumani, D. S., & Emelianov, S. Y. (2018). Photoacoustic Image-Guided Delivery of Plasmonic-Nanoparticle-Labeled Mesenchymal Stem Cells to the Spinal Cord. *Nano Letters*, *18*(10), 6625-6632. ***Equal Contribution***

Laffey, M.,* Kubelick, K. P.,* Donnelly, E. M., & Emelianov S. (2019). Effects of freezing on mesenchymal stem cells labeled with gold nanoparticles. *Tissue Engineering Part C: Methods.* **Accepted**. ***Equal Contribution***

Dumani, D. S.,* Cook, J. R.,* Kubelick, K. P.,* Luci, J. J., & Emelianov, S. Y. (2019). Photomagnetic Prussian blue nanocubes: synthesis, characterization, and biomedical applications. *Nanomedicine*. **Accepted.** ***Equal Contribution***

Kubelick, K.P. & Emelianov, S.Y. (2019). Trimodal imaging to guide stem cell therapy of the spinal cord using Prussian blue nanocubes**. Under review.**

Kubelick, K.P. & Emelianov, S.Y. (2020). *In vivo* intraoperative guidance of stem cell delivery in the spinal cord using photoacoustic imaging augmented with Prussian blue nanocubes. **In preparation**.

Kubelick, K.P. & Emelianov, S.Y. (2020). *In vivo* longitudinal monitoring of stem cell therapy in the spinal cord using a trimodal imaging tool. **In preparation.**

4.1 Abstract

Translation of stem cell therapies to treat injuries and diseases of the spinal cord is hindered by lack of real-time monitoring techniques to guide regenerative therapies intra- and post-operatively. Thus, we developed a trimodal ultrasound (US), photoacoustic (PA),

and magnetic resonance (MR) imaging approach augmented with Prussian blue nanocubes (PBNCs) to guide stem cell injections intraoperatively and monitor therapies in the spinal cord post-operatively. Per the clinical procedure, a laminectomy was performed in rats. For intraoperative guidance, PBNC-labeled stem cells were injected directly into the spinal cord while US/PA images were acquired. For post-operative guidance, US/PA/MR images were acquired up to 14 days after surgery. Several features of the trimodal imaging approach were demonstrated including detection of low stem cell concentrations, real-time needle guidance and feedback on stem cell delivery, and agreement between US/PA/MRI. These benefits span intra- and post-operative environments to support further development of this trimodal imaging tool. Although the ability to monitor stem cell location can provide useful information on stem cell migration in the spinal cord, this research is ultimately a building block on the road to functional monitoring *in vivo*. To this end, the focus of future work is development of a photoacoustic probe for stem cell apoptosis detection *in vivo*.

4.2 Introduction

Regenerative medicine holds great promise to offer novel treatment methods for injuries and neurodegenerative diseases of the spinal cord that otherwise have no cure. Stem cell therapy has received substantial interest, but has not yet reached its clinical potential.[43,169–173] Development and translation of stem cell therapies for the spinal cord is hindered by lack of: 1) real-time guidance of stem cell injection; 2) noninvasive, longitudinal monitoring techniques to assess treatment progression and improve understanding of stem cell behavior; and 3) functional stem cell monitoring.[2,43,174,175]

Development of imaging tools to guide and detect stem cells in the spinal cord would expedite therapy development and clinical translation.

Others have recognized this need and substantial effort has been spent developing magnetic resonance imaging (MRI) tools to detect stem cells in the spinal cord.[5,176–179] MRI is the gold standard for central nervous system imaging. Advantages include noninvasive, longitudinal, high-resolution, whole body imaging. Although MRI is an excellent option for post-operative monitoring, challenges exist for intraoperative imaging, including high cost, slow acquisition, large foot print and lack of portability, and incompatibility with tools and instruments in the operating room (OR).[180–182] For these reasons, the use of MRI to guide stem cell therapies throughout the entire course of treatment is challenging. Other modalities can address this need, such as combined ultrasound/photoacoustic (US/PA) imaging.[2,17,90,138,183–185]

Ultrasound signals are produced by backscattering of acoustic waves to convey anatomical information at high resolution. However, contrast is poor due to similar backscattering properties across many tissues. Photoacoustic imaging can address this challenge. In PA imaging, contrast is based on absorption of light rather than scattering of sound. By irradiating an optical absorber with a pulsed laser, thermal deposition and compression of the surrounding tissue produces transient acoustic waves that can be detected by a traditional ultrasound transducer.[115–117,184] Advantages of PA imaging include high contrast, high resolution, real-time imaging, and a variety of exogenous contrast agents exist to obtain cellular information. Furthermore, US/PA imaging systems are portable to facilitate intra- or post-operative imaging.

We previously explored the use of US/PA imaging augmented with gold nanospheres (AuNSs) to provide real-time guidance of stem cell therapies in the spinal cord.[174] Although results showed some intraoperative benefits, applicability to the post-operative environment was not demonstrated. In the current work, a trimodal US/PA/MR imaging approach was introduced to facilitate intra- and post-operative guidance in the spinal cord by labeling stem cells with Prussian blue nanocubes (PBNCs). PBNCs are a unique nanoconstruct that simultaneously possess optical and magnetic properties to produce PA and MR contrast.[148] By labeling stem cells with PBNCs, US/PA imaging can facilitate intraoperative imaging, and MRI can facilitate post-operative imaging per the current clinical standard. This work demonstrated several features of the US/PA/MR imaging approach, including detection of stem cells at low concentrations, real-time needle guidance and injection monitoring, feedback on stem cell delivery, and strong agreement between PA/MR images, to lay the groundwork for a clinical multi-modal imaging protocol.

4.3 Materials and methods

4.3.1 Materials

Dextran-coated superparamagnetic iron oxide nanoparticles (SPIONs), 5 nm and 10 nm diameter, were purchased from Ocean NanoTech (San Diego, CA). Small SPIONs (3 nm diameter) were synthesized in-house. Prior to use, all glassware and stir bars were washed with aqua regia (3:1 HCl:HNO_3; Sigma-Aldrich). All chemicals were used as received.

Adipose-derived mesenchymal stem cells (MSCs) were cultured following methods described above in Chapter 3 (see Section 3.3.1).

4.3.2 Synthesis of small SPION precursors and PBNCs

A 1,000 ml three-neck round bottom flask containing an egg-shaped stir bar was suspended in a silicon oil bath placed on a heated stir plate. One neck was used as a gas inlet, and the second neck was connected to a condenser to keep the reaction under reflux. A 200 ml volume of triethylene glycol (TEG) was added to the round bottom flask, followed by 12.714 g of iron(III) acetylacetonate. The iron was dissolved, and the solution was heated to 140 ˚C for one hour while stirring under argon or nitrogen gas. Next, an additional 200 ml of TEG was added to the flask to remove any iron deposited on the sides of the glassware. The solution was then heated to 200 ˚C. After 2 hours the solution turned from a reddish color to a dark brown-black color indicating the formation of Fe_3O_4 nanoparticles, commonly referred to as SPIONs. The SPION solution was cooled to room temperature while continuing to stir under argon or nitrogen gas overnight. The volumes and masses of reagents were carefully measured throughout the synthesis to keep track of Fe concentrations. The SPION solution was diluted 10x with deionized ultra-filtered (DIUF) water containing dextran at a concentration of 10 mg dextran/mg of Fe. The reaction was gently stirred overnight to allow the dextran to coat the SPIONs. Excess dextran was removed from the solution by centrifugation in 50 kDa filtered centrifuge tubes (Amicon).

Synthesis of PBNCs using iron oxide precursors was described in Chapter 3, and the same method was used here (see Section 3.3.14).

4.3.3 Characterization of nanoparticles

Transmission electron microscopy (TEM) (Hitachi HT7700 TEM, IEN/IMAT Materials Characterization Facility, Georgia Institute of Technology) was used to characterize PBNC morphology. Carbon formvar TEM grids (Electron Microscopy Sciences) were prepared by drop casting 3 μl of particle solution and drying overnight at room temperature. Images were acquired at an accelerating voltage of 100 – 120 kV. PBNC edge length and SPION diameter were determined using ImageJ (NIH).

The optical absorption spectra of 20 nm, 40 nm, and 200 nm PBNCs was measured using UV-Vis spectrophotometry (Synergy HT microplate reader, BioTek Instruments). Readings were taken in 5 nm increments from 400 nm to 995 nm.

Magnetic properties of PBNCs were first assessed using superconducting quantum interference device (SQUID) magnetometry. Prior to measurements, samples were concentrated by centrifugation using 50 kDA filtered centrifuge tubes (Amicon). The final concentrations were 8.7 mg/ml for PBNCs (20 nm edge length), and 20 mg/ml for SPIONs (3 nm diameter). Each sample was scanned separately. Briefly, 100 μl of the concentrated nanoparticle solution was added to a polycarbonate capsule (AGC3, Quantum Design). The capsule was sealed with non-magnetic tape and inserted in a non-magnetic straw to be held inside the magnetometer. A capsule filled with DIUF water was used to confirm no significant background magnetization. The temperature was set to 5 K, and the magnetic field was varied from 5 T to −5 T twice to obtain a hysteresis curve of the magnetic moment.

Longitudinal and transverse relaxivity of all PBNCs (20 nm, 40 nm, and 200 nm edge length) were determined using a low-field 0.5T NMR spectrometer (Maran Ultra 23, Resonance). Solutions at concentrations ranging from 533 to 16 µg of Fe/ml were prepared. The average relaxation time was calculated using four scans per sample.

Further characterization of PBNCs was conducted using tissue-mimicking phantom experiments. All particle phantom experiments were conducted following methods described above in Chapter 3 (see Section 3.3.6). PBNCs (20 nm, 40 nm, and 200 nm edge length) were all at a concentration of 2 optical density (OD) in inclusions.

4.3.4 Imaging Equipment

All US/PA imaging experiments were conducted using the Vevo LAZR and 20 MHz transducer. The imaging system was described in detail above (see Section 3.3.5).

A 7T preclinical MRI system (Bruker PharmaScan) was used to acquire all MR images. Samples were secured in a cylindrical holder and inserted in a 38 mm imaging coil for phantom studies. *In vivo* studies were conducted using a 60 mm imaging coil. Built-in pulse sequences were used with slight modifications to the repetition (TR) and echo times (TE), described in detail below for each experiment, to improve nanoparticle contrast. MR images were post-processed using the built-in Bruker Pharmascan image analysis software.

4.3.5 In vitro studies of PBNC-labeled stem cells

Stem cells were labeled with 200 nm PBNCs using the same incubation method described in Chapter 3 (see Section 3.3.3). In this case, stem cells were labeled with 200 nm PBNCs at a concentration of 2 OD.

Histology was used to verify PBNC uptake. Microscopy coverslips were cleaned using 70% ethanol. Once dried, each coverslip was placed in a well of a 6-well cell culture plate. A monolayer of MSCs was grown on top of the coverslips. MSCs were labeled with PBNCs (see Section 3.3.3). PBNC-labeled MSCs were fixed onto the coverslips, stained with eosin for 15 minutes (VWR; see Section 4.3.10), and mounted onto slides for brightfield microscopy.

Tissue-mimicking gelatin phantom experiments were conducted to assess PA and MR detection sensitivity of PBNC-labeled MSCs at known concentrations. Phantom experiments of PBNC-labeled MSCs were conducted following the same phantom recipe described above (see Section 3.3.6). In this case, each dome-shaped inclusion contained PBNC-labeled MSCs at 10k, 5k, 2.5k, 1.25k, 625, 313, 156, 78, 39, 20, and 0 cells/μl. The same exact phantom was imaged using US/PA and MRI. Cross-sectional US/PA images of the cell inclusions were acquired at 740 nm wavelength, corresponding to the optical absorption peak of PBNCs, determined by UV-Vis spectrophotometry. The average PA signal of the inclusion, manually isolated using ultrasound, was calculated over 20 frames to accommodate fluctuations in laser energy. MR images were acquired using a multi-slice multi-echo (MSME) pulse sequence to determine T2 relaxation times starting with TR = 1955.2 ms and TE = 20 ms. TE increased by 20 ms increments for 32 steps. Coronal views

were acquired and analyzed due to better visualization of inclusions. Although different slice orientations were used for PA and MRI, PBNC-labeled MSCs appeared homogenously distributed throughout inclusions in either case. Thus, slice orientation should not impact results. For MR image analysis, the built-in Bruker Pharmascan software was used to define a circular region of interest corresponding to the inclusion. The average T2 relaxation time and standard deviation was calculated using the built-in parametric fit algorithm.

4.3.6 Ex vivo spinal cord access and stem cell injection protocol

All studies involving animals were conducted following guidelines of the Institutional Animal Care and Use Committee (IACUC) of the Georgia Institute of Technology. Spinal cord procedures followed previously reported methods.[137,173,186,187] In brief, Sprague-Dawley rats (Charles River Laboratories) were sacrificed, and the spinal column was removed. A multilevel laminectomy was performed to expose the underlying spinal cord. Up to 5 μl of PBNC-labeled MSCs suspended at 10k cells/μl were directly injected into the spinal cord per the clinical procedure at a rate of 16 nL/sec using a 33G syringe attached to an ultra-micropump (World Precision Instruments).[44]

4.3.7 Ex vivo intraoperative US/PA image-guidance

During needle insertion, single-wavelength US/PA datasets were acquired at 740 nm wavelength and exported to MATLAB for post-processing. Reverberation artifacts extending below the needle shaft were removed by creating a mask with a width of 2x the outer diameter of the 33G needle used for the injection and aligning the mask with the length of the needle shaft. Small gaps in the PA signal were occasionally observed along

the needle shaft. The MATLAB image processing toolbox and morphological operators, specifically image dilation followed by erosion, were used to connect gaps and display a continuous needle shaft.

During stem cell injections, single-wavelength US/PA datasets were similarly acquired at 740 nm wavelength and exported to MATLAB for post-processing. PA signals from the needle shaft and PBNC-labeled MSCs were segmented to better visualize the injection. To segment images, US/PA images were split into two regions of interest: 1) the region containing the needle, and 2) the region containing the stem cells. In the needle shaft region of interest, reverberations artifacts were removed as described above. In the stem cell region of interest, a threshold was applied to reduce background noise. Any remaining pixels in the stem cell region of interest were identified as PBNC-labeled MSCs and were multiplied by a scaling factor. As a result, PBNC-labeled MSCs were primarily colored red, and the needle shaft was primarily colored blue. The average PA signal was calculated for the region containing the PBNC-labeled stem cells.

4.3.8 Ex vivo trimodal US/PA/MR imaging

Locations of PBNC-labeled MSC injections were marked by glass capillary tubes, which were visible in ultrasound and MRI, inserted in the surrounding muscle, to assure the same injections were compared across modalities. US/PA datasets were acquired with and without a layer of muscle covering the spinal cord. MR images were only acquired with a layer of muscle placed on top of the spinal cord.

Three-dimensional (3D) US/PA datasets were created by attaching the transducer to a translational motor and compiling two-dimensional (2D) cross-sectional views

acquired at 133 μm steps and 740 nm wavelength. Datasets were then exported to MATLAB for post-processing. Anatomical information provided by ultrasound was used to spatially distinguish PA signals from different species: 1) blood vessels/background signals that appeared on top of the spinal cord; 2) PBNC-labeled stem cells that appeared within the spinal cord. PA signals from each species were further segmented by thresholding and scaling such that background signals were primarily colored blue and PBNC-labeled MSCs were primarily colored red. Reverberation artifacts were occasionally observed below strong PA signals from blood vessels at the surface of the spinal cord. These artifacts were removed by finding the local maximum PA signal, which corresponded to the vessel, and eliminating PA signals below a 0.5 mm vessel radius. Sagittal US/PA images were produced by integrating 3D datasets along the x-dimension, i.e. image width, and interpolating to display resulting images with square pixels (~40 μm x ~40 μm).

MR images were acquired using several different pulse sequences. T2-weighted images were produced using the T2-Turbo RARE pulse sequence with TR = 2500 ms and TE = 35 ms. T2*-weighted images were produced using the T1-FLASH sequence with TR = 310 ms and TE = 5 ms for axial images or TE = 10 ms for sagittal images. Four averages were acquired for all pulse sequences.

Following US/PA/MR imaging, spinal cord tissue was fixed in 10% neutral buffered formalin, followed by submersion in sucrose for one week. Tissue was frozen in embedding medium for histology and sectioned into 20 μm sagittal slices. Sections were stained by submersion in eosin for 75 seconds. Brightfield photomicrographs were

acquired using the Axio Observer microscope (Zeiss). Wide-field views were produced by compiling tile scans.

4.3.9 In vivo surgical procedure and imaging protocols

All studies involving animals were conducted following IACUC guidelines per the Georgia Institute of Technology.

First, the procedure room was prepared. During room preparation, the PBNC-labeled stem cells were prepared by a second person (see Section 3.3.3). Three tables were cleaned with 70% ethanol or Sporcidin disinfectant solution (Contec Healthcare). While still in the packaging, a surgical gown, surgical gloves, hair net, face mask, sterile hand towel, and scrub brush were placed directly onto Table 1, which was non-sterile. The two remaining tables were covered with sterile drapes. Table 2 was used to display all sterile surgical tools: small/medium/large scissors, small animal bone cutters, two glass syringes equipped with a 33G needle, needle grabbers, two forceps with teeth, retractor, curette, spatula, and Vannas scissors (World Precision Instruments). Sterile Q-tips, sterile sutures (5-0 vicryl, undyed, braided, reverse cutting), and fenestrated drapes were also placed on Table 2. Table 3 was used as the surgical table and contained the disinfected stereotax, heating pad, transducer holder, and ultra-microinjection pump (World Precision Instruments).

After the room was prepared, rats were anesthetized using either isoflurane or injectable anesthetics. For isoflurane, anesthesia was induced with 5% isoflurane at 500 ml/min and maintained with 1.0% - 2.5% isoflurane at the same flow rate. For injectables, anesthesia was induced using a combination of dexdomitor (.5 mg/kg) and ketamine (75

mg/kg). However, only half of the recommended dose was required to maintain a surgical plane for approximately 3 hours, which was enough time to complete the procedure. Once anesthetized, an intramuscular or subcutaneous injection of sustained release buprenorphine (.6 - .8 mg/kg) was administered for pain relief. The rat was then prepared for surgery by removing hair on the back between the shoulder blades and hips. The exposed skin was sterilized by wiping the area with poviodine iodine swab sticks (Dynarex) followed by alcohol wipes (BD) for two cycles. On the third cycle, the iodine was left on the skin to maintain sterility. A hard toe pinch, i.e. nail on bone, confirmed the surgical plane was reached. At this point, surgical garb was donned.

A lumbar laminectomy was performed to expose the spinal cord. An incision of approximately 2 cm was made in the skin along the spine. A fenestrated drape was adhered to the skin with the incision centered in the drape hole. The skin was held open with retractors or sutures. Two cuts were made in the muscle on either side of the spinous process, and the muscle was removed with blunt dissection until the spinous processes and laminae were fully exposed and clear of muscle. Finally, the bone was removed to expose the spinal cord for direct injection. Up to 5 μl of PBNC-labeled MSCs suspended at 10k cells/μl were directly injected into the spinal cord per the clinical procedure at a rate of 16 nL/sec using a 33G syringe attached to an ultra-micropump (World Precision Instruments).[44] The needle remained in the spinal cord for 5 minutes after injection to prevent reflux. After injection, the muscle was sutured back over the spinal cord, then the skin was sutured back over the muscle. The bone was not replaced.

For *in vivo* intraoperative studies, two strains of rats were used: Sprague-Dawley (Charles River Laboratories; n = 4) and nude rats (n = 2; Taconic) for a total of 6 rats. All rats were female. US/PA datasets were acquired intraoperatively with the Vevo LAZR during surgery following the imaging protocol described above in *ex vivo* studies (see Section 4.3.7). Figure 26 depicts the surgical and intraoperative imaging set up. After 24 hours, MR images were acquired to validate US/PA results using the 7T preclinical MRI system (Bruker PharmaScan) and the T2-RARE sequence described in *ex vivo* studies (see Section 4.3.8). Rats were then sacrificed, and the spinal cord was harvested for histology. US/PA datasets were exported to MATLAB for post-processing. MR datasets were processed using the built-in Bruker Pharmascan software.

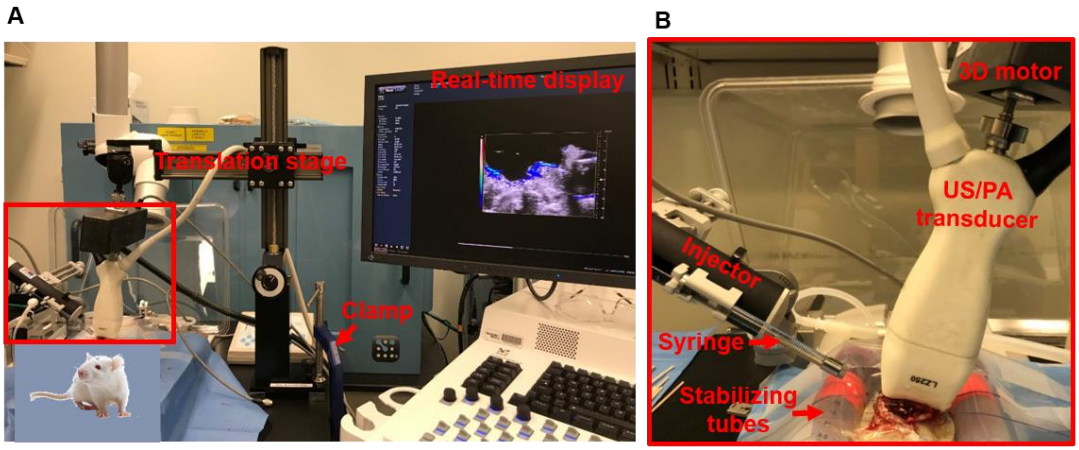

Figure 26. Surgical and imaging set up for *in vivo* intraoperative studies. The combined US/PA imaging transducer was positioned on top of the exposed cord while the needle was brought into position (A, B). US/PA images were acquired as the needle was inserted, during, and immediately post-injection after needle removal. Zoomed in photograph depicting the position of the transducer and syringe (B).

For longitudinal studies, nude rats (Taconic; n = 5) were imaged 3, 5, 7, 10, and 14 days post-injection with US/PA imaging and MRI. All rats were female. The albino phenotype was preferred, but some black and white spotted nude rats were also used. For

the spotted rats, a black patch was frequently observed on the spine. In this case, the pigmented skin was moved outside the field of view during US/PA imaging. For longitudinal imaging, the Vevo system was operated with an external laser (Phocus Mobile, Opotek) because higher laser energy was achievable to penetrate overlying muscle and skin post-operatively. Otherwise US/PA and MR datasets were acquired using the same imaging protocol as in *ex vivo* studies (see Section 4.3.7 and 4.3.8) and *in vivo* intraoperative studies. US/PA datasets were exported to MATLAB for post-processing. MR datasets were processed using the built-in Bruker Pharmascan software. After 14 days, animals were sacrificed, and the spinal cord was harvested for histology.

4.3.10 Histological analysis of PBNC-labeled stem cells

Spinal cord sections were stained with eosin (VWR) or DAPI (Thermo Fisher). In both cases, slides were removed from the -80˚C freezer and air dried at room temperature for 30 minutes.

For eosin staining, slides were submerged in PBS for 1 x 10 minutes, followed by 1 x 1 minute in 95% EtOH, 75 seconds in diluted eosin (4:1 Eosin: 95% EtOH), 1 x 1 minute in 95% EtOH, 2 x 1 minute in 100% EtOH, and 1 x 10 minutes in xylene. Slides were mounted and dried in the fume hood for at least 24 hours. Brightfield images were acquired (Axio Observer, Zeiss).

For DAPI staining, slides were rehydrated with PBS for 20 minutes. A 1:1000 dilution of DAPI was prepared in PBS per the manufacturer's instructions. Slides were stained with DAPI for 10 minutes in the dark at room temperature, followed by 3 x 5 minute

washes with PBS. Slides were mounted and dried overnight at room temperature in the dark. Confocal fluorescent microscopy images were acquired (LSM 700, Zeiss)

4.3.11 Ex vivo porcine studies

A porcine spine was obtained from the slaughterhouse (Holifield Farms, Covington, GA). Muscle was removed and a laminectomy was performed per the clinical procedure.[44] A hand saw and bolt cutters were used to cut the thick porcine bones. A 31G insulin syringe (BD) was used to inject 25 μl of highly concentrated 200 nm PBNCs (50 OD). Multi-wavelength US/PA datasets were acquired in this intraoperative mimicking situation using the 15 MHz and 20 MHz transducer. Each transducer was coupled directly to the exposed spinal cord using ultrasound gel. Data acquired using the 20 MHz transducer was further processed in MATLAB. Anatomical information from ultrasound was used to identify the region of interest corresponding to the spinal cord, and background PA signals in surrounding tissue were suppressed. Three-dimensional volumetric images were created in AMIRA.

4.3.12 Stem cell viability probe

A caspase-3 sensitive photoacoustic imaging probe was synthesized to assess MSC apoptosis.[188] The probe consisted of three components: (1) a hydrophilic DEVD peptide sequence (aspartate-glutamate-valine-asparate; Asp-Glu-Val-Asp); (2) an aggregating and quenching (AgQ) unit consisting of 2-cyano-6-aminobenzothiazole (CABT; Sigma-Aldrich); and (3) a commercially-available fluorescent dye absorbing at 800 nm wavelength (IRDye 800 CW NHS ester; LI-COR Biotechnology). The DEVD peptide motif is synthesized using well-established Fmoc chemistry methods.[189] Briefly, after

synthesizing Fmoc-Lys(alkyne)-COOH (Sigma-Aldrich) and coupling to each amino acid in the sequence, the Fmoc group is deprotected using piperidine/DMF (VWR) to connect the DEVD peptide sequence. The overall chemical structure of the imaging probe is depicted in Figure 27.

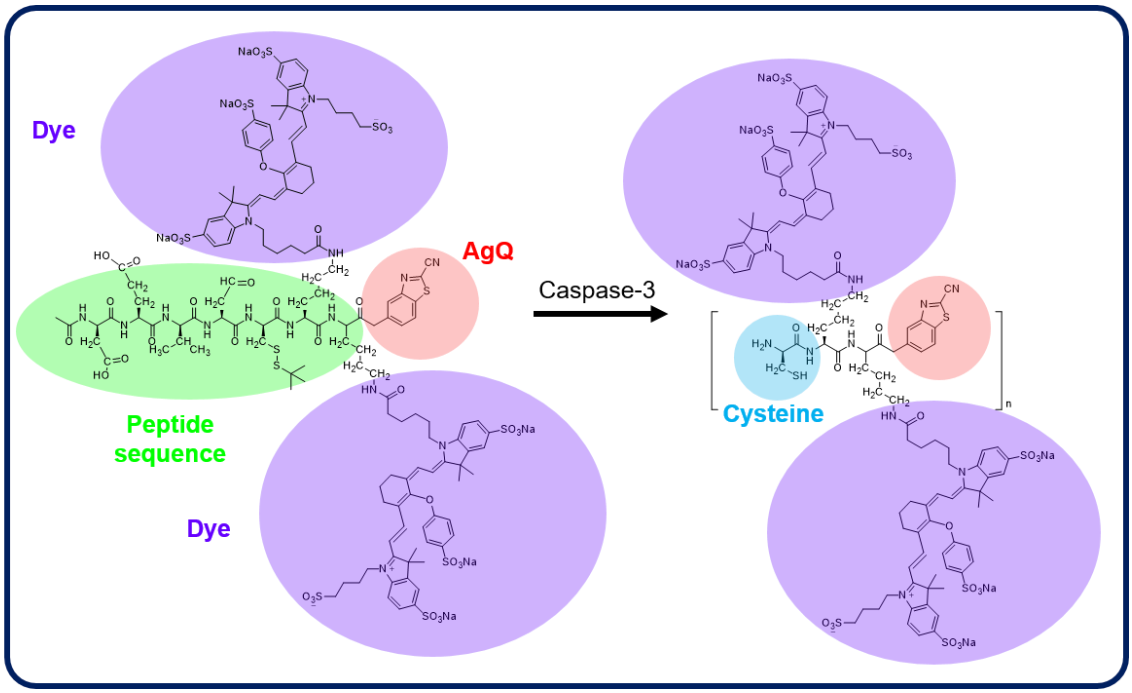

Figure 27 Chemical structure photoacoustic imaging probe for sensing apoptosis. The probe consisted of an aggregating/quenching unit (AgQ; red circle), IR800 dye (purple circles), and peptide sequence (green circle). Cleavage of the DEVD peptide by caspase-3 upon apoptosis induces aggregation of the probe through a condensation reaction that takes place between CABT (red circle) and the thiol and amino groups of cysteine (blue circle). As a result of aggregation, fluorescent signal is quenched and PA signal is enhanced. Thus, enhanced PA signal corresponds to cell death.

4.4 Results

4.4.1 Characterization of PBNCs

To demonstrate size control of the PBNC synthesis method, 3, 5, or 10 nm diameter SPIONs were used as the iron source to produce PBNCs with different edge lengths. TEM

images confirmed that PBNC size varied with SPION precursor size (Figure 28). Small PBNCs with ~20 nm edge length resulted from 3 nm diameter SPION precursors (Figure 28A and 28D). Medium PBNCs with ~40 nm edge length resulted from 5 nm diameter SPION precursors (Figure 28B and 28E). Large PBNCs with ~ 200 nm edge length resulted from 10 nm SPION precursors (Figure 28C and 28F). The plot summarizes the distribution of resulting PBNC edge length and SPION precursor diameter (Figure 28G).

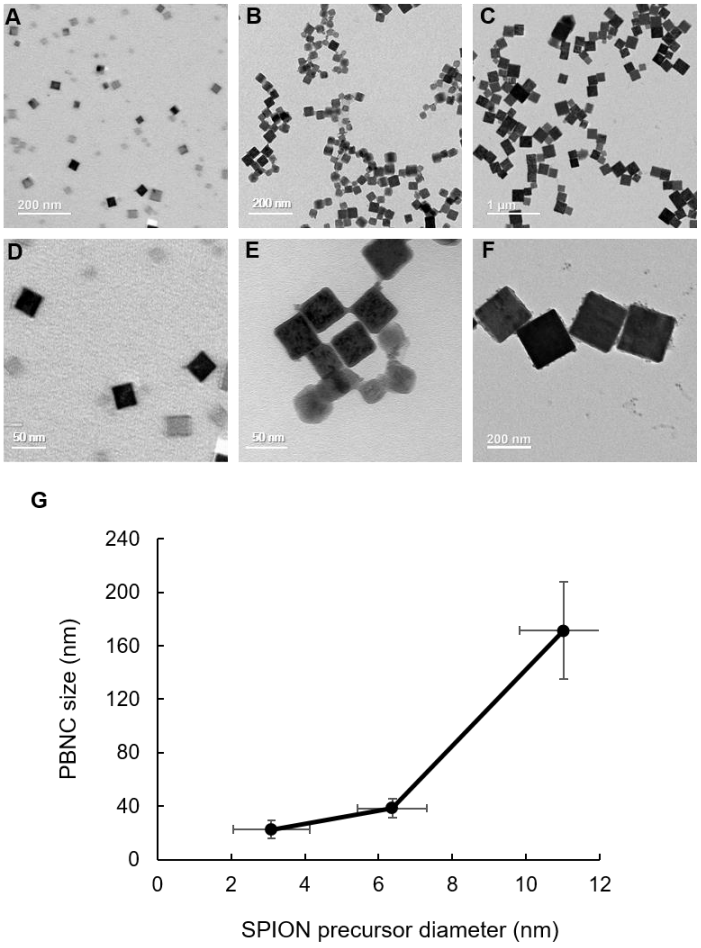

Figure 28. Characterization of size-controlled PBNCs synthesized from SPION precursors. TEM images of PBNCs. PBNCs with an edge length of (A) ~20 nm, (B) ~40 nm, and (C) ~200 nm synthesized from 3 nm, 5 nm, and 10 nm diameter SPIONs, respectively. (D – F) Images at increased magnification for 20 nm, 40 nm, and 200 nm PBNCs, respectively. (G) Scatter plot showing relationship between SPION diameter and resulting PBNC size.

Optical and magnetic properties of PBNCs were assessed with UV-Vis spectrophotometry and SQUID, respectively. The optical absorption spectrum of the 20 nm, 40 nm, and 200 nm PBNCs were comparable, and each particle had a peak optical absorption at 685 nm, 720 nm, and 740 nm wavelength, respectively (Figure 29A). Spectral shifts likely resulted from increased optical scattering of larger PBNCs. The magnetism of small 20 nm PBNCs and their 3 nm SPION precursors was analyzed with SQUID (Figure 29B). PBNCs exhibited superparamagnetic behavior and had a magnetic saturation of 104.0 emu/g. SPIONs had a magnetic saturation of 20.5 emu/g. This corresponded to a 5-fold increase in magnetization. Overall, UV-Vis and SQUID measurements supported further assessment of PBNCs as MR and PA contrast agents.

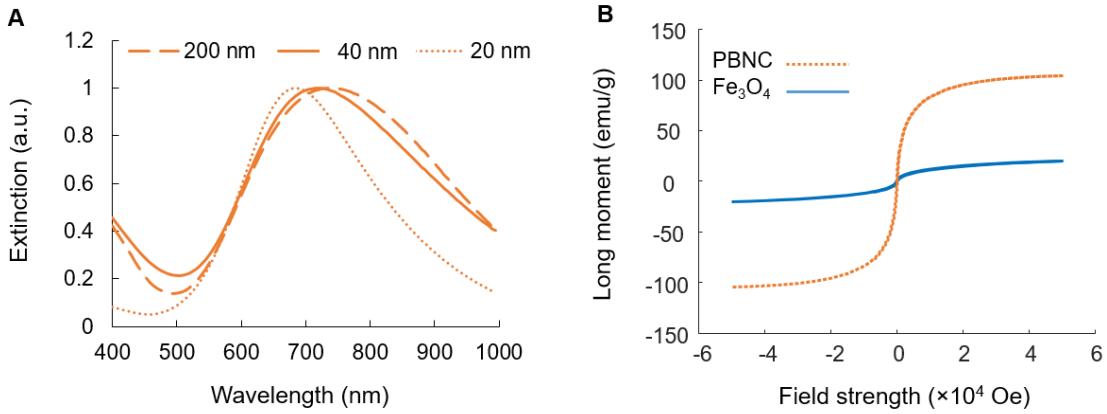

Figure 29. Magnetic and optical properties of PBNCs. (A) UV-Vis spectrophotometry shows the peak absorption for the 20 nm, 40 nm, and 200 nm PBNCs, with a peak at 685 nm, 720 nm, and 740 nm respectively. (B) Magnetic moment curves show a 5-fold increase in magnetization for 20 nm PBNCs compared to the 3 nm SPIONs based on nanoparticle mass. Results confirmed photomagnetic properties of PBNCs.

To test feasibility of our PBNCs as MRI contrast agents, relaxometry studies were performed using a 0.5 T NMR spectrometer. To calculate the molecular weights, Fe_3O_4 and $C_{18}Fe_7N_{18}$ were assumed for SPIONs and PBNCs, respectively. The measured

transverse relaxivity values are found in Table 2. Transverse relaxivity was 1.11 $mM^{-1}s^{-1}$ for 3 nm SPIONs. After synthesis, 20 nm PBNCs had a 10.05 $mM^{-1}s^{-1}$ transverse relaxivity, showing a 9-fold increase over the 3 nm SPION precursor. However, the size-matched 20 nm SPIONs had a transverse relaxivity of 920 $mM^{-1}s^{-1}$. Thus, for the same particle size, SPIONs still provided better relaxivity than their PBNC counterparts. The large 200 nm PBNCs had a transverse relaxivity of 402.4 $mM^{-1}s^{-1}$, a 40-fold increase over the smaller 20 nm PBNCs, showing the scalable magnetic properties with increasing PBNC size. The r_2/r_1 ratio, an indicator for effective T_2 contrast agents, ranged from 1.02 to 16.43 for 20 nm to 200 nm PBNCs at 0.5 T.

Table 2. Relaxometry measurements of PBNCs and SPIONs

Magnetic field	Nanoparticle size & type	Transverse relaxivity r^2 [$mM^{-1}s^{-1}$]
0.5 T	2-nm SPION	1.11
0.5 T	10-nm SPION	316.0
0.5 T	20-nm SPION	920.8
0.5 T	20-nm PBNC	10.05
0.5 T	40-nm PBNC	34.0
0.5 T	200-nm PBNC	402.4

To assess the feasibility of PBNCs as multi-modal contrast agents, nanoparticles were imaged in a tissue-mimicking phantom. Dome-shaped inclusions contained PBNCs with 20 nm, 40 nm, or 200 nm edge length at 2 OD. In the phantom, PBNCs of all sizes generated high contrast under T_2-weighted MRI (Figure 30B–D). US/PA imaging at 740

nm laser light irradiation confirmed PA contrast (Figure 30J–L). Additionally, the PA spectra matched the expected absorption based on UV-Vis measurements (Figure 30M).

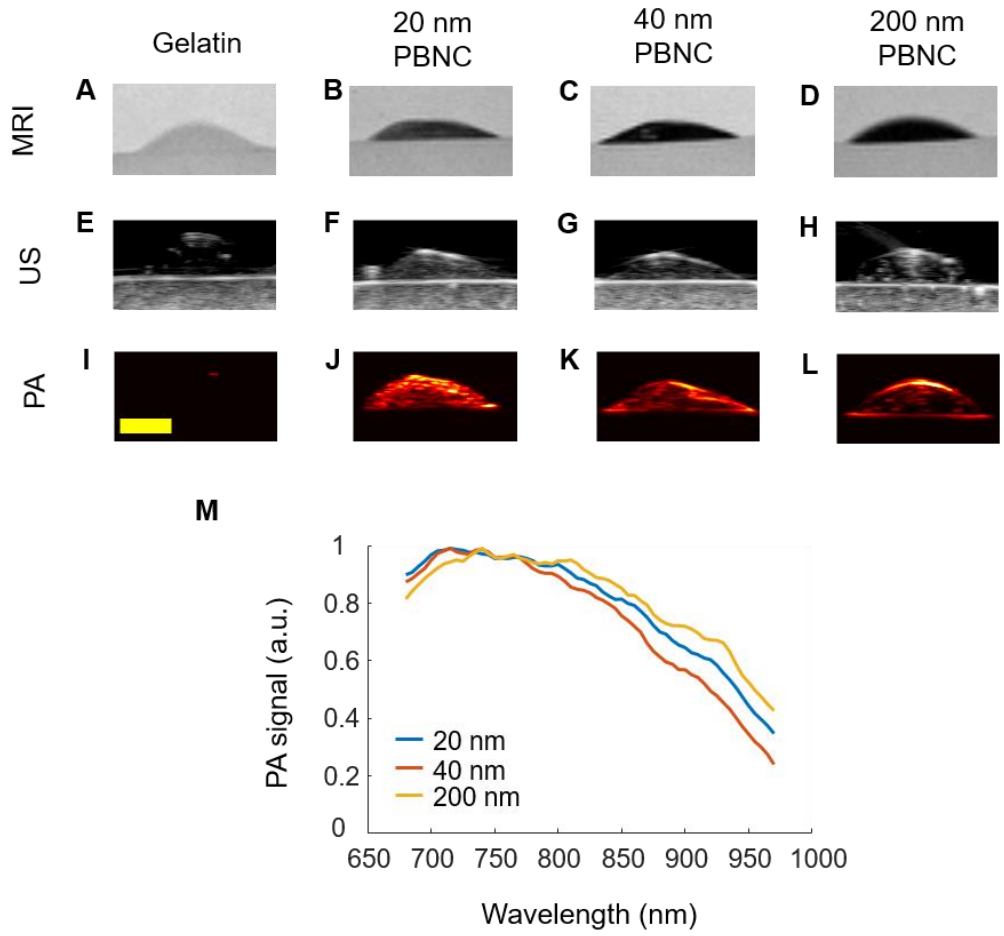

Figure 30. Trimodal US/PA/MRI of PBNCs in a tissue-mimicking phantom. All PBNCs were suspended at the same concentration based on optical density (OD = 2). The phantom contained four dome-shaped inclusions. One contained gelatin only, and the other three contained different types of PBNCs. The same inclusion was imaged with all modalities: top row (A – D) T2-weighted MR images; middle row (E – H) US images; bottom row (I – L) PA images at 740 nm wavelength. Columns (left to right): gelatin control, 20 nm, 40 nm, or 200 nm PBNCs. All PBNCs produced MR (B – D) and PA (J – K) contrast. Plot of PA spectra for all PBNC types (M).

4.4.2 Characterization of PBNC-labeled stem cells in vitro

Tissue-mimicking phantom experiments were repeated with PBNC-labeled MSCs. MSCs were incubated with PBNCs at 1 OD. Each dome-shaped gelatin inclusion contained PBNC-labeled MSCs at known cell concentrations. US/PA and MR images were acquired to compare detection sensitivity (Figure 31 and Figure 32). First, the representative PA spectrum of PBNC-labeled MSCs (Figure 31B) was similar to UV-Vis spectrophotometry results of PBNCs alone (Figure 29). Qualitatively, ultrasound signal (top row; grayscale) and PA signal (bottom row; color scale) both decreased with decreasing cell concentration (Figure 31C). The average PA signal was calculated for each inclusion and confirmed PA signal decreased with cell concentration (Figure 31D). Together, the US/PA images and average PA signal indicated a detection limit below ~100 cells/μl.

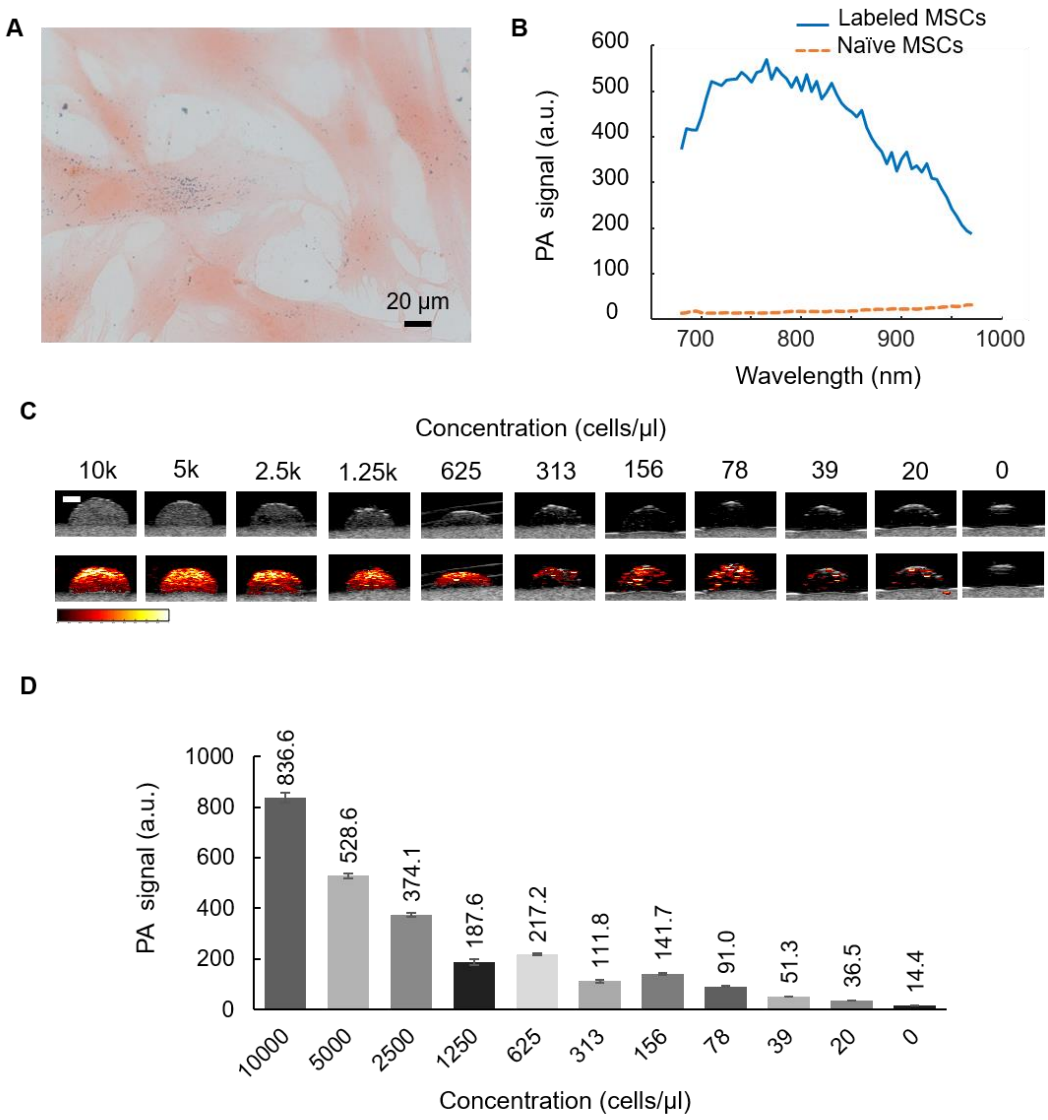

Figure 31. PA signal of PBNC-labeled MSCs *in vitro*. (A) Brightfield microscopy of eosin-stained cells verified successful labeling based on blue pigment, indicative of PBNCs, colocalized with pink cytoplasm. (B) Representative PA spectrum of PBNC-labeled MSCs at 5k cells/μl. (C) Images of all dome inclusions. Top row: ultrasound (grayscale) only. Bottom row: US/PA (color scale) overlays. (D) Bar graph of comparing PA signal with cell concentration. Scale bar = 2 mm.

Next, MR images were acquired for the same tissue-mimicking phantom to confirm PBNC-labeled MSCs produced MR contrast and compare detection limits of PA versus MRI. The average T2 relaxation time at 7T was determined using the MSME sequence

and parametric fit function. Relaxation time increased as PBNC-labeled MSC concentration decreased (Figure 32A). PBNC-labeled MSCs at concentrations above ~300 cells/µl had faster T2 relaxation times than the 0 cell/µl control at 354.5 ms and 368.6 ms, respectively. However, qualitative differences were visible between the 78 cells/µl inclusion and 0 cells/µl inclusion (Figure 32B). Overall the *in vitro* study indicated PA imaging was more sensitive to lower cell concentrations than MRI, but results will vary *in vivo* and both modalities successfully detected PBNC-labeled MSCs.

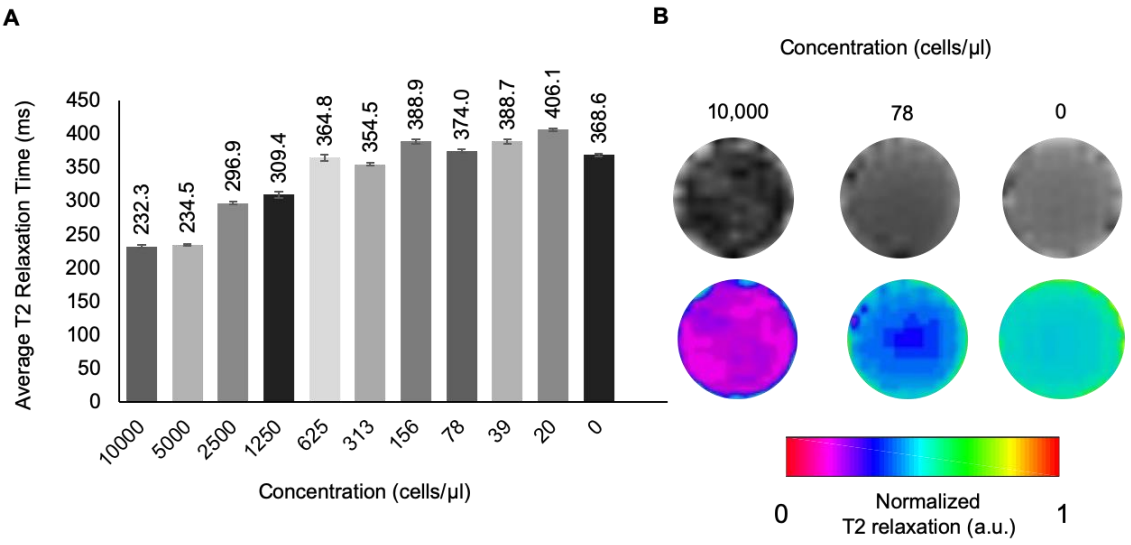

Figure 32. MRI of stem cells labeled with PBNCs *in vitro*. MRI studies were conducted with the same phantom used in the PA studies. Coronal images were acquired using a MSME sequence to determine average T2 relaxation times (A). T2 relaxation time increased with decreasing cell concentration. Representative T2-weighted MR images (B; top row) and parametric fit images depicting relaxation time (B; bottom row).

4.4.3 Intraoperative studies, ex vivo and in vivo

Feasibility of US/PA imaging as an intraoperative tool to guide needle insertion and injection of PBNC-labeled MSCs was first assessed *ex vivo* in Sprague-Dawley rats (Figure 33). After performing a multilevel laminectomy, US/PA images were acquired in

real-time as the needle was advanced into the spinal cord. Ultrasound (grayscale) imaging provided anatomical context for needle placement (Figure 33A–D). Although the 33G needle shaft was difficult to detect with ultrasound at 20 MHz (Figure 33A–D), it was easily visualized with PA imaging (color scale) (Figure 33E–H).

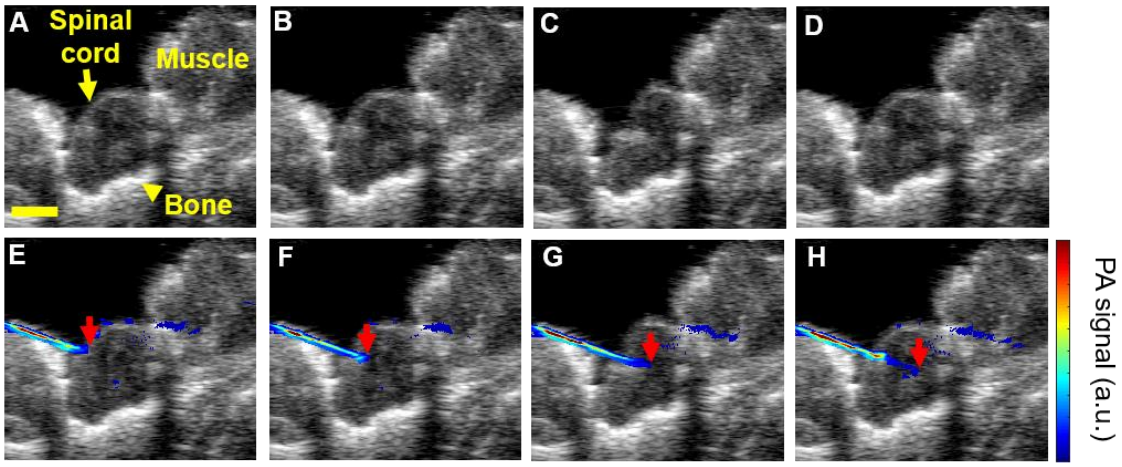

Figure 33. US/PA image guidance of real-time needle insertion in a rat spinal cord *ex vivo*. Top row: ultrasound (grayscale) only. Bottom row: combined ultrasound (grayscale) and photoacoustic (color scale) images at 740 nm wavelength. Red arrows indicate the 33G needle tip. Scale bar = 2 mm.

Real-time US/PA images were acquired throughout a 4 µl injection of PBNC-labeled MSCs (Figure 34) *ex vivo*. PA images were post-processed so that the needle shaft primarily appeared blue and PBNC-labeled MSCs primarily appeared red. PBNC-labeled MSCs suspended at 10k cells/µl, a clinically relevant cell concentration, were detected after only 1 µl was injected (Figure 34B). The average PA signal increased as a function of injection volume (Figure 34E). Results provided proof-of-concept that PA imaging augmented with PBNCs can provide real-time feedback on MSC delivery success, which is based on injection location, volume delivered, and stem cell retention in the spinal cord.

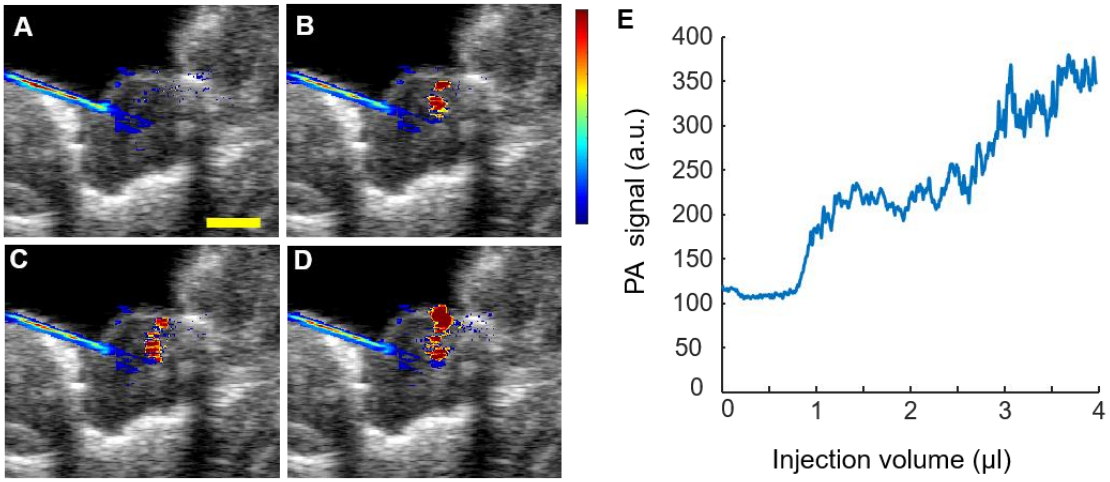

Figure 34. Injection of PBNC-labeled MSCs in a rat spinal cord *ex vivo*. Throughout the injection, combined ultrasound (grayscale) and photoacoustic (color scale) images were acquired using a 20 MHz transducer and a laser operating at 740 nm wavelength. (A – D) US/PA images at 0, 1, 2, and 4 µl injected, respectively, at a concentration of 10k cells/µl. (E) Plot comparing PA signal with injection volume. Scale bar = 2 mm.

Thus far, optical properties of PBNCs were utilized to implement PA imaging in the spinal cord. However, PBNCs also possess magnetic properties, and the imaging approach can extend to post-operative MRI. The spinal cord was injected at two locations in the spinal cord *ex vivo* with ~2 µl or 5 µl of PBNC-labeled MSCs suspended at 10k cells/ µl. First, US/PA images were acquired and post-processed to distinguish PA signals from the background and PBNC-labeled MSCs (Figure 35A–C). Next, a layer of muscle was placed on top of the spinal cord to mimic the transition from intraoperative to post-operative imaging and MR images were acquired. PBNC-labeled MSCs showed negative contrast in T2-weighted (Figure 35D–F) and T2*-weighted (Figure 35G–I) MR images. Both the ~2 µl (Figure 35B–H) and 5 µl (Figure 35C–I) injections were observed at similar locations in the US/PA and MR images.

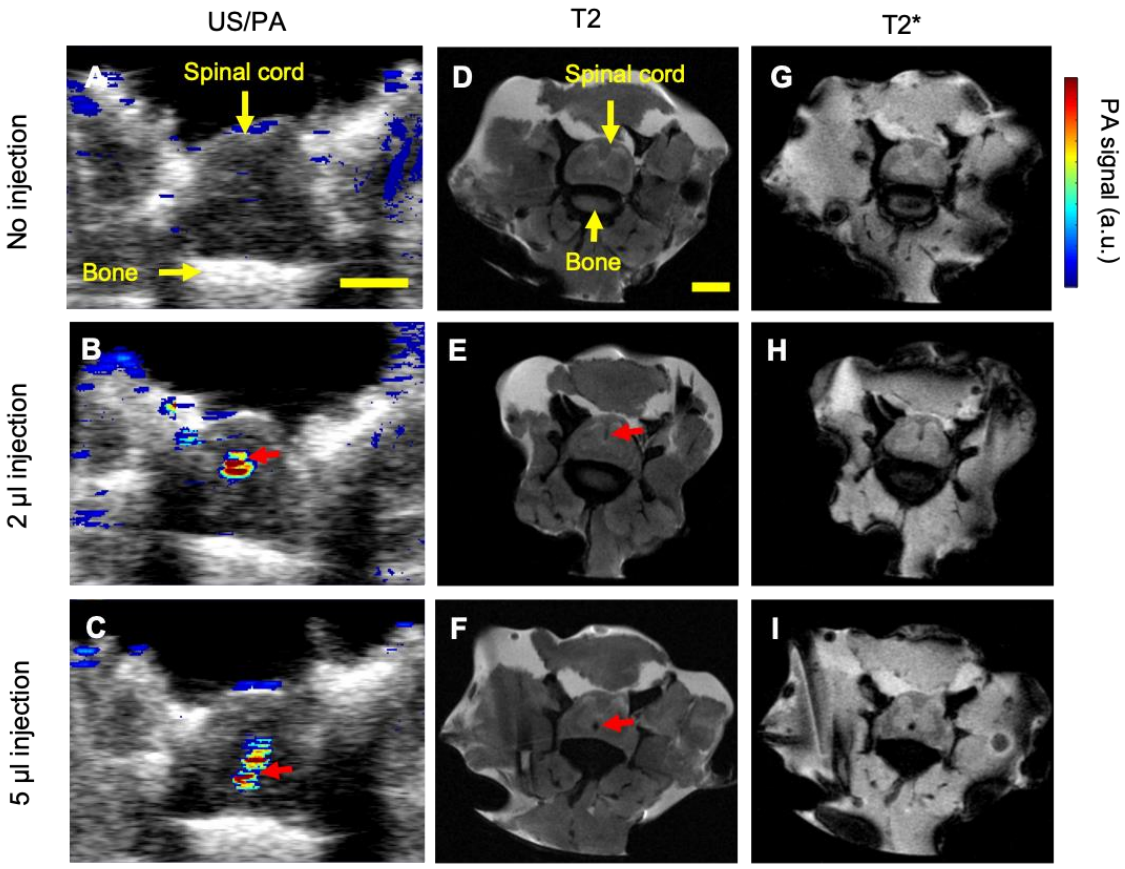

Figure 35. Multi-modal detection of PBNC-labeled stem cells. PBNC-labeled MSCs were suspended at 10k cells/µl. Top row: control, no cells injected. Middle row: 2 µl injection of PBNC-labeled stem cells. Bottom row: 5 µl injection of PBNC-labeled stem cells. PA images (A - C) were acquired at 740 nm wavelength. Muscle was placed over the cord prior to MR imaging to mimic the clinical procedure and the post-operative imaging scenario. MR images were acquired using T2 (D - F) and T2* (G - I) pulse sequences. Red arrows indicate location of stem cells. Scale bar = 2 mm.

Sagittal US/PA/MR images of the spinal cord were also created (Figure 36). In this orientation ~2 µl and 5 µl injections of PBNC-labeled MSCs were visible in the same frame to allow further comparison of US/PA and MR detection of PBNC-labeled MSCs. Additionally, US/PA images were displayed without (Figure 36A) and with (Figure 36B) a layer of muscle on top of the spinal cord to mimic intraoperative and post-operative scenarios, respectively, and evaluate the feasibility of extending US/PA imaging to post-

operative monitoring. Both PBNC-labeled MSC injections were detected with PA imaging in either case. T2*-weighted MR images confirmed PA results, and both stem cell injections were detected at similar locations (Figure 36C). Brightfield photomicrographs further confirmed injection locations for PA/MRI (Figure 36D, E) and verified MSCs were still labeled with PBNCs, indicated by aggregated blue pigment speckles co-localized with pink cytoplasm (Figure 36F).

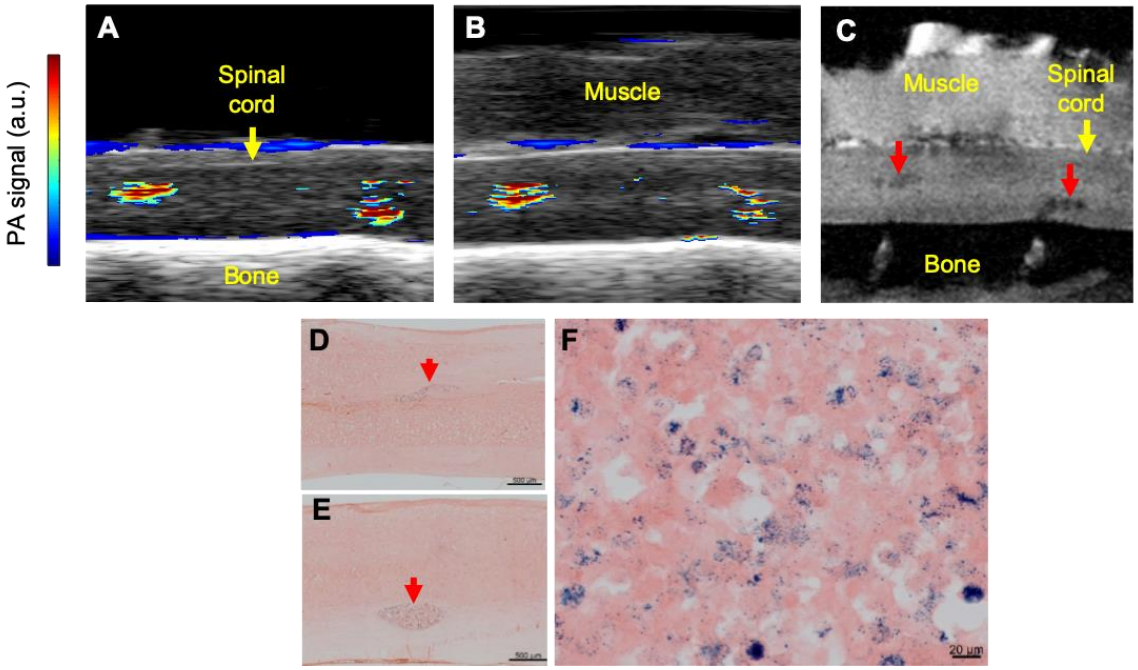

Figure 36. Multi-modal detection of PBNC-labeled MSCs with overlying muscle. PBNC-labeled MSCs (red arrows) at 10k cells/µl were injected twice along the spinal cord. Sagittal US/PA (A, B) and T2* MR images (C) depicted the ~ 2 µl (left) and 5 µl (right) injections of PBNC-labeled MSCs before (A) and after (B, C) a layer of muscle was placed over the spinal cord. Brightfield microscopy of eosin-stained tissue at 10x (D, E) and 40x (F) magnification further verified injection locations (D – F).

Ex vivo studies validated surgical techniques, imaging protocols, and detection algorithms. Agreement between US/PA and MR data sets motivates progression to *in vivo* studies. The first set of *in vivo* studies similarly assessed the ability to guide needle

insertion (Figure 37), visualize stem cell delivery intraoperatively (Figure 38), and detect PBNC-labeled stem cells post-operatively with MRI 24 hours after surgery (Figure 39). *In vivo* US/PA datasets were acquired during real-time while the needle was inserted into the spinal cord following the methods used in *ex vivo* studies. Ultrasound imaging provided anatomical context, while PA imaging clearly highlighted the needle shaft (Figure 37). Substantial reverberation artifacts from the needle were observed with both modalities. PA artifacts could be removed with post-processing. Real-time *in vivo* US/PA imaging also visualized breathing and resulting motion in the spinal cord. This movement can change the location of the injection target, thus visualization with US/PA imaging during needle insertion can improve accuracy and safety of the procedure.

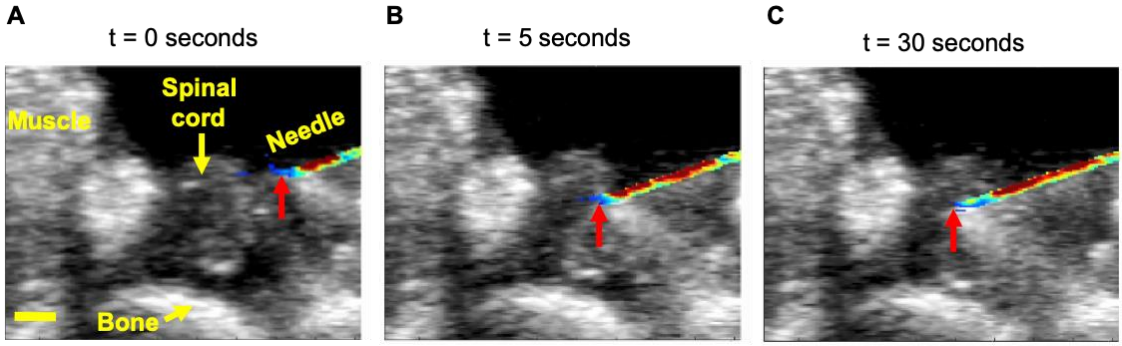

Figure 37. *In vivo* US/PA image-guidance of needle insertion in the rat spinal cord. Combined ultrasound (grayscale) and PA (color scale) images were acquired with a 20 MHz transducer at 740 nm wavelength in real-time. Red arrows indicate the needle tip. Images from t = 0 seconds, 5 seconds, and 30 seconds (A – C), respectively. Scale bar = 3 mm.

After needle insertion, US/PA images were acquired during the stem cell injection *in vivo* (Figure 38). PA signals from the needle and PBNC-labeled MSCs were segmented such that the needle was primarily colored solid red to better distinguish PBNC-labeled MSCs. During the injection, accumulation of the PBNC-labeled stem cells was visible

from 0 to 4 µl (Figure 38A–C). Real-time guidance also highlighted a problem with stem cell delivery in this case, specifically reflux of the injection out of the spinal cord. Stem cell reflux would not have been visible without image guidance. Thus, results can inform researchers or clinicians if another it is worth attempting another risky injection based on stem cell retention at the tissue target.

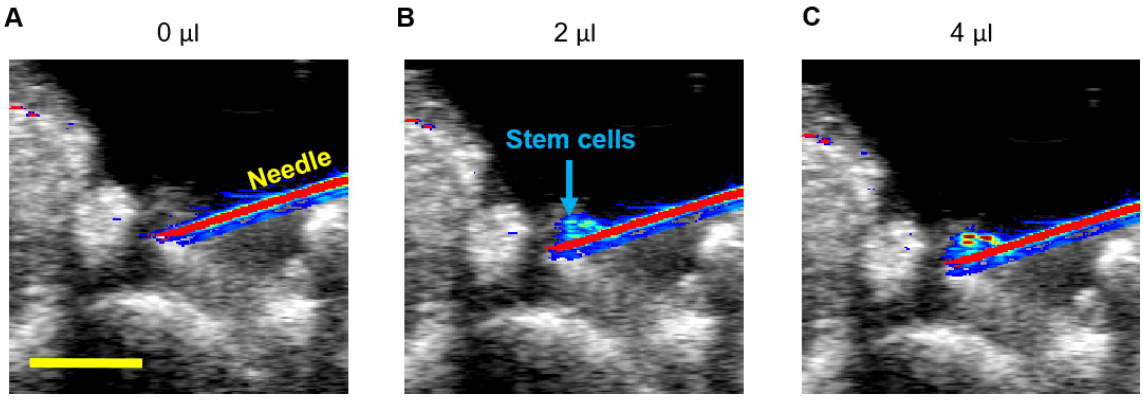

Figure 38. *In vivo* US/PA imaging during PBNC-labeled MSC injection into the rat spinal cord. Combined ultrasound (grayscale) and PA (color scale) images acquired with a 20 MHz transducer at 740 nm wavelength during injection of PBNC-labeled MSCs at 10k cells/µl. Images at t = 0, 2, and 4 µl injected (A – C), respectively. Scale bar = 3 mm.

Once the needle was removed from the spinal cord, a final set of US/PA images were acquired prior to closing the incision for comparison to MR images acquired 24 hours after surgery (Figure 39). Thus, this study mimicked the transition from intraoperative guidance with US/PA imaging to post-operative guidance with MRI, the gold standard for clinical spinal cord imaging. PBNC-labeled stem cell injections were observed at similar locations with a similar footprint in US/PA (Figure 39A) and T2-weighted MR images (Figure 39B). After completing MR data acquisition, rats were sacrificed, and the spinal cord was excised. A photograph of the excised cord showed a superficial blue spot in the center of the spinal cord, indicative of PBNC-labeled MSCs (Figure 39C).

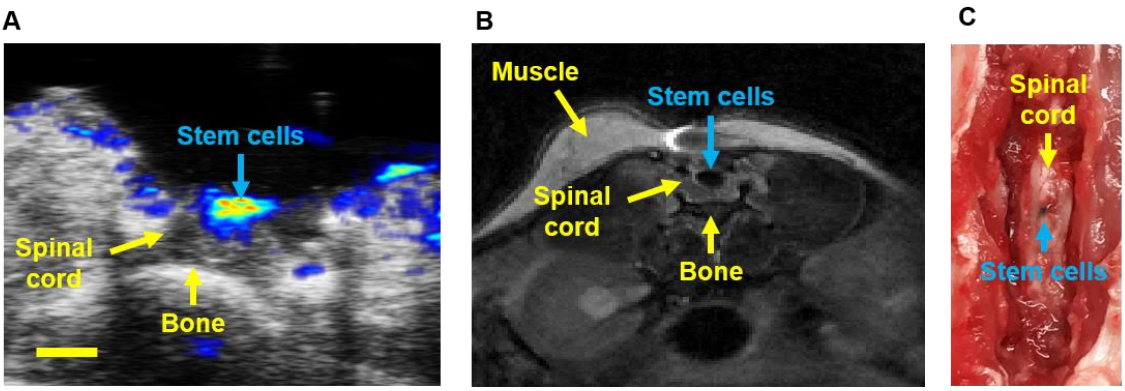

Figure 39. *In vivo* intraoperative US/PA and post-operative MRI. (A) Combined ultrasound (grayscale) and PA (color scale) images were acquired intraoperatively with a 20 MHz transducer at 740 nm wavelength after a 5 µl injection of PBNC-labeled MSCs at 10k cells/µl. Post-operative MR images were acquired 24 hours later (B). Photograph of the excised spinal cord depicting PBNC-labeled MSCs (C). Scale bar = 3 mm.

Histological analysis further verified presence of PBNC-labeled MSCs 24 hours after injection. Blue PBNCs were visible on eosin-stained tissue sections with brightfield microscopy (Figure 40). However, brightfield microscopy only confirmed presence of particles, not stem cells. To confirm the latter, stem cells were double-labeled with a fluorescent dye in addition to PBNCs prior to injection. Thus, green fluorescence confirmed presence of PBNC-labeled stem cells with confocal microscopy.

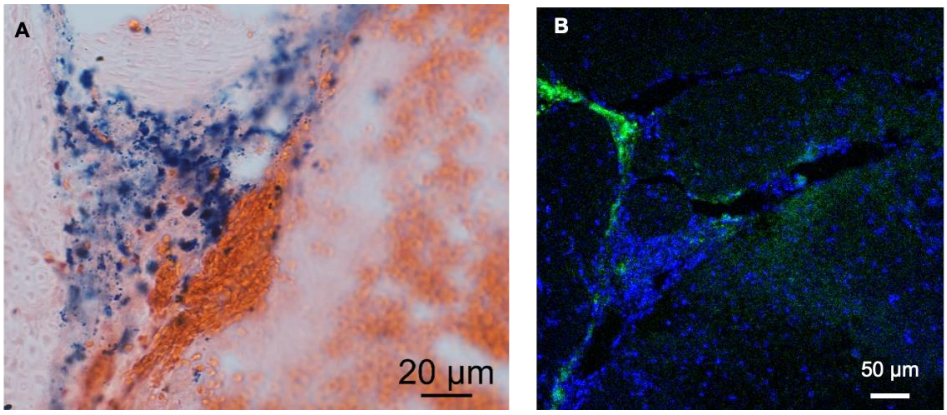

Figure 40. Histology of PBNC-labeled MSCs at 24 hours. Stem cells were double-labeled with PBNCs and a fluorescent dye (CellTracker Green) in culture prior to injection into the spinal cord. (A) Brightfield microscopy of eosin-stained spinal cord and blue PBNCs. (B) Confocal microscopy of DAPI-stained spinal cord and green PBNC-labeled MSCs.

4.4.4 In vivo longitudinal monitoring

The above *in vivo* studies highlighted the feasibility of intraoperative US/PA imaging and post-operative MRI to monitor PBNC-labeled MSCs at a single, early time point. However, information is desired at multiple, later time points to more fully develop the imaging platform. In addition, extending US/PA imaging to post-operative monitoring is of interest to add new opportunities for therapy assessment and provide complimentary information to MRI. According to these goals, more extensive longitudinal monitoring studies were conducted.

For longitudinal *in vivo* studies, PBNC-labeled MSCs (5 µl volume at 10k cells/µl) were similarly injected directly into the spinal cord of immune-compromised rats (n = 5). Multiple sites were injected, space permitting. After stem cell delivery, the muscle and skin were sutured back over the cord, but the bone was not replaced per the clinical procedure. Both US/PA and MR datasets were acquired at multiple time points – at most

3, 5, 7, 10, and 14 days post-injection. In all US/PA datasets below, background PA signals outside of the spinal cord were suppressed using anatomical information from ultrasound.

Figure 41 displays post-operative axial views of a PBNC-labeled MSC injection in the spinal cord at 3, 5, 7, 10 and 14 days *in vivo*. Axial views were first assessed because the orientation was most straightforward for image acquisition, processing, and visualizing injections. PA signals from PBNC-labeled stem cells were visible at all time points (Figure 41A–E). The T2-weighted MR image at Day 14 confirmed presence of the PBNC-labeled stem cell injection. Overall, results indicated extending US/PA imaging to post-operative stem cell monitoring in small animals seemed feasible.

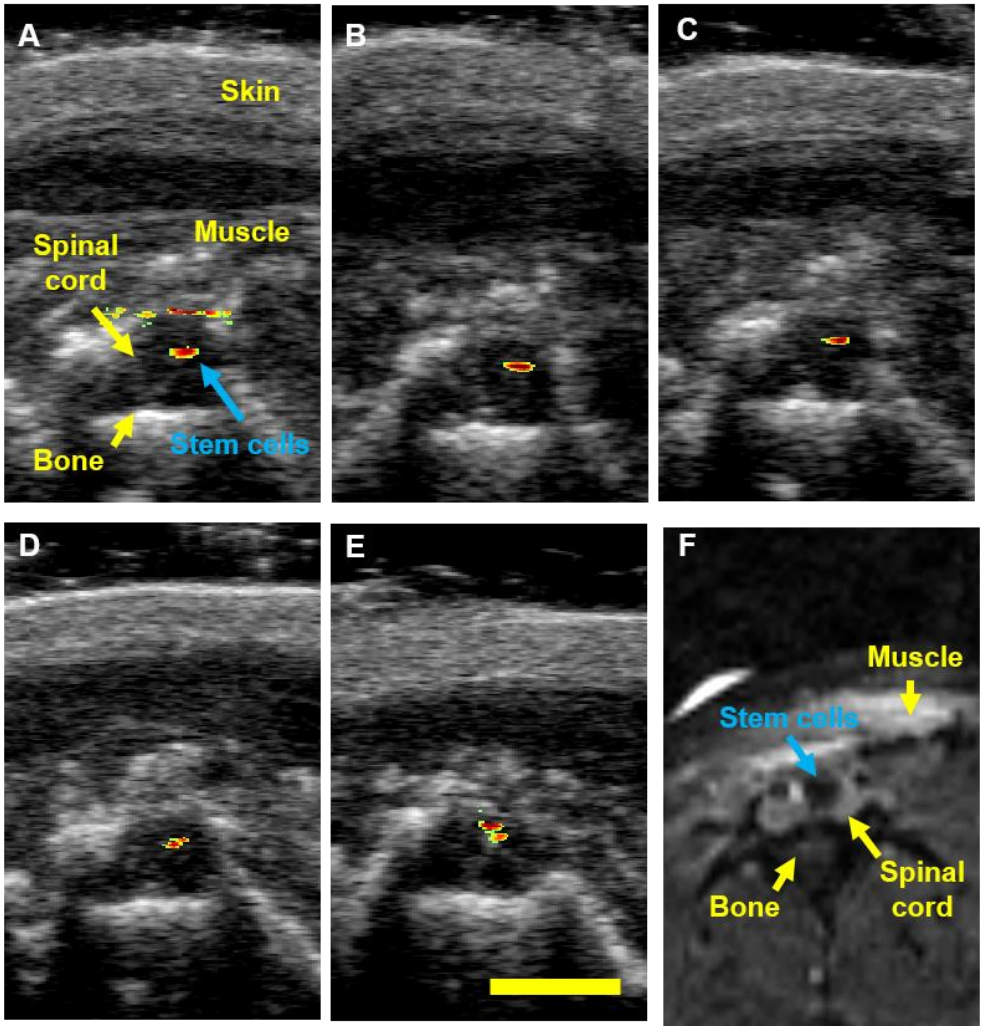

Figure 41. Longitudinal monitoring of PBNC-labeled MSCs *in vivo* – axial views. Post-operative combined ultrasound (grayscale) and PA (color scale) images were acquired using at 20 MHz transducer at 740 nm wavelength at 3, 5, 7, 10, and 14 days, respectively (A – E). PBNC-labeled MSCs were still visible at day 14 with PA imaging (E). T2-weighted MR images confirmed presence of PBNC-labeled MSCs (F). Scale bar = 3 mm.

To further establish a ground truth and compare detection with T2-weighted MRI, sagittal and coronal views were also acquired (Figure 42). Sagittal and coronal orientations allow visualization of multiple injections in the spinal cord, which is common clinical practice.[44] The spinal cord was injected with PBNC-labeled MSCs at three distinct locations. By day 14, sagittal views did not clearly depict injections (Figure 42A–D). However, negative contrast indicative of PBNC-labeled MSCs from all three injections

was more clearly identifiable in coronal views (Figure 42E–H). Coronal views may also better visualize stem cell migration from the injection site.

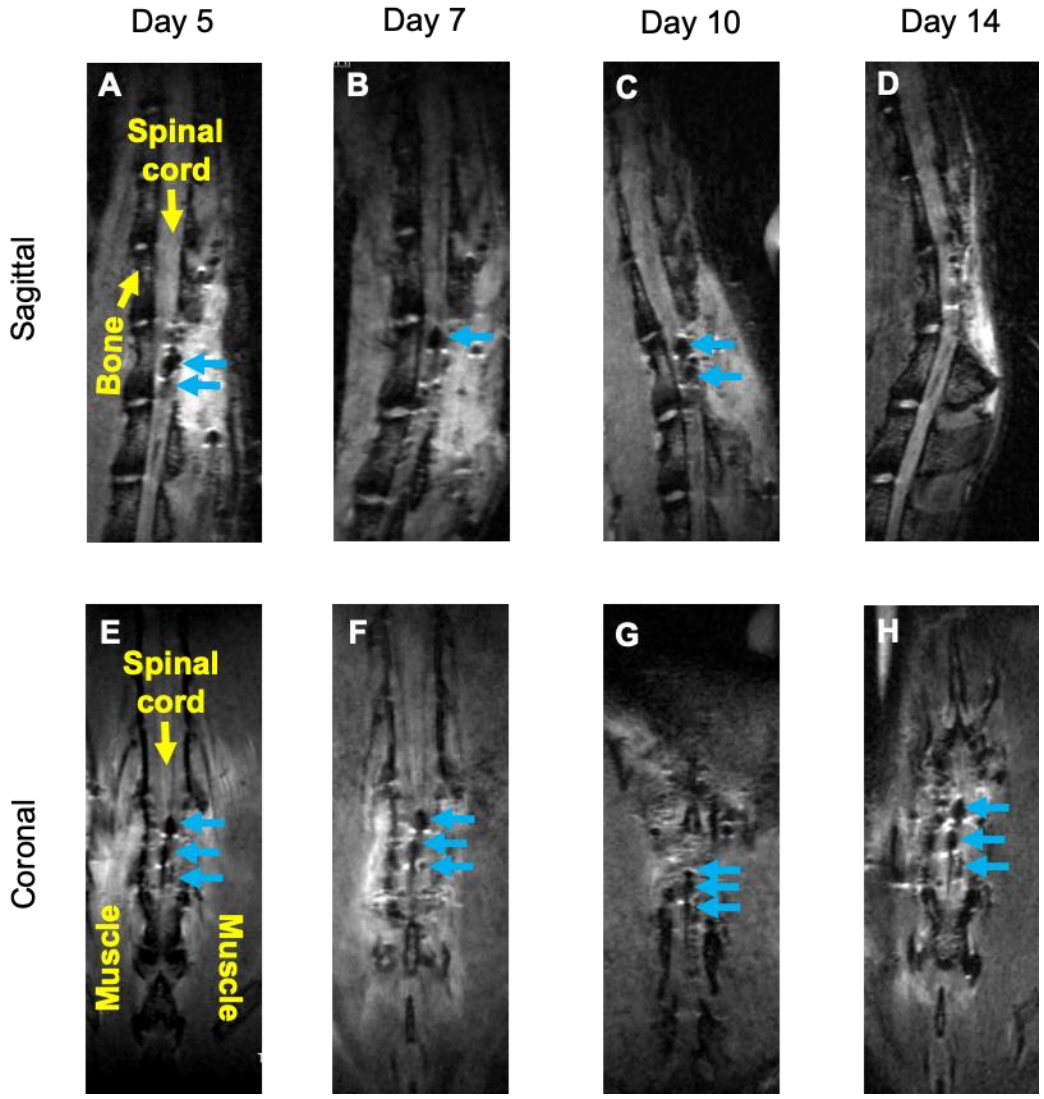

Figure 42. Longitudinal monitoring of PBNC-labeled MSCs MRI *in vivo* – sagittal and coronal views. PBNC-labeled MSCs (5 µl at 10k cells/µl) were injected into the spinal cord at three separate locations. Sagittal (top row; A – D) and coronal (bottom row; E – H) Post-operative T2-weighted MR images at 5 (A, E), 7 (B, F), 10 (C, G), and 14 days (D, H). Blue arrows indicate injections of PBNC-labeled MSCs.

Given better visualization of PBNC-labeled MSC injections in coronal MRI views, three-dimensional US/PA datasets were processed to display images in a similar orientation

(Figure 43). PA datasets were integrated with depth (y-dimension) to create a coronal view of the three PBNC-labeled MSC injections and visualize the injection footprint. The red box indicates the approximate location of the spinal cord. Changes in the injection location and footprint of PBNC-labeled stem cells were observed at each time point. Some imaging artifacts may be present (Figure 43B), and results did not perfectly agree with MRI. However, expecting perfect agreement was unrealistic due to differences in exact spinal column orientation, MR image slice selection, contrast mechanisms of PA and MRI, and detection sensitivity. In spite of this, three injection sites were depicted with both PA and MRI. With further development, PA imaging may ultimately better visualize stem cell migration in the spinal cord in small animals *in vivo* as more subtle variations in the stem cell footprint were observed with PA imaging.

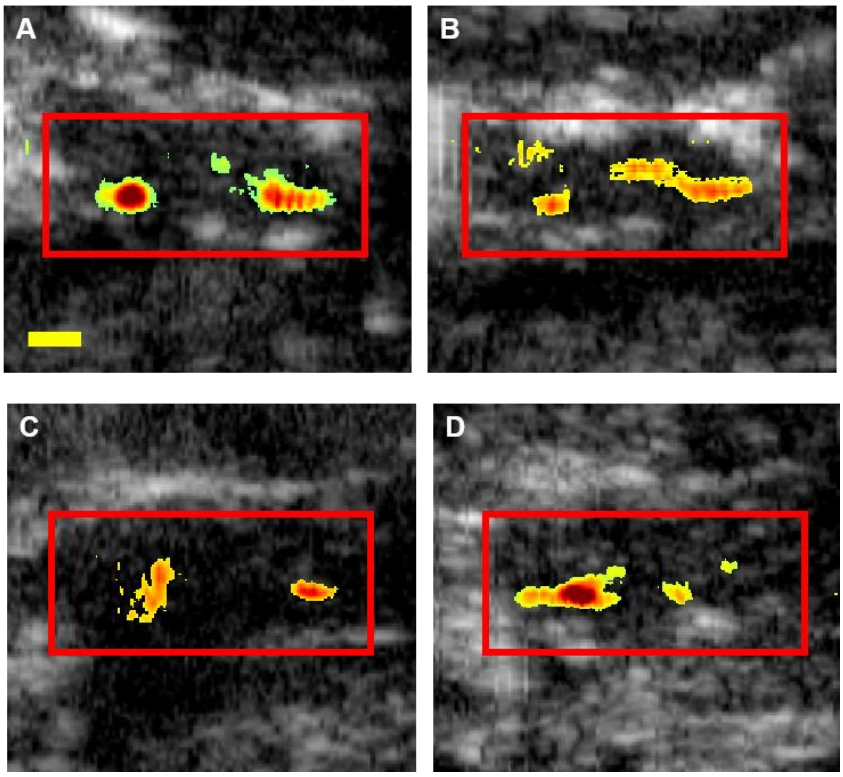

Figure 43. Longitudinal monitoring of PBNC-labeled MSCs with US/PA imaging *in vivo* – coronal views. Three-dimensional PA datasets were integrated with depth (y-dimension) to create a maximum intensity projection and produce coronal maps of PBNC-labeled MSCs at day 5, 7, 10, and 14 post-operatively (A – D), respectively. Red box indicates approximate location of the spinal cord. Scale bar = 3 mm.

After 14 days, animals were sacrificed for histology to verify presence of PBNC-labeled MSCs. PBNCs were visible on eosin-stained tissue sections with brightfield microscopy due to their blue color (Figure 44A and 44B). The large aggregates of PBNCs may indicate internalization in cells (Figure 44B). However, as was the case for intraoperative studies, brightfield microscopy only confirmed presence of particles, not stem cells. Stem cells were also double-labeled with a fluorescent dye, in addition to PBNCs in culture prior to injection into the cord. Thus, presence of PBNC-labeled stem cells was confirmed with confocal microscopy by green fluorescence (Figure 44C).

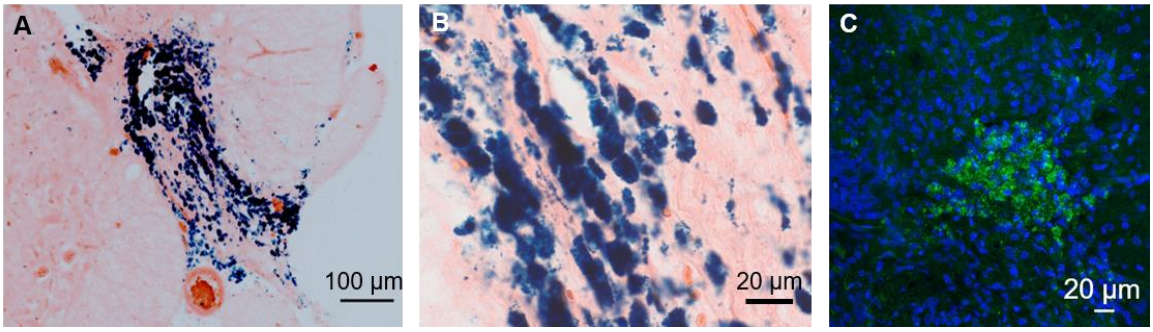

Figure 44. Confirming presence of PBNC-labeled MSCs after 14 days post-injection. Stem cells were double-labeled with PBNCs and a fluorescent dye, CellTracker Green. (A, B) Brightfield microscopy of eosin-stained spinal cords and blue PBNCs. (C) Confocal microscopy of DAPI-stained spinal cord and green fluorescent stem cells.

4.5 Discussion

In previous work, we demonstrated use of AuNSs to detect stem cells in the spinal cord with US/PA imaging.[174] Although AuNSs are a widely-used contrast agent for PA imaging, PBNCs have several benefits. Regarding optical properties, PBNCs have a peak optical absorption at longer wavelengths, ~740 nm wavelength compared to ~680 nm wavelength for AuNSs, which allows PA imaging at greater depths and may improve detection. Regarding magnetic properties, PBNCs produce MR contrast, which is not possible with pure AuNSs. Magnetic contrast may expedite translation due to compatibility with MRI, which is the gold standard for spinal cord imaging. Although PBNCs are in preclinical development, precursor components are FDA approved, which may further simplify regulatory hurdles and translation. In addition, we previously explored PBNC cytocompatibility.[126] No effects on stem cell potency or viability were observed, even when MSCs were exposed to higher concentrations of PBNCs compared to those used here. Cytocompatibility over longer time periods remains to be assessed. For these reasons, PBNCs are a promising contrast agent for stem cell imaging in the spinal

cord with clear benefits compared to previous studies with AuNSs. The trimodal US/PA/MRI platform augmented with PBNCs provides a variety of options for intra- and post-operative detection of stem cells in the spinal cord in research and clinical settings.

PA and MRI detection capabilities of PBNC-labeled MSCs were compared *in vitro*. Results indicated PA imaging was able to detect less than 100 cells/µl. MRI had a detection threshold of ~300 cells/µl. Although *in vitro* results indicated PA imaging was more sensitive to PBNC-labeled MSCs, PA and MRI detection limits may vary in tissue. More specifically, light penetration will reduce detection capabilities of PA imaging *in vivo*. However, for *in vivo* studies 10k cells/µl were injected per the clinical protocol, which is roughly a 30- and 100-fold increase over the MR and PA detection limits observed in phantom studies. As a result, we were able to detect PBNC-labeled stem cells *in vivo* up to two weeks post-injection. Considering the low detection threshold of phantom results, it may be possible to detect stem cells at even longer time points. However, this may not be required based on clinician feedback.

Features of the US/PA/MR imaging platform augmented with PBNCs were demonstrated in experiments mimicking intra- and post-operative situations *ex vivo* and *in vivo*. PA imaging was inherently well-suited for intraoperative imaging due to the smaller footprint, OR compatibility, lower cost, and fast image acquisition to allow real-time imaging. Although intraoperative MRI exists, implementation is challenging and high cost is limiting.[180–182] One feature of intraoperative US/PA imaging was real-time guidance of the direct stem cell injection into the spinal cord. Research has shown that direct injection into the spinal cord has higher likelihood of therapeutic success.[186] However, it comes with higher risk due to more likely damage to the spinal cord during needle insertion.

Intraoperative needle guidance can help assure safe needle placement and success of the stem cell injection, indicated by stem cell retention in the spinal cord, dose delivered, and accuracy of injection location.[5,43,190]

We previously investigated the use of ultrasound only to guide needle placement into the spinal cord.[137] Here, the use of PA imaging was investigated for the same purpose.[97] In the *ex vivo* study, the needle shaft was barely visible using ultrasound alone at 20 MHz imaging frequency, but was clearly highlighted with PA imaging at 740 nm wavelength. One reason for this is the angular dependence of ultrasound.[97] Compared to ultrasound, PA imaging is less dependent on the object angle relative to the transducer because contrast is based on light absorption, not backscattering. As a result strong PA signals were generated from the needle regardless of orientation.[97] Thus, intraoperative PA imaging may be a better option for needle guidance, while intraoperative ultrasound provides anatomical context. Needle guidance was also possible during *in vivo* intraoperative imaging. An additional benefit of real-time guidance with US/PA imaging was highlighted as movement in the spinal cord from breathing was also visible, which may change the injection location and have implications on injection safety. In fact, neurosurgeons have developed a spinal cord derrick to guide and stabilize direct injections into the spinal cord for this very reason, which further highlights the importance and clinical need for image guidance [47].

After needle placement, the PBNC-labeled MSC injection was detected in real-time using US/PA imaging with both *ex vivo* and *in vivo* studies. From a clinical perspective, results can provide physicians with immediate feedback on injection success intraoperatively. Currently feedback on injection volume, location, and stem cell retention

would likely be confirmed with post-operative MRI due to limited availability of intraoperative MRI systems. Thus, intraoperative information is often unavailable to indicate failed stem cell delivery in real-time, highlighting a benefit of the intraoperative US/PA imaging approach. In a research setting, therapy development can also proceed more efficiently by immediately confirming delivery success. US/PA results from intraoperative-mimicking studies were compared to MRI. There was good agreement between modalities, and PBNC-labeled MSCs were detected at similar locations. Some differences in injection morphology were observed and were suspected to result from differences in imaging slice, rat orientation, and detection sensitivity of PBNCs-labeled MSCs with PA and MRI.

To initially assess post-operative potential of the trimodal US/PA/MRI approach, a layer of muscle was replaced on top of the spinal cord post-injection to mimic the clinical procedure *ex vivo*. Even in clinic, bone is not replaced after the surgery,[173] providing a convenient US/PA imaging window. PBNC-labeled MSCs were still detectable with PA imaging in spite of the additional muscle layer, indicating feasibility of post-operative US/PA imaging and motivating *in vivo*, longitudinal studies with US/PA/MRI.

For *in vivo* longitudinal studies, scattering from the skin and increased imaging depth due to swelling at the surgical site required use of higher laser energies. In *ex vivo* studies, PBNC-labeled MSCs were visible with approximately 7 mJ/cm^2 at 740 nm wavelength. However, approximately 20 mJ/cm^2 was required to visualize PBNC-labeled stem cells for *in vivo* studies. PBNC-labeled MSCs were ultimately visible at 14 days post-injection with both MRI and PA imaging in rats. Although MRI still has the advantage for post-operative imaging due to ease of whole body penetration, detection of PBNC-labeled

stem cells with PA imaging for *in vivo* longitudinal studies brings a new opportunity to implement a low-cost alternative that provides complimentary information to MRI.

Results from *in vivo* longitudinal studies were confirmed with histology in addition to MRI. Although MRI is the best comparison for verifying PA results, neither modality can distinguish the presence of PBNC-labeled MSCs versus PBNCs alone or PBNCs transferred to another cell type. By double-labeling the PBNC-labeled MSCs with a fluorescent dye, CellTracker Green, presence of double-labeled MSCs in the spinal cord verified US/PA/MRI results with optical methods. However, confirmation with confocal fluorescent microscopy was not ideal. One issue was physical blockage of fluorescent signal from highly concentrated PBNCs within cells, which diminished green fluorescence from double-labeled MSCs. In spite of this, optical microscopy still depicted some green fluorescent signal from PBNC-labeled MSCs. Together with PA and MR results, histology further validated presence of PBNC-labeled MSCs at 14 days post-injection.

4.6 Conclusions

Results showed proof-of-concept of a trimodal US/PA/MR imaging approach for intraoperative guidance of stem cell delivery in the spinal cord and longitudinal monitoring of stem cells up to 14 days post-operatively. A key aspect of this approach was the use of a unique formulation of Prussian blue nanocubes, developed in-house,[148] to produce multi-modal PA/MR contrast. MSCs were labeled with 200 nm PBNCs in culture. *Ex vivo* and *in vivo* US/PA/MRI studies in rats demonstrated several features supporting intra- and post-operative usability, including real-time needle and injection guidance, immediate feedback on stem cell delivery success, and longitudinal multi-modal stem cell detection. PA and

MR images showed good agreement on stem cell location in intra- and post-operative scenarios. In the future, long term effects of PBNCs must be assessed. To fully evaluate PBNC cytocompatibility, impact on stem cell secretory profile should also be assessed, and particle clearance must also be evaluated. Overall PBNCs may facilitate new opportunities to guide stem cell therapies in the spinal cord, and results lay the groundwork for a customizable trimodal imaging approach.

4.7 Future work

The key next steps to advance the trimodal imaging approach for applications in the spinal cord are large animal studies and implementation of functional imaging. Although *in vivo* studies in rodents were necessary to justify future work, studies in porcine models are critical to assess clinical feasibility. Regarding functional imaging, detecting stem cell location was first required to provide foundational monitoring information. Now that location was detected, the platform can be further developed for more sophisticated monitoring. Specifically, functional monitoring is desired to provide functional information regarding stem cell status and therapy progression, such as stem cell viability, proliferation, and differentiation, or blood flow and oxygenation. For these reasons, current efforts are focused on spinal cord imaging in porcine models and developing a sensor to detect stem cell apoptosis. Both aspects have been explored in preliminary experiments detailed here.

Translation of intraoperative US/PA imaging to an *ex vivo* porcine spine was assessed. A porcine spinal column was obtained from the slaughterhouse and was similarly prepared by performing a laminectomy to expose the underlying spinal cord. In this case,

PBNCs alone were injected at two sites along the spinal cord followed by US/PA imaging to mimic the intraoperative scenario. The spinal cord was imaged with both a 15 MHz and 20 MHz transducer. It was initially expected that the 15 MHz transducer would be favored for large animal studies due to greater possible imaging depth of the lower frequency transducer. However, the 20 MHz transducer was preferred. The smaller footprint of the transducer allowed closer positioning to the spinal cord to maximize fluence at the PBNC injection sites and higher frequency better visualized anatomy. Both injection sites were visible with US/PA imaging in 2D sagittal views (Figure 45A and 45B). Although each site was theoretically injected with 25 μl of PBNCs, the injection footprint differed. Three-dimensional volumetric US/PA images confirmed this result, which highlighted variability in the procedure and an opportunity to improve consistency with image guidance (Figure 45C). After imaging, the spinal cord was excised from the spinal column and cut in half to confirm presence of PBNCs (Figure 45D).

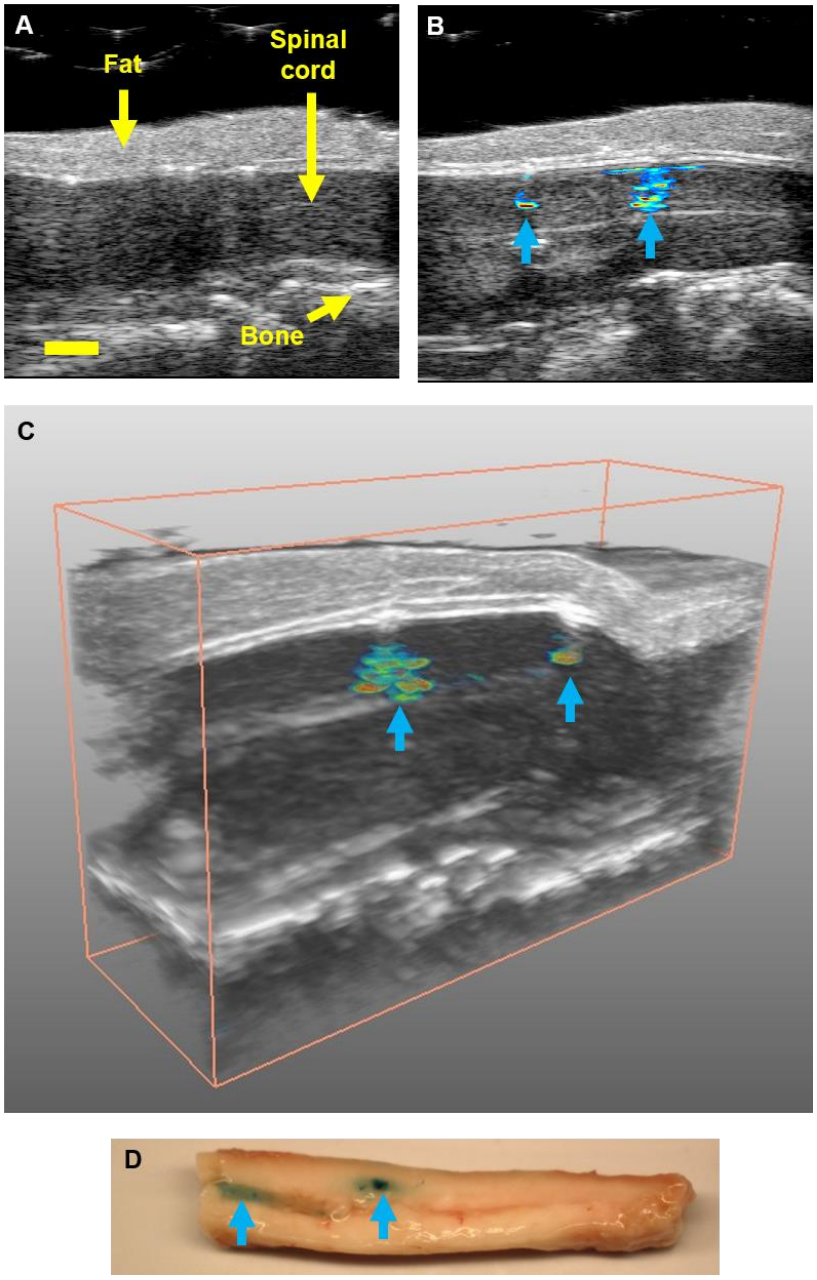

Figure 45. US/PA imaging of PBNCs in a porcine spine *ex vivo*. A 25 µl volume of PBNCs (blue arrows) was injected directly into the spinal cord at two locations. Two-dimensional US (grayscale) and PA (color scale) sagittal views before (A) and after (B) injection. Three-dimensional US/PA volumetric image visualized the injection bolus (C). The spinal cord was excised and both injections were observed (D). Scale bar = 3 mm.

Although a high concentration of PBNCs was injected in this case (~50 OD), results indicated feasibility of intraoperative US/PA imaging in a large animal model, which is an

important steps towards feasibility in patients. However, many factors must be considered for translation of the trimodal imaging approach to large animals *in vivo* and humans for post-operative monitoring. First, light penetration and imaging depth are concerns for post-operative monitoring. Currently, US and PA imaging depths of ~15 cm and ~7 cm, respectively, can be reached.[13,191] In humans, the distance from the spinous process to the spinal column is approximately 1 – 2 cm in the cervical region, 3 – 7 cm in the thoracic region, and 3 cm in the lumber region. Dimensions are similar for pigs.[187] Based on these dimensions, post-operative US/PA imaging may be feasible due to the imaging window created by lack of bone, but anatomical distance to the spinal cord will still challenge the penetration limit of current PA imaging hardware. If the current PA imaging depth is insufficient, it may be possible to detect PBNC-labeled MSCs using more complex ultrasound detection mechanisms, such as magnetomotive imaging.[192] Alternatively, technological advances in light delivery may eventually allow post-operative PA imaging of stem cell therapies in the spinal cord of large animals or humans. In the meantime, the great advantage of PBNCs is that MRI can be used for post-operative monitoring immediately, while US/PA imaging can still benefit stem cell therapies with intraoperative guidance.

To address the need for functional stem cell monitoring, a PA imaging probe to assess stem cell apoptosis was developed. Although substantial functional information related to cell and tissue status is desired, our initial focus is on apoptosis due to relevance to a wide range of stem cell tracking applications. A probe consisting of the DEVD peptide sequence, an optically-absorbing dye, and an aggregating/quenching (AgQ) unit was synthesized. Note that the probe design does not include any nanoparticles. The overall

detection scheme is illustrated in Figure 46. While a cell is alive, the dye component of the probe is fluorescently active, and, as a result, the photoacoustic signal is low. Upon cell apoptosis the DEVD peptide motif is cleaved by caspase-3, a key mediator of apoptosis that is activated by a variety of signals triggering programmed cell death.[193] Cleavage allows the probe to self-polymerize and aggregate. More specifically, aggregation of the dye quenches fluorescent activity and decreases quantum yield, which in turn increases PA signal.[194,195] Therefore enhanced PA signal corresponds to cell apoptosis.[196,197]

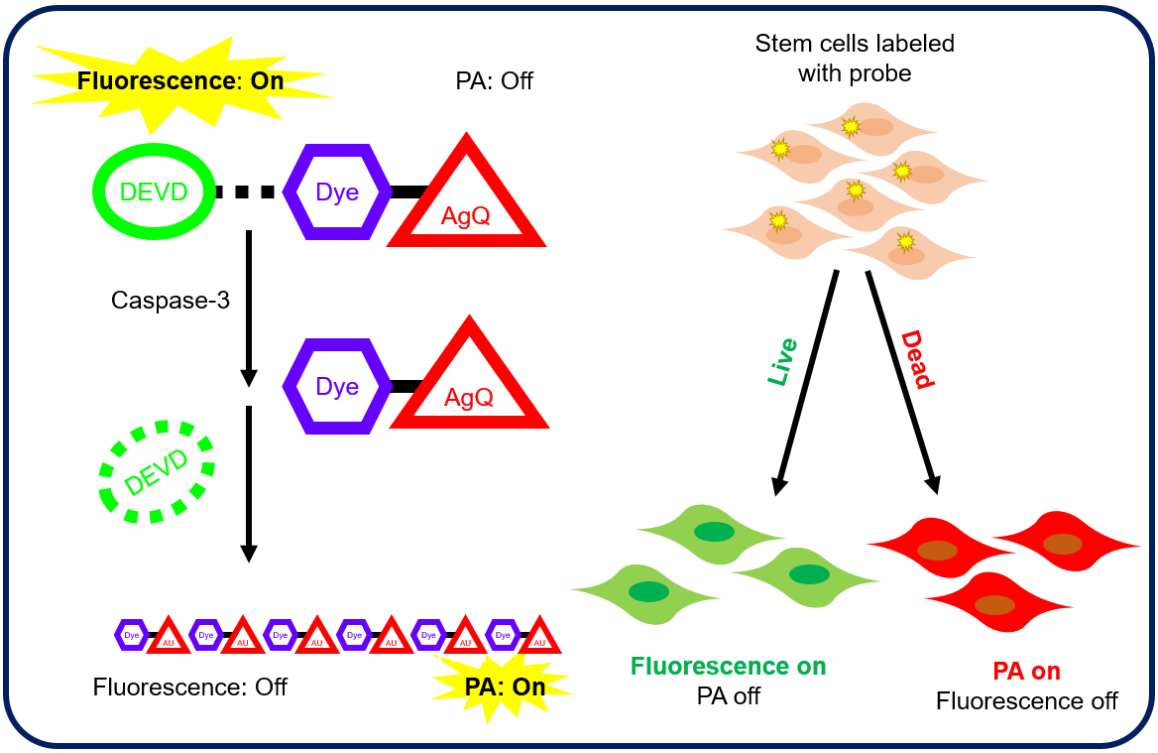

Figure 46. Detection scheme of the stem cell apoptosis probe. The probe consists of the DEVD peptide sequence (green oval), dye (purple polygon), and an aggregating/quenching unit (AgQ; red triangle). Upon cell apoptosis, caspase-3 cleaves the DEVD motif, allowing the probe to aggregate and enhance PA signal corresponding to cell apoptosis.

After synthesis, probe function was tested in tissue-mimicking phantom experiments. MSCs were incubated with the probe overnight in cell culture. The next day,

the media was collected, and MSCs were washed with PBS to remove any residual probe. The media was replaced and supplemented with .2 μg/ml of doxorubicin. After four hours, the cells and media were collected for phantom preparation and US/PA imaging. Dome-shaped inclusions consisted of the naïve live cells, probe-labeled dead cells, and the probe alone. Representative US/PA images showed dead cells labeled with the probe produced a PA signal at 700 nm wavelength (Figure 47B). Analysis of the PA spectrum of each inclusion showed an increased PA signal and spectral shift upon cell death (Figure 47B and C). While it is difficult to make conclusions based on changes in magnitude of the PA signal, the spectral shift observed from ~800 nm wavelength to ~700 nm wavelength in the probe alone versus the probe-labeled MSCs may better distinguish cell apoptosis.

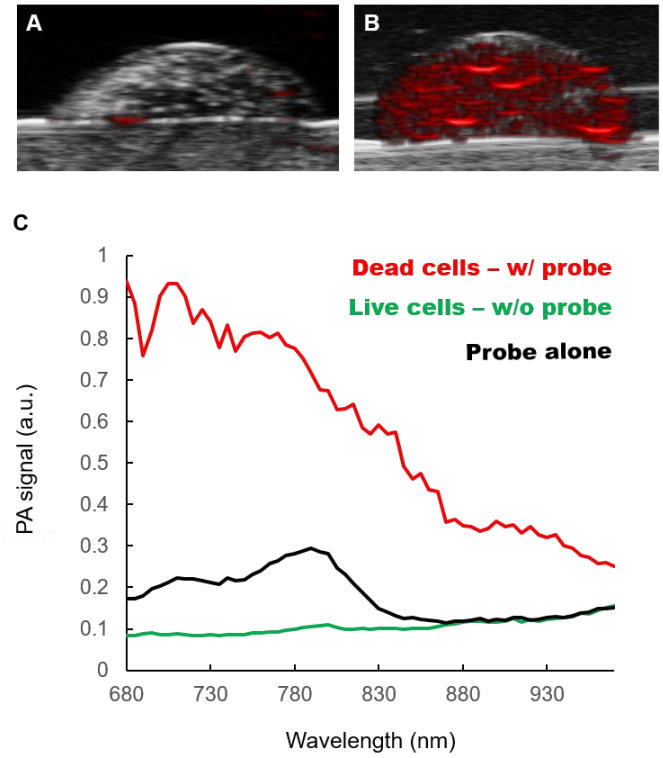

Figure 47. Assessing stem cell apoptosis detection *in vitro* in a tissue-mimicking phantom. Combined ultrasound (grayscale) and PA (color scale) images of live, unlabeled MSCs (A) and dead MSCs incubated with the probe (B). (C) PA spectra of dead cells (red line), live cells (green line), and the probe alone (black line).

Although results demonstrated changes in the PA signal from the probe upon cell death, there were many issues identified in this study. First, cell death was primarily caused by the probe itself. After overnight incubation with the probe alone, many MSCs were discovered floating and lysed in the media the following day before any doxorubicin was added. To salvage the experiment, the media containing the dead, lysed cells incubated with the probe was also collected and imaged in the tissue mimicking phantom. This sample is identified as "Dead cells – w/ probe" above (Figure 47). In later studies, further purification steps during probe synthesis eliminated cell death and lysis caused by the probe. However, once the probe no longer caused cell lysis, there was also no longer any

change in the PA signal upon cell apoptosis. Thus, cells did not efficiently endocytose the probe to allow PA detection of caspase activation in the cytoplasm. Overall, initial success (Figure 47) was observed because cell lysis allowed caspase-3 to access the probe external to the cells.

To address this problem, laser delivery of the probe using perfluorocarbon nanodroplets was attempted. The idea is similar to sonoporation, but instead laser light irradiation of nanodroplets provides the mechanical stimulus to open the cell membrane.[198,199] The labeling scheme is depicted in Figure 48A. Briefly, stem cells were incubated with a cocktail of the apoptosis probe and light-activated nanodroplets, which contained a dye absorbing at 1064 nm wavelength. Upon laser irradiation at 1064 nm, the droplets vaporized to generate acoustic waves, which can mechanically stimulate transient opening of the cell membrane to allow the probe to enter. In tissue-mimicking phantom studies, results indicated delivery of photoacoustic absorbers into the cells (Figure 48B–E); however, substantial background signal was observed in the light-irradiated cells incubated with nanodroplets only (Figure 48D and 48E). Thus, it appeared that the 1064 nm dye more favorably crossed the cell membrane rather than the apoptosis probe. Although development of this laser-based delivery technique would be beneficial for various applications, use of existing technologies, such as electroporation, may be a better immediate solution to deliver the apoptosis probe to MSCs in culture.

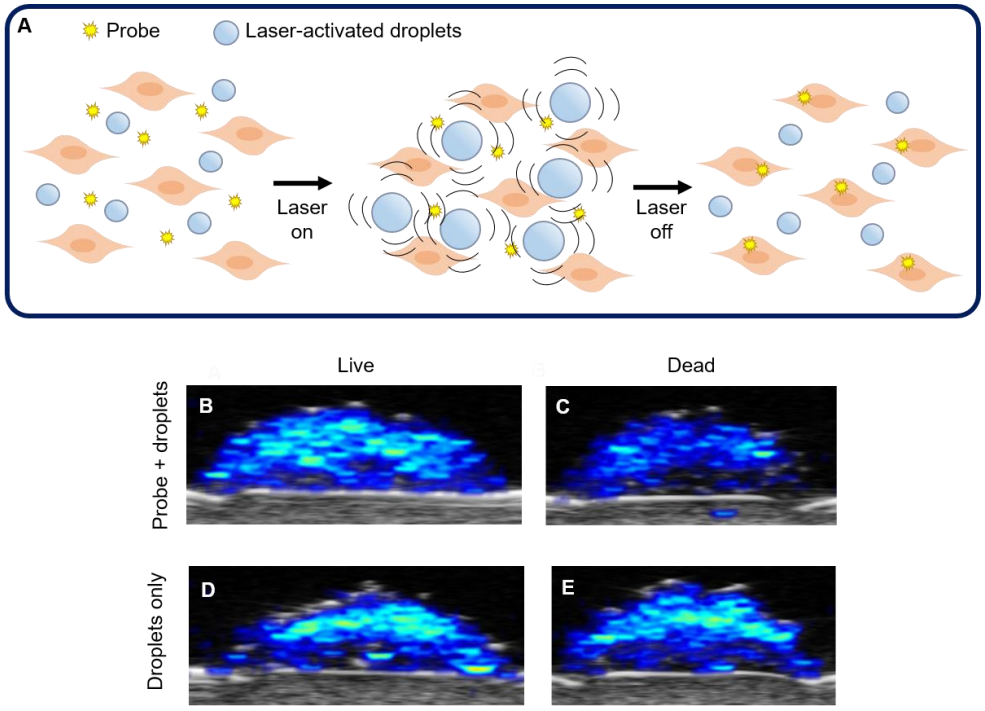

Figure 48. Apoptosis probe delivery using light-activated nanodroplets. Laser light-activated nanodroplets may be able to temporarily permeabilize the cell membrane through acoustic stimulation to improve delivery efficiency (A). Combined ultrasound (grayscale) and PA (color scale) images of live (B, D) and dead stem cells treated with doxorubicin (C, E). Top row (B, C): stem cells incubated with the probe and nanodroplets. Bottom row (D, E): stem cells incubated with nanodroplets only. All groups were irradiated with 300 laser pulses for duration of 10 ns at a frequency of 10 Hz.

4.8 Contributions from collaborators

In this chapter, specific contributions were made by Eleanor Donnelly, Diego Dumani, Jisha V.S., Andrew Zhao, and Johannes Leisen. Eleanor Donnelly provided training to execute the *in vivo* surgeries. Diego Dumani conducted the SQUID experiment for PBNCs. Jisha V.S. synthesized the apoptosis probe. Andrew Zhao synthesized light-activated nanodroplets and tested laser parameters to deliver the caspase-3 probe. Johannes Leisen provided expertise and training to execute magnetic resonance imaging studies.

CHAPTER 5. TRACKING PARTICLES TO INFORM VACCINE DESIGN

This work was presented at two conferences:

Kubelick, K.P., Pradhan, P., Roy, K., & Emelianov, S. Ultrasound and Photoacoustic Imaging to Aid Design, Optimization, and Validation of Pathogen-like Particle Vaccines. IEEE International Ultrasonics Symposium, Kobe, Japan, October 2018.

Kubelick, K.P., Pradhan, P., Roy, K., & Emelianov, S. Tracking Vaccine Particle Trafficking to the Lymph Node using Ultrasound/Photoacoustic Imaging Tools. Biomedical Engineering Society (BMES) Annual Meeting, Atlanta, GA, October 2018.

5.1 Abstract

Development of particulate vaccines, termed pathogen-like particles (PLPs), is of interest to stimulate a more robust immune response compared to traditional, small molecule formulations. Physical properties of PLPs can be tailored to impact trafficking to the lymph node, cell-particle interactions, and ultimately vaccine mechanism of action. To expedite development of PLPs, a minimally invasive, longitudinal monitoring tool is needed to understand the impact of vaccine particle design on the immune response *in vivo*. Thus, we have developed an ultrasound/photoacoustic (US/PA) imaging platform to track PLPs during trafficking to the lymph node, which can provide insight on how to effectively design PLPs to stimulate a robust immune response. Several types of PLPs, composed of poly(lactide-co-glycolic acid) (PLGA), were synthesized using a water-oil-water double emulsion method. Different optical absorbers for PA or fluorescent imaging were encapsulated within the PLPs. The most promising formulation, nano-sized PLPs (nPLPs),

~300 nm diameter and loaded with dye absorbing at 950 nm wavelength, was assessed with US/PA imaging *in vivo*. BALBL/c mice received subcutaneous injections of Dye950-nPLPs, and the inguinal lymph node was imaged at multiple time points up to 48 hours post-injection. Dye950-nPLPs were then coated with an adjuvant, CpG, to mimic vaccine particles and compare differences in PLP trafficking. Spectroscopic analysis of multi-wavelength PA datasets detected presence of uncoated and adjuvant-coated Dye950-nPLPs. Accompanying changes in lymph node swelling and blood accumulation were also observed. Several technical challenges remain, including sensitivity of particle detection, and crosstalk between particles and endogenous absorbers due to overlapping optical spectra, which motivate research areas for further development. Overall, initial results indicated the potential of the US/PA imaging platform to inform particulate vaccine design, which may be applicable to particle tracking in other applications in the future.

5.2 Introduction

Development of particulate vaccines, termed pathogen-like particles (PLPs), is of interest to stimulate a more robust immune response compared to traditional, small molecule formulations.[58,59] Physical properties of PLPs can be tailored to control vaccine delivery and ultimately mechanism of action by manipulating trafficking to the lymph node and cell-particle interactions.[54] Particle size, composition, and surface coating can all be tailored to engineer immunity, leading to endless design combinations.[58,200,201] For example, considering surface coating alone, the type of coating, surface molecule density, resulting particle charge, and hydrodynamic radius all impact immune response. Though an incredible variety of particles have been developed to date, outcomes are not well understood.[58] This can be partly attributed to the lack of *in vivo* monitoring techniques to

evaluate particle interactions with the immune system. To expedite development of PLPs, a minimally invasive longitudinal monitoring tool is needed to understand the relationship between vaccine particle design and the resulting immune response *in vivo*.

Other than histology, one existing option to address this need is two-photon intravital imaging. Two-photon intravital imaging has drastically advanced understanding of the immune system *in vivo*.[60,61] This purely optical method is an excellent option for cellular and molecular-level imaging due to high resolution and compatibility with existing optical dyes to monitor complex cellular and molecular responses. Although certain lymph nodes are quite superficial, two-photon microscopy still lacks sufficient imaging depth for *in vivo* monitoring, which is why two-photon intravital imaging was developed. Intravital imaging requires a highly invasive, specialized surgical procedure, where the skin is removed and replaced with a transparent viewing window to facilitate optical imaging. Thus, two-photon intravital imaging increases imaging depth by eliminating light scattering and attenuation at the skin. An alternative option is the commercially available fluorescent *in vivo* imaging system (IVIS; PerkinElmer). However, resolution is poor and sensitivity and imaging depth are limited by optical scattering from the skin.

Although current optical imaging techniques are not ideal, the desirable attributes of these systems are clear, specifically high resolution, high contrast, and the potential to detect many cellular or molecular events simultaneously using the wide variety of available optical absorbers. Considering the characteristics of an ideal system, ultrasound (US)-guided photoacoustic (PA) imaging is an excellent alternative. As a combined optical and acoustic modality, PA imaging captures the best of both worlds for lymph node imaging by providing high resolution, optical-based contrast at greater imaging depths than purely

optical methods. For this reason, PA imaging has been widely used for other applications of lymph node imaging using nanodroplets, metallic nanoparticles, endogenous optical absorbers, and dyes.[12,62–65]. However, US/PA imaging tools have not been specifically developed to monitor vaccine particle trafficking to the lymph node.

In this chapter, nano-sized PLPs (nPLPs) with a diameter of approximately 300 nm were synthesized.[54,55,57] An optically absorbing dye, Dye950, was encapsulated within the nPLPs to generate PA contrast. The first batch of Dye950-nPLPs received no further surface modification. A second batch of Dye950-nPLPs was coated with an adjuvant, CpG, to mimic a vaccine particle. BALB/c mice received subcutaneous injections of uncoated or adjuvant-coated particles while US/PA datasets were acquired up to 48 hours post-injection. Spectroscopic PA analysis was implemented to distinguish Dye950-nPLPs from the background. Results provided information on particle trafficking to the lymph node, particle localization within the lymph node, and morphological changes at the lymph node. Furthermore three-dimensional (3D) US/PA volumetric images visualized particle distribution from the injection site to the inguinal lymph node. Together, these pieces of information can indicate passive drainage or active cellular transport of PLPs to the lymph node. If and how PLPs arrive to the lymph node ultimately impact the immune response and vaccine mechanism of action.[54,202–204] Thus, results lay the groundwork for developing a US/PA imaging platform to inform vaccine design and monitor more complex cell-particle interactions in the future.

5.3 Materials and methods

5.3.1 Particle synthesis and characterization

All materials were used as received. PLGA (RG502H, Sigma-Aldrich) PLPs were synthesized via a water-oil-water double emulsion and all subsequent coating steps followed previously established methods described elsewhere.[54–57] Small modifications were made to the protocol to incorporate photoacoustic or fluorescent dye.

Briefly, to synthesize micron-sized PLPs (mPLPs) with ~ 1 micron diameter, 200 mg of PLGA and 8 mg of hydrophobic dye, either DiI (Sigma-Aldrich), Epolight 9151 (Epolin; referred to as Dye750), or Epolight 3832 (Epolin; referred to as Dye950), were dissolved in 10 ml of dichloromethane (Sigma-Aldrich) and added to 300 µl of deionized ultra-filtered (DIUF) water. The solution was homogenized at ~10,000 rpm (SL2T) for 2 minutes. The first emulsion was then added to 50 ml of 1% polyvinyl alcohol (PVA; Sigma-Aldrich) and homogenized at the same speed for 2 minutes. The second emulsion was added to a beaker containing 100 ml of 1% PVA and stirred gently for 3 hours in a fume hood. Following solvent evaporation, particles were centrifuged at 3500 rpm for 20 minutes. The pellet was resuspended in 2 ml of DIUF water, and the process was repeated three times. After the final centrifugation step, the resuspended PLPs were flash frozen in liquid nitrogen, and the sample was lyophilized (FreeZone, Labconco) for at least 3 days. After drying, the sample was weighed and stored at -20˚C.

Methods to synthesize nPLPs with ~300 nm diameter were also previously established elsewhere.[54–57] Briefly, the same amount of PLGA and hydrophobic dye was dissolved in 4 ml of dichloromethane and sonicated (Q700, QSonica) at approximately 85

W for 2 minutes in the presence of 1 ml DIUF water. In the second emulsion, the sample was added to 16 ml of 5% PVA and sonicated at the same power for 5 minutes. The double emulsion was poured into a beaker and gently stirred for 3 hours in a fume hood. Following solvent evaporation, particles were centrifuged at 3500 rpm for 20 minutes to remove large, pelleted PLPs. The supernatant was then centrifuged at 20,000 G for 20 minutes. The pellet was resuspended in DIUF water and centrifuged two additional times. After the final spin, the pellet was lyophilized following the above protocol.

In preparation for adjuvant-coating, nPLPs were coated with branched polyethylenimine (bPEI; Polysciences) via well-established surface activation methods described by others.[56,57] Briefly, 200 mg of PLPs were resuspended in 3 ml of ice cold 0.1 M MES (Sigma-Aldrich) buffer. Two separate solutions of 40 molar excess EDC (Sigma-Aldrich) and 25 molar excess sulfo-NHS (Sigma-Aldrich) in 1 ml of 0.1 M MES were prepared. The sulfo-NHS solution was added to the PLPs, followed by the EDC solution. Samples were covered in aluminum foil followed by gentle shaking at room temperature. After 2 hours a bPEI solution consisting of 14.1 ml bPEI, 28.2 ml of 0.2 M MES buffer, and 1.8 ml HCl (37%, VWR) was added to the PLP solution. The solution was stirred for 2 hours. The PEI-nPLPs were centrifuged at 22,000 G for 20 minutes at 4˚C. The pellet was resuspended in 20 ml of 1M NaCl and centrifuged again using the same parameters. The pellet was resuspended in 20 ml of DIUF water and centrifuged again using the same parameters. After the final spin, the pellet was resuspended in 5 ml of RNAse/DNAse free water and lyophilized following the above protocol.

PEI-nPLPs were next coated with an adjuvant, CpG (tlrl-1826; Invivogen), according to methods previously described elsewhere.[54] A sodium phosphate loading

buffer (pH 6) was obtained from collaborators in the Roy Lab. Two centrifuge tubes containing reaction components were prepared. In Tube 1, 50 μg of CpG was added to 1 ml of loading buffer in a 2 ml low adhesion centrifuge tube (USA Scientific). In Tube 2, 5 mg of PEI-PLPs were added to 1 ml of loading buffer in a 2 ml low adhesion centrifuge tube. Tube 2 was briefly sonicated for 5 – 10 seconds to resuspend PEI-nPLPs. Tube 1 was then secured in a vortex. While Tube 1 was continually vortexed at low speed, the solution from Tube 2 was added dropwise to Tube 1 over one minute. Once the entire solution from Tube 2 was added to Tube 1, the lid on Tube 1 was closed, and the solution was vortexed at high speed for 30 seconds. Tube 1 was wrapped in foil and rotated overnight at 4˚C. The following day the CpG-nPLPs were centrifuged at 3000 G for 20 minutes. The supernatant was kept to determine CpG surface loading on the CpG-nPLPs (Synergy HT microplate reader, BioTek Instruments; single-stranded DNA setting). The pelleted CpG-nPLPs were resuspended at 1 μg CpG/μl in sterile PBS to prepare for *in vivo* injections.

PLP hydrodynamic diameter and surface charge was measured with DLS and zeta-potential, respectively (Malvern Zetasizer Nano ZS). Prior to measurements, PEI-nPLPs were sonicated in a bath sonicator for 10 minutes.

5.3.2 PA assessment of PLPs in a tissue-mimicking phantom

A tissue mimicking phantom was prepared and imaged with US/PA imaging according to the methods described above (see Section 3.3.6). In this case, the dome-shaped inclusions contained uncoated m- and nPLPs loaded with Dye750 or Dye950. Seven different domes were prepared for each type of PLP containing different particle

concentrations: 12.5 mg/ml, 6.3 mg/ml, 3.1 mg/ml, 1.6 mg/ml, 0.78 mg/ml, 0.39 mg/ml, and 0.195 mg/ml.

5.3.3 In vivo studies

In vivo studies were conducted following the Institutional Animal Care and Use Committee (IACUC) guidelines per the Georgia Institute of Technology. Female, BALB/c mice (Charles River Laboratories) were used in these studies.

For US/PA imaging experiments, mice received Dye950-nPLPs with different coatings. More specifically, two mice received uncoated Dye950-nPLPs, and two mice received CpG-coated Dye950-nPLPs (henceforth referred to as "CpG-Dye950-nPLPs"). Anesthesia was induced with 5% isoflurane at a flow rate of 500 ml/min and maintained at 1 - 2% isoflurane at the same flow rate. Hair was removed on the abdomen between the legs and ribs. Mice were injected on the left side near the mammary fat pad with 20 µl of Dye950-nPLPs or CpG-Dye950-nPLPs, which corresponded to 20 mg of nPLPs and 20 µg of CpG, where applicable. Three-dimensional multi-wavelength US/PA datasets were acquired using the Vevo LAZR (see Section 2.3.2 and 3.3.5). Datasets were exported to MATLAB (Mathworks, Inc.) and post-processed with spectroscopic analysis (see Section 2.3.5) to distinguish PA signals from endogenous and exogenous absorbers, in this case blood and Dye950-nPLPs or CpG-Dye950-nPLPs. Three-dimensional volumes were created in AMIRA (Thermo Fisher).

Fluorescent imaging experiments using the *in vivo* imaging system (IVIS Lumina, PerkinElmer) and fluorescent microscopy were conducted to establish a ground truth for

comparison of photoacoustic results. For *in vivo* fluorescent experiments, female, BALB/c mice received DiI-loaded nPLPs (referred to as "DiI-nPLPs") with different coatings. More specifically, three mice received uncoated DiI-nPLPs, and three mice received CpG-DiI-nPLPs. Mice were similarly anesthetized for hair removal and particle injections. In this case, a 20 μl subcutaneous injection was administered on the underside of the left leg, further away from the left inguinal lymph node compared to the injection with photoacoustic particles. After 24 hours, mice were anesthetized again for fluorescent imaging with IVIS. After *in vivo* fluorescent images were acquired, mice were sacrificed for acquisition of *ex vivo* fluorescent images with IVIS. In this case, the skin was removed to expose both inguinal lymph nodes, and the injection site was covered with a piece of gauze to suppress the high fluorescent signal from the injection site to allow detection of low concentrations of particles at the lymph node.

After sacrifice, both inguinal lymph nodes were harvested from all mice. Lymph nodes were sectioned and stained with eosin for brightfield microscopy (Axio Observer, Zeiss) or DAPI for confocal fluorescent microscopy (LSM 700, Zeiss). The staining protocol followed methods described above (see Section 4.3.10).

5.4 Results

5.4.1 Particle synthesis and characterization

Seven different types of photoacoustic PLPs were synthesized with different photoabsorbers, diameters, and particle coatings, as described in Table 3. The original formulation of PLPs, composed of PLGA, does not optically absorb for tracking with photoacoustic imaging, IVIS, or fluorescent confocal microscopy. Thus, various

photoabsorbers were encapsulated within the PLP by adding hydrophobic dyes to the oil phase during the double emulsion synthesis.

Table 3. Description of PLP formulations. The size column indicates target diameter of ~1 μm (micro) or ~300 nm (nano). The absorber column indicates type of dye encapsulated. The coating column indicates whether the PLP has no coating or an adjuvant (CpG) coating. The modality column indicates PA or fluorescent contrast.

Formulation	Size	Absorber	Coating	Modality
1	Micro	Dye950	None	PA
2	Micro	Dye750	None	PA
3	Nano	Dye950	None	PA
4	Nano	Dye750	None	PA
5	Nano	Dye950	CpG	PA
6	Nano	DiI	None	Fluorescence
7	Nano	DiI	CpG	Fluorescence

The optical properties of uncoated photoacoustic PLPs, which contained Dye750 or Dye950, were assessed with UV-Vis spectrophotometry (Figure 49). First, the absorbance spectra of free Dye750 and Dye950 was measured and compared to the known spectra of endogenous absorbers, specifically HbO_2 and Hb.[106–112] Both photoacoustic dyes had a distinct optical signature compared to endogenous absorbers, which indicated potential to distinguish Dye950- or Dye750-PLPs *in vivo* with multi-wavelength PA imaging and spectroscopic analysis. The extinction spectra of Dye950- and Dye750-mPLPs (Figure 49B) or nPLPs (Figure 49C) had similar spectral signatures to the free dye,

indicating successful encapsulation of absorber. Optical scattering was apparent in measurements of Dye950- and Dye750-mPLPs, indicated by noise in the spectra (Figure 49B). Less optical scattering was observed in the measurements of Dye950- and Dye750-nPLPs due to their smaller size (Figure 49C). Unlike, PA imaging, UV-Vis measurements were susceptible to scattering. Spectral shifts were also observed in the dye-loaded PLPs compared to free dye because the optical signature can vary based on concentration of encapsulated dye.

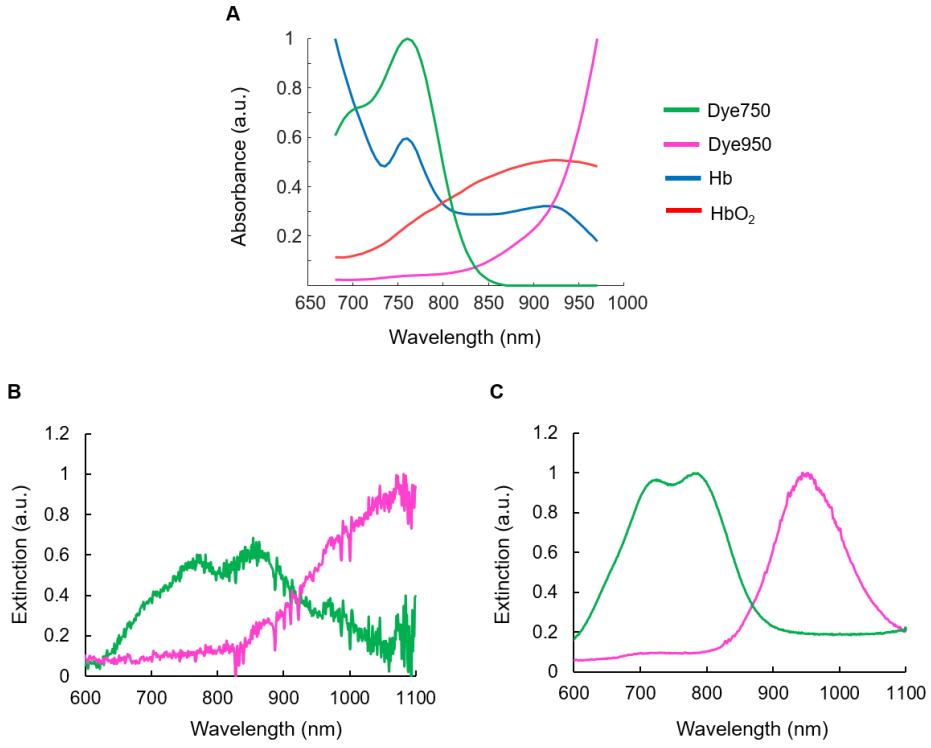

Figure 49. Characterization of PLPs with UV-Vis spectrophotometry. (A) Absorbance spectra of free Dye750 (green), free Dye950 (pink), and relevant endogenous absorbers for lymph node imaging in BALB/c mice, Hb (blue) and HbO_2 (red). Extinction spectra of mPLPs (B) and nPLPs (C) loaded with Dye750 or Dye950. Similar spectral signatures were observed for the free dye and dye encapsulated in the PLPs; however, some differences were observed. Noise in the spectra of mPLPs resulted from scattering of the larger particle. Differences in the ratios between extinction peaks can result from differences in concentration of dye encapsulated in each particle type.

The PA signal of uncoated PA-tagged PLPs was assessed in tissue-mimicking phantom experiments. Seven domes with decreasing concentrations were prepared for each type of PA-tagged PLP to determine the detection limit. PA signal was detected from all four types of PA-tagged PLPs at the lowest concentration of 0.195 mg/ml: Dye950-mPLPs, Dye750-mPLPs, Dye950-nPLPs and Dye750-nPLPs. However, a higher PA signal was observed from the nano-sized formulations. Furthermore, compared to endogenous absorbers Dye950 had a more distinct spectral signature than Dye750, which has a shared peak with Hb (Figure 49). For these reasons, the following *in vivo* studies described hereafter were conducted with Dye950-nPLPs because characterization determined this was the most promising formulation to allow US/PA detection.

Dye950-nPLPs were further characterized with DLS to determine the hydrodynamic radius (Table 4). Results were compared to uncoated PLPs that were not loaded with any dye, and DiI-nPLPs for fluorescent imaging. Additional measurements were acquired after coating the Dye950- and DiI-nPLPs with PEI. The uncoated nPLPs had a smaller hydrodynamic diameter of 277.5 nm compared to that of the Dye950-nPLPs or DiI-nPLPs, at 301.7 nm and 330.9 nm, respectively. This may indicate some dye coating the PLP surface. As expected, hydrodynamic diameter increased when the particles were coated with PEI. Particles also tended to aggregate after the PEI coating step. The PEI-Dye950-nPLPs seemed more susceptible to aggregation than the PEI-DiI-nPLPs with a hydrodynamic diameter of 2654 nm compared to 479.7 nm.

Table 4. Average diameter of different types of nPLPs. PDI = polydispersity index.

Particle type	Z- average diameter (nm)	PDI
nPLP	277.4	0.054
Dye950-nPLP	301.7	0.074
PEI-Dye950-nPLP	2645	0.334
DiI-nPLP	330.9	0.289
PEI-DiI-nPLP	479.7	0.373

Particle surface charge was assessed with zeta-potential (Table 5). The surface charge changed after each coating step as expected based on previous results from others [54]. The uncoated particles had a negative surface charge. After PEI-coating the surface charge became more positive. Finally, the surface charge became more negative after CpG coating. Plate reader measurements determined the CpG surface loading was ~10 μg of CpG/mg of particles for both CpG-Dye950-nPLPs and CpG-DiI-nPLPs.

Table 5. Comparing surface charge of nPLPs after each coating step

Particle type	Zeta potential (mV)	Zeta deviation (mV)
nPLP	-31.0	5.73
Dye950-nPLP	-34.3	5.83
PEI-Dye950-nPLP	38.4	5.86
CpG-Dye950-nPLP	9.86	3.09
DiI-nPLP	-19.5	4.06
PEI-DiI-nPLP	20.2	4.76
CpG-DiI-nPLP	-3.31	5.60

5.4.2 In vivo studies using uncoated nPLPs

For the first set of *in vivo* experiments, Dye950-nPLPs (uncoated) were subcutaneously injected near the left mammary fat pad. Uncoated PLPs were initially studied to assess feasibility of PA detection prior to studying a more realistic and complex adjuvant-coated vaccine particle. Multi-wavelength US/PA datasets were acquired continuously for the first 2 hours post-injection and at 24 hours post-injection followed by spectroscopic analysis.

Prior to injection of Dye950-nPLPs, only Hb and HbO_2 were identified, indicating minimal crosstalk between optical absorbers (Figure 50A–C). Crosstalk between endogenous and exogenous absorbers creates detection inaccuracies due to overlapping spectral signatures, which ultimately leads to incorrect identification of blood or particles.

As expected no Dye950-nPLPs were detected prior to injection. Thus, there appeared to be minimal crosstalk between absorbers, and results gave confidence in particle detection at later time points. By 2 hours post-injection, some PLPs were observed at the lymph node periphery (pink arrow; Figure 50L). By 24 hours, more substantial accumulation of PLPs was detected surrounding the lymph node and in surrounding vessels (Figure 50O). Changes in blood spatial distribution were also observed at each time point (Figure 50D and E, G and H, J and K, M and N). However, the difference between signal from Hb and HbO_2 at 2 hours and 24 hours post-injection could result from differences in the imaging frame acquired, as mice were allowed to wake up at 2 hours post-injection and were anesthetized again for US/PA imaging 24 hours later. Note that the injection site was not visible in the same frame as the lymph node in any of the images in Figure 50. Overall results indicated feasibility of detecting Dye950-nPLPs and some accompanying physiological responses.

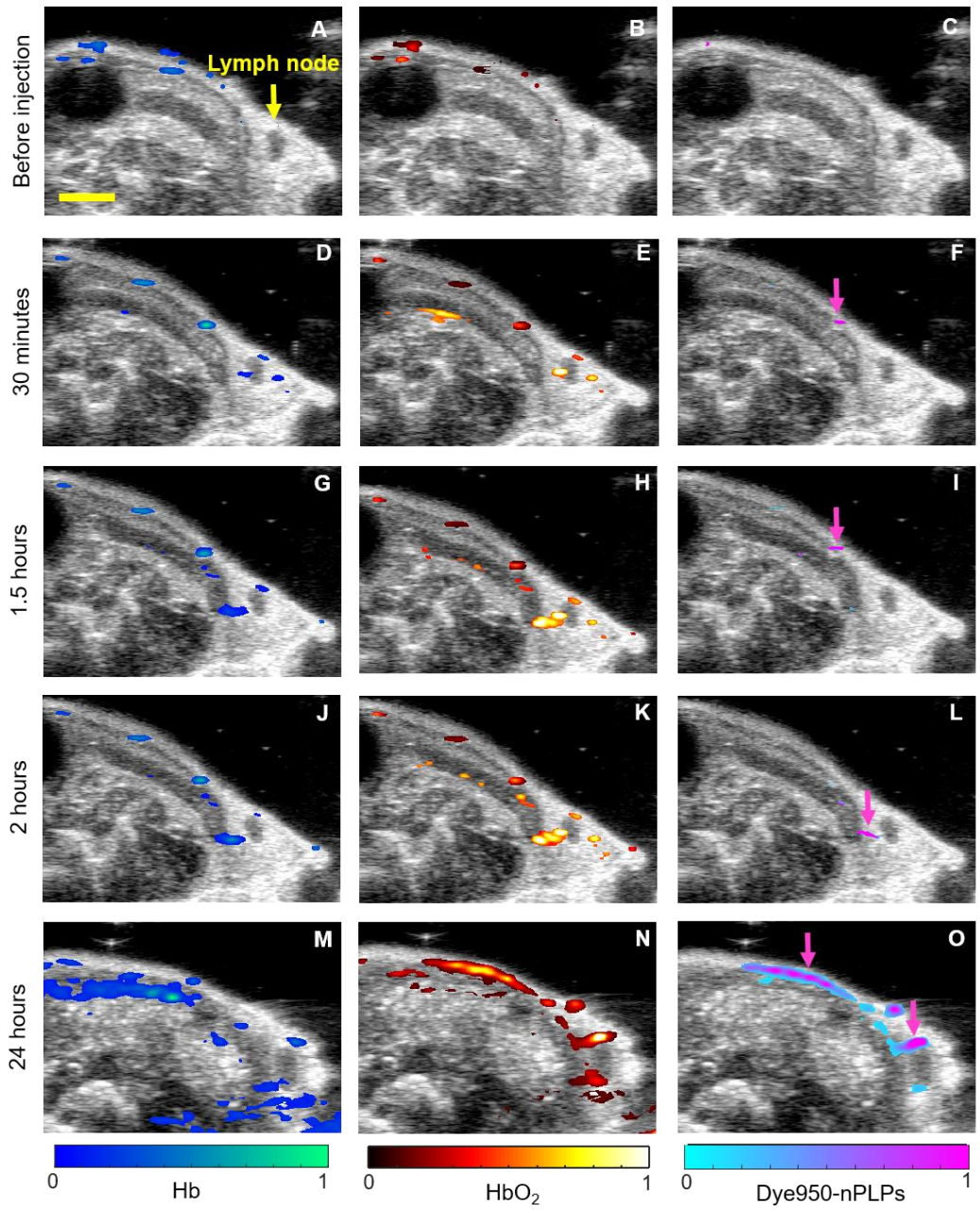

Figure 50. *In vivo* US/PA imaging of Dye950-nPLP trafficking to the lymph node. Ultrasound (grayscale) and PA (color scale) overlay images after spectroscopic analysis to distinguish Hb, HbO_2, and Dye950-nPLPs (columns left to right). Maps of absorber distribution before injection (A – C), 30 minutes (D – F), 1.5 hours (G – I), 2 hours (J – L), and 24 hours (M – O) after injection. PLPs were detected near the lymph node by 2 hours post-injection (L) and more substantial accumulation was observed by 24 hours post-injection (O). Pink arrows point to particles. Scale bar = 3 mm.

To establish a ground truth for *in vivo* PA results, fluorescent experiments were conducted with fluorescent IVIS of DiI-nPLPs, a fluorescent analog for the photoacoustic Dye950-nPLPs. DiI-nPLPs were injected subcutaneously on the underside of the left leg. The inguinal lymph nodes were imaged after 24 hours with IVIS *in vivo* (Figure 51A). Particle accumulation was not visible at the inguinal lymph node with IVIS *in vivo*. The mouse was sacrificed and fluorescent IVIS images were acquired *ex vivo* after peeling back the skin to expose both inguinal lymph nodes and covering the injection site (Figure 51B). Fluorescent signal was visualized at the left inguinal lymph node, i.e. the injected side (ipsilateral), providing some confirmation of PA results. However, the exact distribution of DiI-nPLPs within the lymph node could not be determined due to poor resolution of IVIS. This result highlighted two immediate advantages of the US/PA imaging platform. First, *in vivo* IVIS detection of nPLPs was not possible. Mice had to be sacrificed, and the skin pulled back to allow detection with IVIS. Second, poor resolution prevented IVIS detection of exact nPLP location within the lymph node, even *ex vivo*. US/PA imaging of nPLPs addressed both shortcomings of IVIS as longitudinal *in vivo* monitoring was possible and high resolution specifically depicted particles at the lymph node periphery (Figure 50).

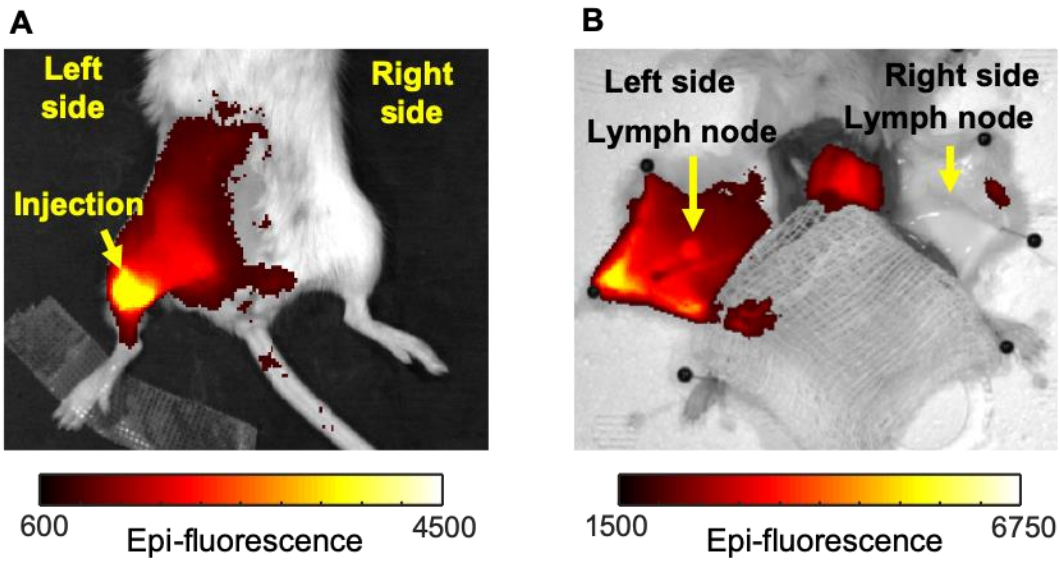

Figure 51. *In vivo* and *ex vivo* fluorescent imaging of DiI-nPLPs. BALB/c mice received subcutaneous injections of DiI-nPLPs and were imaged 24 hours later with IVIS. DiI-nPLP accumulation was not apparent at the left inguinal lymph node *in vivo* while the skin was intact (A). Increased fluorescent signal was present at the left inguinal lymph node *ex vivo* (B).

To further assess nPLP detection capabilities of *in vivo* PA imaging, the inguinal lymph nodes were harvested for histology from mice that received Dye950-nPLPs or DiI-nPLPs. The Dye950-nPLPs appeared dark green in solution, thus it was suspected that particles could be visualized under brightfield microscopy. Eosin-stained tissue may have depicted Dye950-nPLP accumulation based on dark greenish/brown coloration throughout the lymph node (Figure 52A and 52B). Compared to *in vivo* PA imaging results, where Dye950-nPLPs were only detected at the lymph node periphery, brightfield microscopy indicated sensitivity of the current *in vivo* US/PA imaging platform can be improved. Confocal fluorescent microscopy showed DiI-nPLPs (red fluorescence) were primarily localized to the lymph node periphery (Figure 52C and 52D), similar to *in vivo* PA imaging results. Overall, it is important to recognize the standards for success of *in vivo* US/PA

detection of particles cannot be solely based on optical microscopy of tissue sections from harvested lymph nodes. The imaging modalities are far too different, and histology will always be more sensitivity than minimally invasive, US/PA imaging. Thus, it would be unrealistic to aim to design a US/PA imaging system based on the sensitivity of a highly invasive method, such as histology. Results from *ex vivo* IVIS, brightfield microscopy, and confocal fluorescent microscopy also highlight the challenge of establishing a fair ground truth for development of the US/PA imaging platform for particle tracking, as each modality showed slightly different results. In spite of this technical challenge, results have already indicated one benefit of the US/PA platform, the ability for high resolution, minimally invasive, longitudinal detection of particles *in vivo*, which was not possible with any of the other modalities, including *in vivo* IVIS.

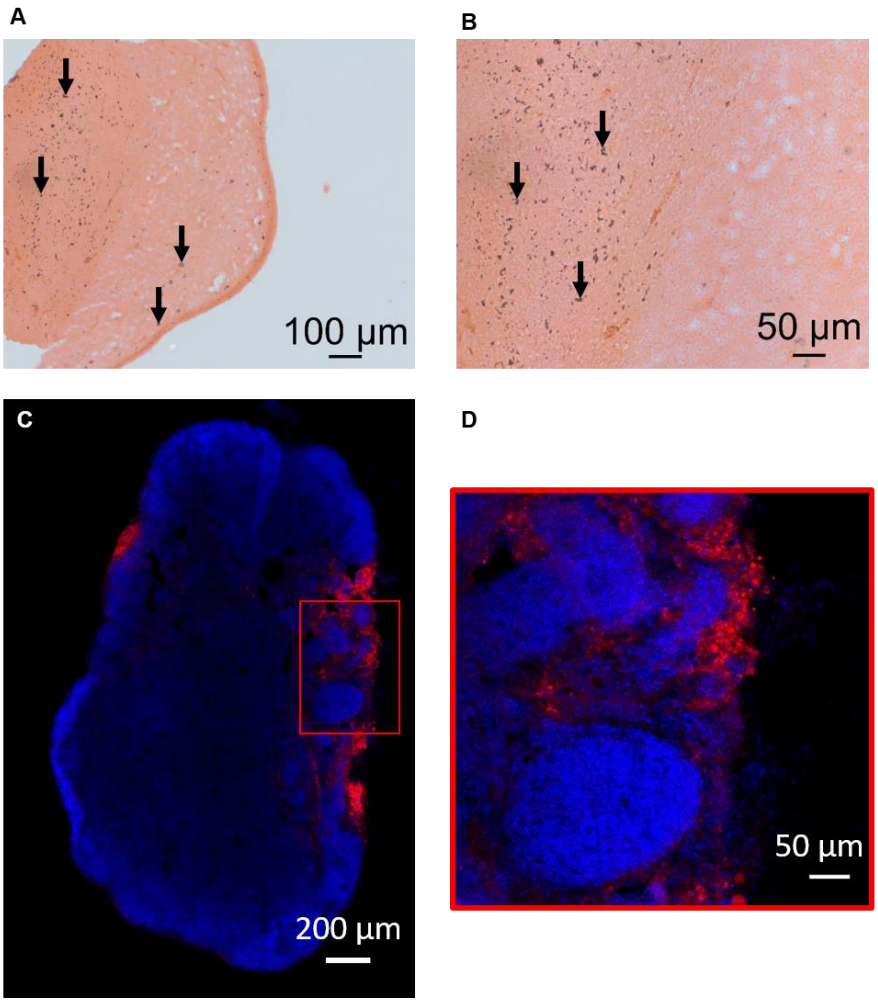

Figure 52. Histology of Dye950-nPLPs and DiI-nPLPs at 24 hours. Brighfield and confocal microscopy from the left inguinal lymph node from the mouse injected with Dye950-nPLPs (A, B) or DiI-nPLPs (C, D), respectively. Dye950-nPLPs may be indicated by dark green/brown speckles throughout the eosin-stained lymph node (A, B; black arrows). (C, D) DiI-nPLPs (red) were visible at the DAPI-stained lymph node periphery

5.4.3 In vivo studies using adjuvant-coated particles

To assess trafficking in a vaccine-mimicking particle, Dye950- and DiI-nPLPs were next coated with an adjuvant, CpG. BALB/c mice were similarly prepared and injected. In this case, US/PA imaging time points were staggered between mice to visualize trafficking over a longer range of time. The first mouse was imaged from 0 – 4

hours post-injection and at 48 hours post-injection. The second mouse was imaged from 4 – 8 hours post-injection and at 24 hours post-injection. To more fully evaluate trafficking of a vaccine-mimicking particle, two-dimensional (2D) and 3D multi-wavelength US/PA datasets were acquired over a wider field-of-view. However, system limitations allowed acquisition of fewer wavelengths for 3D datasets, which impacted spectroscopic processing. More specifically, compared to analysis of uncoated Dye950-nPLPs, which separated the PA signals into three absorber maps (Hb, HbO_2, and particles), the best approach to minimize artifacts for CpG-Dye950-nPLPs was to separate signals into two absorber maps (total blood and particles). Although this was only a requirement for 3D datasets, for consistency purposes, 2D datasets of adjuvant-coated particles were processed using the same approach, i.e. two absorber maps were produced. For this reason, some differences were observed in the 2D results of uncoated particles (Figure 50) and adjuvant-coated particles (Figure 53).

In this case, 2D cross-sectional views of the ipsilateral inguinal lymph node showed some crosstalk was between the CpG-Dye950-nPLPs and blood (Figure 53A and 53F), indicated by detection of CpG-Dye950-nPLPs before injection (Figure 53A). Thus, some misidentification of optical absorbers occurred. However, the map of CpG-Dye950-nPLP distribution before injection (Figure 53A) can be used to identify imaging artifacts at later time points (Figure 53B–E). In addition, artifacts were isolated to tissues outside of the lymph node. Thus, particle accumulation within the lymph node can still be assessed, and spectroscopic PA analysis was conducted with caution. For the adjuvant-coated particles, no PLP accumulation was observed at the lymph node by 24 or 48 hours post-injection (Figure 53B–E). Changes in blood spatial distribution were observed (Figure 53F–J).

Although this may be indicative of an immune response, the result can also be explained by acquisition of different imaging frames at each time point, as mice were anesthetized again for US/PA imaging at 24 hours and 48 hours post-injection. Ultrasound depicted some response to the particles as lymph node swelling was visible at 48 hours post-injection (Figure 53E), which was confirmed by photographs of harvested inguinal lymph nodes (Figure 53K). Swelling was suspected to primarily result from presence of the CpG adjuvant because US/PA images of the lymph node after injection of uncoated particles loaded with dye did not show the same response (Figure 50). Note that the injection site was not visible in any US/PA images in Figure 53.

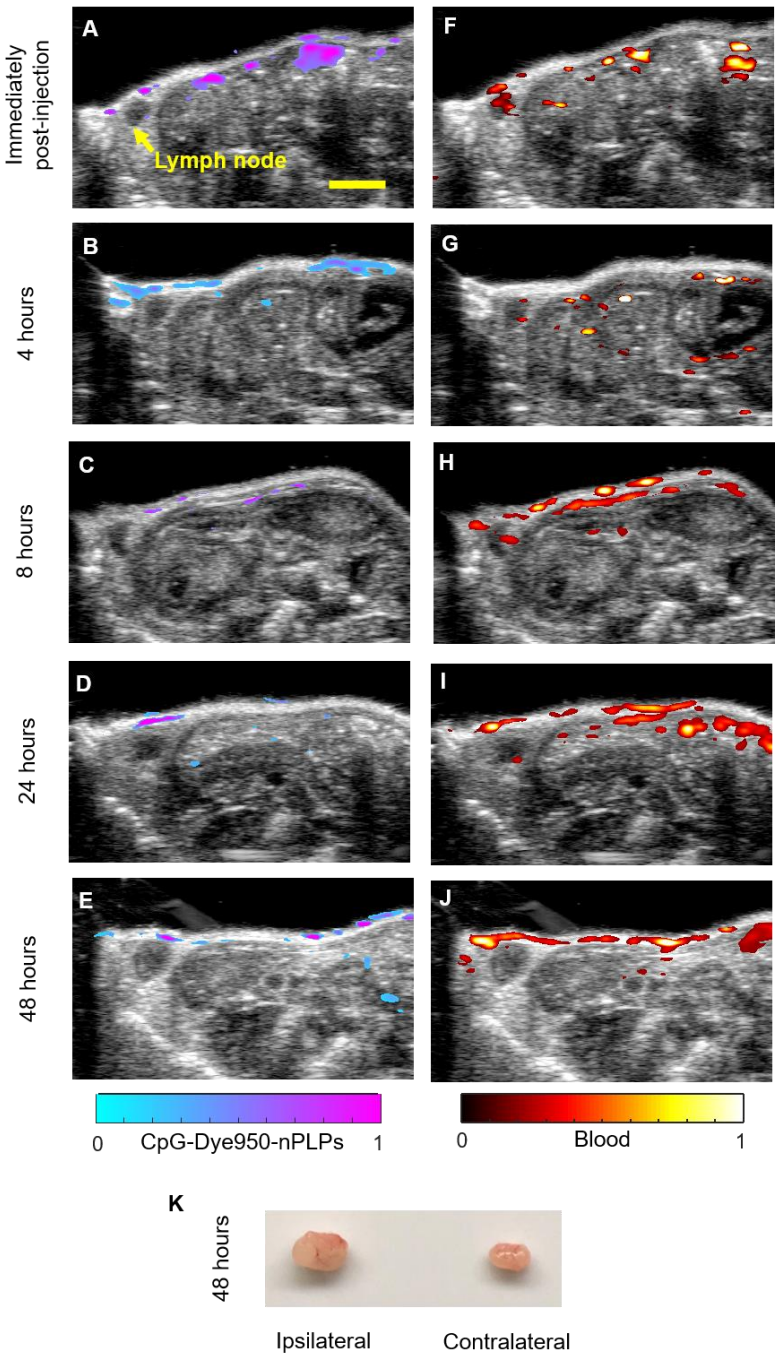

Figure 53. *In vivo* US/PA imaging of CpG-Dye950-nPLP trafficking to the lymph node. PA datasets were post-processed using spectroscopic analysis to distinguish absorbers: CpG-Dye950-nPLPs (A – E; left column) and blood (F – J; right column). Absorber distribution maps immediately (A, F), 4 hours (B, G), 8 hours (C, H), 24 hours (D, I), and 48 hours (E, J) after injection. (K) Photographs of excised lymph nodes. Scale bar = 3 mm.

To better understand results from 2D cross-sectional lymph node images, 3D multi-wavelength US/PA datasets were processed to depict CpG-Dye950-nPLP trafficking over a larger field-of-view from the injection site to the ipsilateral inguinal lymph node. After spectroscopic analysis, topographic maps were created by integrating spectroscopic PA datasets with depth (y-dimension) (Figure 54). Although crosstalk was again observed between the CpG-Dye950-nPLPs and blood (Figure 54A and 54F), this was localized to the injection site. Thus, insights can still be gained about particle trafficking since the location of the imaging artifacts was clearly identified and isolated to a specific region. Minimal changes in CpG-Dye950-nPLP distribution were observed up to 8 hours post-injection (Figure 54A–C). At 24 and 48 hours post-injection the size and shape of the injection footprint changed, indicating particle movement away from the injection site, and CpG-Dye950-nPLPs appeared in a branched pattern resembling vessels in surrounding tissue (Figure 54D and 54E). Thus, CpG-Dye950-nPLPs appeared trapped in vessels outside of the lymph node. However, the intertwined arrangement of blood and lymphatic vessels and shortcomings of the current processing techniques, prevents conclusions on whether particles are specifically trapped within the vasculature or lymphatics.

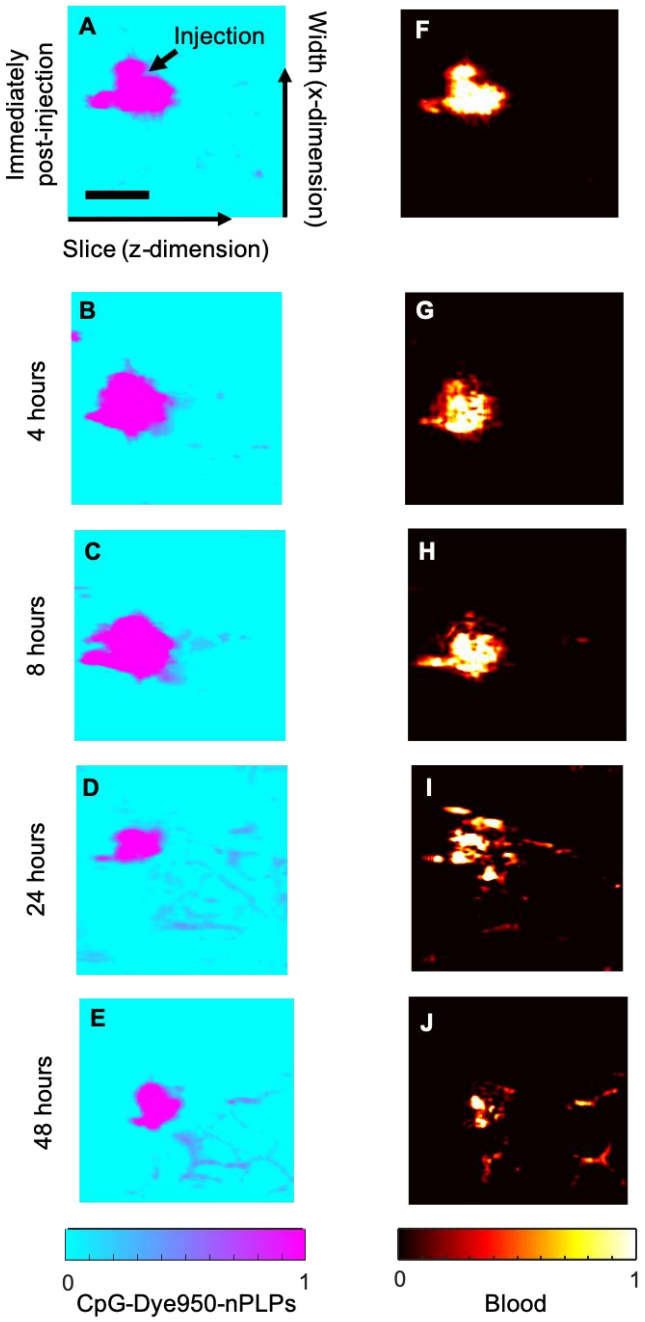

Figure 54. Topographic maps of absorbers from the injection site to the lymph node. Spectroscopic PA analysis of 3D volumetric datasets distinguished CpG-Dye950-nPLPs (A – E; left column) and blood (F – J; right column). Images were integrated over depth (y-dimension). Over time the size of the injection footprint decreased, and particles were distributed in a branched pattern extending from the injection site (B – E). Scale bar = 3 mm.

Three-dimensional volumetric US/PA overlay images of the CpG-Dye950-nPLPs provided additional anatomical context (Figure 55). Similar to topographic maps, the footprint of the injection site decreased from 4 hours to 48 hours post-injection, indicating particle trafficking away from the injection site. However, particles did not appear to be traveling towards the ipsilateral inguinal lymph node, located along the outer left edge of ultrasound images. CpG-Dye950-nPLPs were localized to superficial vessels extending towards the midline of the mouse (Figure 55C and 55D).

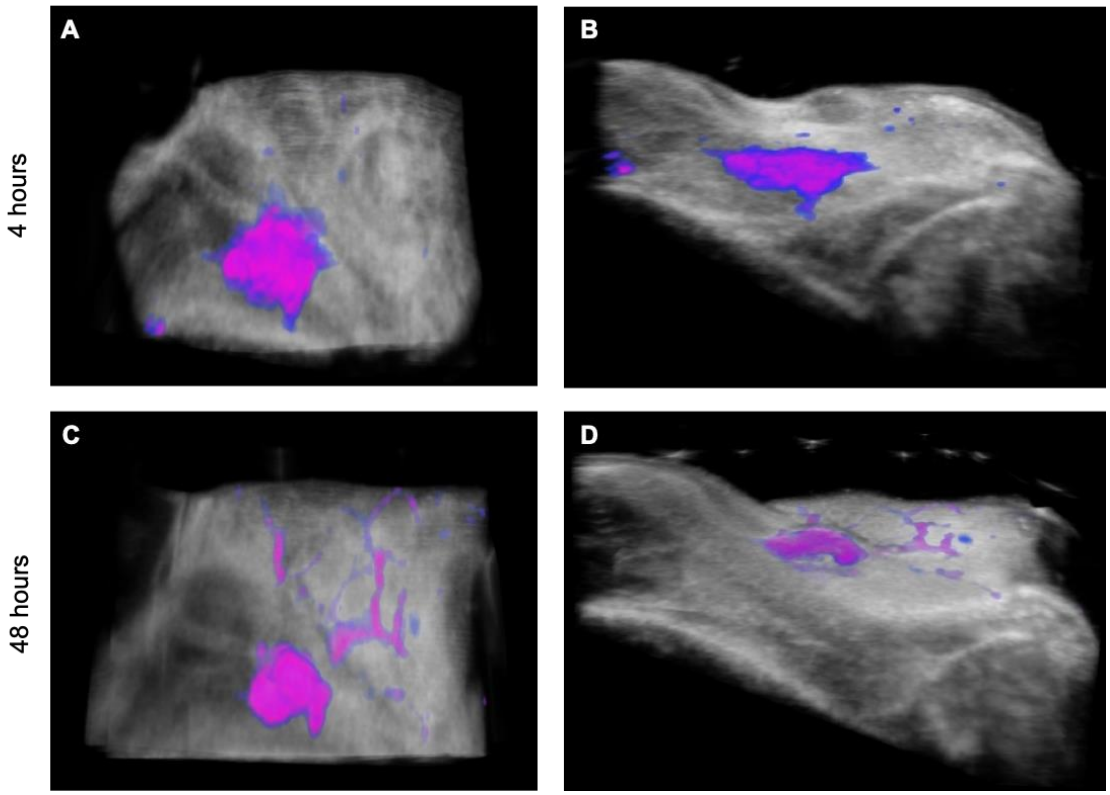

Figure 55. Three-dimensional volumetric images of CpG-Dye950-nPLP trafficking from the injection site. Ultrasound (grayscale) depicts anatomy and spectroscopic PA analysis (color scale) distinguished CpG-Dye950-nPLPs at 4 hours (A, B) and 48 hours (C, D) post-injection. The size of the injection site decreased by 48 hours post-injection and PLPs appeared to be in superficial vessels (C, D).

To again attempt to establish a ground truth for comparison of *in vivo* PA results, CpG-DiI-nPLP localization was assessed with fluorescent IVIS experiments at 24 hours post-injection. Particle accumulation was still not visible at the lymph node with *in vivo* fluorescent imaging using IVIS. However, some increase in fluorescent signal was visible in the abdomen (Figure 56A), which may indicate CpG-Dye950-nPLP accumulation in superficial vessels. However, considering the poor resolution of IVIS, this signal cannot be conclusively identified as being within the lymphatic or blood vessels. The mouse was sacrificed and fluorescent images were acquired *ex vivo* using IVIS by again cutting open the skin to expose both inguinal lymph nodes and covering the injection site. Fluorescent signal from CpG-DiI-nPLPs was visible at the ipsilateral lymph node, which indicates sensitivity of *in vivo* PA results can be improved. However, the best comparison to assess current advantages of the *in vivo* US/PA platform is *in vivo* fluorescent imaging using IVIS (Figure 56A). Unlike the US/PA platform, *in vivo* fluorescent imaging with IVIS did not visualize particle localization within superficial vessels or swelling at the lymph node and could not detect particles at the lymph node. With this in mind, improvements are needed with the US/PA platform to better track adjuvant-coated particles; however, there are already clear benefits compared to the most similar minimally invasive alternative, *in vivo* fluorescent imaging with IVIS, which failed to provide any information on particle localization and trafficking to the lymph node *in vivo*.

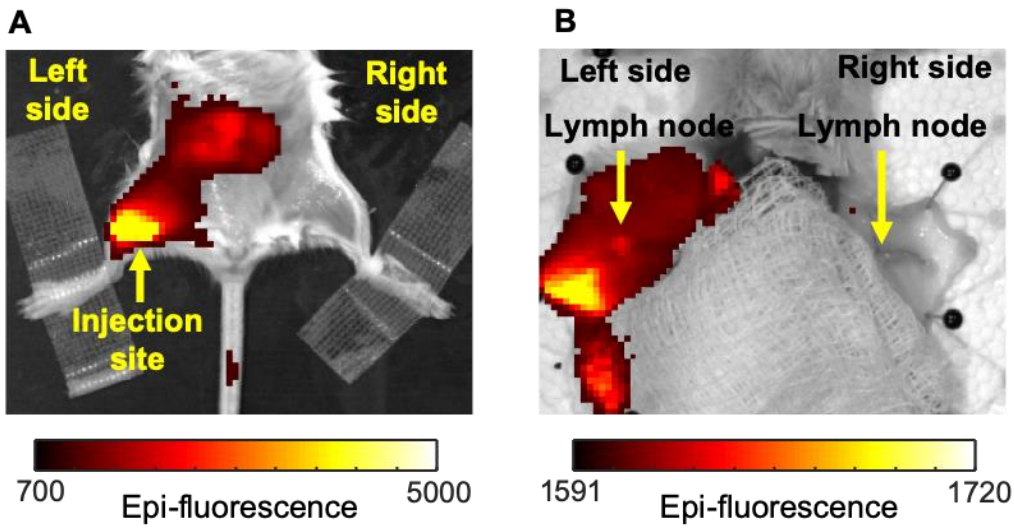

Figure 56. *In vivo* and *ex vivo* fluorescent imaging of CpG-DiI-nPLPs at 24 hours. Particle accumulation was not apparent at the left inguinal lymph node *in vivo* while the skin was intact (A). Increased fluorescent signal was present at the left inguinal lymph node *ex vivo* (B).

Both inguinal lymph nodes were again harvested for histology from both PA and fluorescent studies of adjuvant-coated particles at 24 hours post-injection. Eosin-stained tissue sections depicted CpG-Dye950-nPLPs throughout the lymph node, indicated by appearance of dark greenish/brown speckles (Figure 57A and 57B). Confocal fluorescent microscopy confirmed presence of CpG-DiI-nPLPs (red fluorescence) at the lymph node periphery (Figure 57C and 57D). Both sets of microscopy also indicated a need for increased imaging sensitivity of the US/PA platform. However, discrepancies remain as to whether the standard for US/PA sensitivity should be based on brightfield microscopy, confocal microscopy, or fluorescent imaging with IVIS, as each depicted differences in particle localization. Brightfield microscopy showed accumulation of CpG-Dye950-nPLPs throughout the lymph node. Confocal microscopy showed accumulation of CpG-DiI-nPLPs at the lymph node periphery only. *In vivo* IVIS showed no accumulation of

CpG-DiI-nPLPs at the lymph node. Thus, there are three different "ground truths." Overall, the best comparison is again *in vivo* fluorescent imaging with IVIS, but the current US/PA platform already outperforms this modality. Thus, the key question for future work is how to define the standards for the ideal US/PA platform for tracking particle *in vivo*. The best approach is to set standards based on quantification using histological analysis, but the target detection limit will need to be adjusted due to inherently lower sensitivity of minimally invasive, longitudinal monitoring methods.

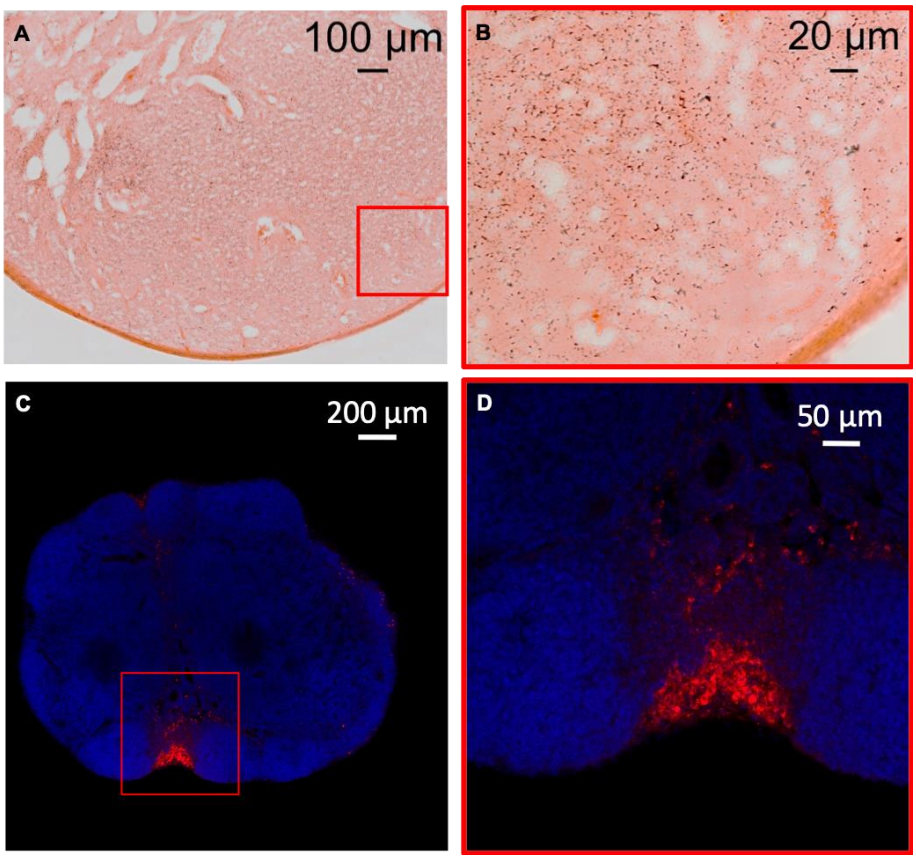

Figure 57. Histology of CpG-Dye950-nPLPs and CpG-DiI-nPLPs at 24 hours. Brighfield and confocal microscopy from the left inguinal lymph node from the mouse injected with CpG-Dye950-nPLPs (A, B) or CpG-DiI-nPLPs (C, D), respectively. CpG-Dye950-nPLPs may be indicated by dark green/brown speckles throughout the eosin-stained lymph node (A, B). (C, D) Some CpG-DiI-nPLPs (red) were visible at the periphery of the DAPI-stained lymph node.

5.5 Discussion

Our results demonstrated several beneficial features of the US/PA imaging platform. First, high resolution and greater penetration depth of US/PA imaging compared to purely optical methods allowed minimally invasive monitoring of particle localization, which was not possible with currently available fluorescent imaging methods, including IVIS. Second, particle trafficking to the lymph node could be longitudinally monitored with 2D cross-sectional images. Accompanying changes in blood spatial distribution and lymph node morphology were also detected. Lastly, 3D volumetric US/PA datasets depicted particles over a wide field-of-view from the injection site to the inguinal lymph node, which may help to further understand particle trafficking and cell-particle interactions.

Although two specific PA-tagged PLP formulations were ultimately used for *in vivo* studies, Dye950-nPLPs and CpG-Dye950-nPLPs, many other formulations were developed and assessed in tissue-mimicking phantom studies. Specifically, both m- and nPLPs were loaded with indocyanine green dye, copper sulfide nanoparticles, gold nanospheres, Prussian blue nanocubes, BODIPY dyes, croconic acid dyes, and infrared 1048 dye (Sigma-Aldrich). The key factor for encapsulation was use of a hydrophobic optical absorber. Dye950 and Dye750, commercially identified as Epolight 3832 and Epolight 9151, respectively, produced the highest PA signal at the lowest PLP concentration in phantom studies (.195 mg/ml). DiI was also a hydrophobic dye and was easily encapsulated in the PLPs for control experiments using fluorescent microscopy.

Although the same synthesis protocol was used for all particle types, differences in particle diameter and surface charge were observed based on the dye encapsulated. For

example, compared to uncoated, unloaded nPLPs, which had a hydrodynamic diameter of 277 nm, the DiI-nPLPs and Dye950-nPLPs measured ~301 nm and ~330 nm, respectively. Unloaded nPLPs and Dye950-nPLPs had similar surface charges of -31 +/- 5.73 mV and -34.3 +/- 5.83 mV, respectively. However, the DiI-nPLPs had a surface charge of -19.5 +/- 4.06 mV. After the final adjuvant coating step, the surface charge of CpG-Dye950-nPLPs and CpG-DiI-nPLP was 9.86 +/- 3.09 mV and -3.31 +/- 5.60 mV, respectively. These differences may impact trafficking to the lymph node,[58,201] which raises concerns for assessing the mechanism of action of a particular vaccine formulation as the dye itself may impact immune response.

In the case of the Dye950-nPLPs (uncoated), particles were detected at early time points and accumulation at the periphery of the left inguinal lymph node was observed by 24 hours post-injection. Furthermore, no crosstalk was observed between endogenous and exogenous absorbers prior to injection, which indicates correct identification of absorbers and gives confidence in PA detection at later time points. *In vivo* US/PA imaging results were compared to *in vivo* results using IVIS. Unlike *in vivo* US/PA imaging results, IVIS was unable to detect DiI-nPLPs *in vivo* at the left inguinal lymph node at 24 hours post-injection. Thus, mice were sacrificed and both inguinal lymph nodes were exposed by peeling back the skin to make another attempt at validating the US/PA platform. *Ex vivo* fluorescent results using IVIS showed DiI-nPLP accumulation at the left inguinal lymph node, which agreed with *in vivo* US/PA imaging results. However, poor image resolution of IVIS made it impossible to determine if DiI-nPLPs were localized only at the lymph node periphery, which was the case in PA results. These shortcomings of IVIS highlight clear advantages of the US/PA tool, specifically minimally invasive, high resolution, *in*

vivo longitudinal imaging. However, results also highlight the challenge of setting detection standards and establishing a ground truth for the US/PA imaging platform.

After sacrifice, lymph nodes were harvested for histology. Brightfield microscopy was used to visualize Dye950-nPLPs, which appeared dark green in solution. Confocal fluorescent microscopy was used to detect DiI-nPLPs. Fluorescent microscopy depicted the DiI-nPLPs at only the periphery of the lymph node and agreed with *in vivo* US/PA imaging results. However, brightfield microscopy showed Dye950-nPLP accumulation throughout the lymph node. Thus, brightfield microscopy seemed to indicate that PA image analysis techniques lacked sufficient sensitivity to detect all Dye950-nPLPs within the lymph node. However, although unlikely, the dark greenish/brown speckles observed from brightfield microscopy were faint and perhaps did not result from the Dye950-nPLPs. This again highlights the broader challenge of establishing an accurate ground truth for these studies. Although *ex vivo* IVIS or confocal microscopy images were less ambiguous and seem to be the most reasonable comparisons, a separate set of particles was required to incorporate a fluorescent dye, and the DiI-nPLPs were injected in a different mouse. Furthermore, the image resolution of IVIS and sensitivity of confocal fluorescent microscopy make detailed comparison with the US/PA platform somewhat invalid. To minimize variability in the ground truth, ideally one type of PLP would be synthesized that simultaneously encapsulates a fluorescent and PA absorber.

In vivo studies were repeated with adjuvant-coated particles. The addition of an adjuvant was a better representation of a vaccine particle, and further analysis was conducted to assess the US/PA platform. Thus, three-dimensional multi-wavelength US/PA datasets were acquired. However, due to hardware limitations, it was not possible

to acquire as many wavelengths, which in turn impacted spectroscopic analysis results. In this case, more crosstalk was observed between the CpG-Dye950-nPLPs and endogenous absorbers. In spite of this inaccuracy, artifacts were identifiable and allowed some insight to be gained regarding particle trafficking. However, improved processing techniques will be required. Three-dimensional US/PA images of CpG-Dye950-nPLPs showed particles were localized to surrounding vessels, possibly be indicative of the lymphatics, but were not visible at the lymph node. This type of information provides a direct example of how the US/PA platform may be used to help inform particle design. Without localization within the lymph node, a robust immune response to this formulation was unlikely.

5.6 Conclusions

Overall, the US/PA imaging platform has many advantages compared to existing technologies for monitoring vaccine particle trafficking to the lymph node, and some of the potential benefits were demonstrated in these studies. Dye950-nPLPs and CpG-Dye950-nPLPs, were synthesized and a variety of outcomes were monitored with US/PA imaging tools. US/PA imaging allowed longitudinal monitoring, high resolution anatomical imaging of the lymph node, and three-dimensional volumetric images provided more complete information on particle trafficking over a wide field-of-view. Changes in blood spatial distribution and lymph node morphology following particle injection were also detected. Together these pieces of information may provide valuable data to aid vaccine design. Overall, in its current state the *in vivo* US/PA platform for vaccine particle tracking already outperforms the most equivalent alternative technology, which is *in vivo* fluorescent imaging using IVIS. IVIS could not detect particles at the lymph node *in vivo,* whereas the US/PA platform did allow minimally invasive particle detection *in vivo*.

However, further development is required to develop the US/PA platform into a highly sensitive, turn-key tool for vaccine particle detection.

5.7 Future work

In its current state, results have shown enough beneficial features to motivate further development of the US/PA imaging platform for monitoring vaccine particles. However, many technical challenges were identified for future work.

Related to study design, a more accurate ground truth needs to be established. It was difficult to validate PA imaging results with the current strategy of injecting a second set of fluorescent particles in a separate mouse. Furthermore, inherent differences between US/PA imaging and fluorescent confocal microscopy or IVIS make it challenging to compare results and conclusively inform changes to the US/PA system. Ideally, the fluorescent and PA absorber should be incorporated within the same particle. Given the poor resolution and inability to detect particles at the lymph node *in vivo* using IVIS, confocal microscopy may be the better option for verification.

The greatest hurdles for future development is increasing PA imaging sensitivity and minimizing high background signals from endogenous absorbers. Further analysis and modifications to spectroscopic processing algorithms may lead to some improvement. Additional particle formulations using other photoacoustic absorbers may also be investigated. Although many other dyes and hydrophilic nanoparticles were tried in the current studies, another option would be to add hydrophobic coatings on nanoparticles, which was only briefly attempted.

However at this point a more drastic change may be required. Rather than continuing to investigate spectroscopic processing techniques, a switch to dynamic contrast mechanisms may be warranted. Dynamic contrast agents, which change in relation to a stationary background PA signals, can allow highly sensitive imaging and suppression of background signals,[205] which was clearly identified as a key requirement for detecting low concentrations of vaccine particles at the lymph node. The drawback of dynamic contrast agents is susceptibility to motion artifacts.

Outside of addressing these technical challenges, the broader vision for this project is to implement multiplex imaging, meaning simultaneous detection of many different photoabsorbers. The motivation from an immunotherapy perspective is that simultaneously delivering several different types of PLPs with different roles eliminates the need to design the one perfect particle to stimulate a holistic immune response. However, understanding the resulting outcome becomes more complex with more particles, even further affirming the need for longitudinal, minimally invasive, *in vivo* monitoring techniques. Thus, the US/PA imaging platform may ultimately be applied by tagging different types of PLPs with different absorbers for simultaneous monitoring.

5.8 Contributions from collaborators

In this chapter, specific contributions were made from Jardin Leleux, Randall Toy, Pallab Pradhan, and Diego Dumani. Jardin Lelux, Pallab Pradhan, and Randall Toy shared expertise and provided training on synthesis of the unloaded PLPs and CpG-coated PLPs. Diego Dumani shared his expertise and advice related to lymph node imaging.

CHAPTER 6. CONCLUSIONS

This thesis described development of a US/PA imaging toolbox, consisting of optically-absorbing contrast agents, imaging hardware, imaging protocols and algorithm development. Different individual tools were combined to create custom imaging platforms for tracking, which were applicable to a variety of *in vivo* applications: 1) stem cell tracking in the anterior segment and spinal cord; and 2) particle tracking for vaccine development. The US/PA imaging toolbox was assessed in three very different applications to demonstrate versatility and motivate later extension to other applications. Although each application was met with unique individual technical challenges, there were several common themes observed throughout all results, which lay the pathway for overall future research plans.

One major research endeavor should be implementation of functional imaging. In its current state, these platforms focused on providing information on location to assess stem cell delivery, retention, and migration. Knowing where the stem cells were located was a critical first step on the longer path of providing functional information. A variety of types of functional information can be provided, some of which were noted in developing the vaccine particle tracking platform, such as changes in blood accumulation or blood oxygen saturation at the lymph node. A metric like blood oxygen saturation would be relevant to a variety of applications, whether that be assessing disease state, tissue healing and revascularization, inflammatory response, or immune response.

Specific to the stem cell tracking applications investigated herein, a key piece of functional information is to determine stem cell status, which may include stem cell

proliferation, viability, or differentiation. In this case, photoacoustic nanosensors can address this need. Related to the spinal cord aim, we are already developing a photoacoustic probe to assess stem cell apoptosis induced by caspase-3. The same probe is relevant to ophthalmic applications. However, one drawback of the current detection scheme is stem cell apoptosis is indicated by an increase in PA signal. Changes in amplitude tend to be less reliable and sensitive than spectroscopic changes, i.e. amplitude may change due to variations in the imaging system itself. Another drawback is that the current probe only detects stem cell apoptosis; however, there are many other mechanisms and classifications of cell death, including entosis, mitotic catastrophe, necrosis, necroptosis, and pyroptosis.[206] Although detecting caspase-3-mediated stem cell apoptosis is a good starting point, a complete viability sensor should account for all mechanisms of cell death.

A second major research endeavor should be investigation of background-free photoacoustic imaging techniques, where PA signals from endogenous absorbers can be completely eliminated with confidence to improve detection sensitivity of cells or particles. This was a common theme throughout all applications. Herein, spectroscopic analysis was the primary method used for separating photoacoustic signals from endogenous and exogenous absorbers. The spinal cord represented the simplest image-processing scenario for several reasons: 1) minimal background signals were observed in the spinal cord; 2) the basic vicinity of the stem cell injection was known *a priori*; and 3) the spinal cord has a well-defined, consistent location. The eye represented a more difficult image-processing scenario. Extremely high background signals from melanin were present in the eye; however, similar to the spinal cord, imaging geometry and location of endogenous

absorbers was well-established. However, stem cell delivery location was not well-controlled in the eye as cells were injected into the aqueous humor and allowed to passively accumulate at the TM. Vaccine particle tracking at the lymph node represented the most challenging image-processing scenario. Vaccine particle trafficking combined challenges from the eye and spinal cord and also introduced some new issues: 1) high background signals were observed from endogenous absorbers; 2) imaging geometry was not consistent; 3) very low PA signals must be distinguished due to low particle accumulation at the lymph node; 4) particle delivery to the lymph node was uncertain; 5) there was no ideal ground truth. For these reasons, each application may benefit from custom light delivery systems or more sophisticated detection algorithms to facilitate background-free PA imaging techniques.

Custom focused-light delivery systems can minimize unnecessary irradiation of tissues outside of the region of interest. Thus, background signals from endogenous absorbers outside the region of interest will no longer be irradiated and, in turn, no longer produce PA signals. However, this approach may not be feasible depending on the application. Focused-light delivery is particularly relevant for ophthalmic applications of PA imaging. From a clinical perspective, focused light delivery systems improve patient safety, imaging accuracy, and ultimately facilitate translation. However during the developmental phase, irradiating the entire anterior segment is important for visualizing off-target stem cell delivery. In the case of lymph node imaging, focusing light at one specific lymph node may be useful to assess particle accumulation at the lymph node with high sensitivity; however, it is again not an ideal approach for visualizing particle trafficking through the lymphatics, which cover a wide field-of-view.

An alternative is implementing background-free PA imaging techniques. These techniques utilize dynamic contrast agents that repeatedly change state. Examples include magnetomotive ultrasound or photoacoustic imaging, pump-probe techniques, or phase-change agents.[192,199,207,208] Magnetomotive imaging requires use of magnetic contrast agents, like PBNCs. By cycling a magnetic field on and off, magnetically-tagged cells or particles oscillate and the background remains stationary. This magnetic movement causes changes in the speckle pattern of US/PA datasets for highly-sensitive imaging at increased imaging depths.[192,207] Pump-probe contrast agents, such as Rose Bengal dye, generate PA signals at one wavelength, but only after first being activated at a different wavelength.[208] Phase-change contrast agents use a similar strategy by oscillating between on/off states to create "blinking" contrast upon acoustic or optical activation.[199,209] These more sophisticated contrast mechanisms may greatly improve sensitivity and imaging depth, which is a benefit for any application of the US/PA imaging toolbox developed here.

Finally, therapeutic tools can be added to the US/PA imaging toolbox. The entire purpose of the US/PA toolbox developed here was to inform therapy design, aid development, and expedite clinical translation. Thus, therapeutic strategies should be implemented in addition to monitoring. One example was the use of PBNCs for image-guided magnetic delivery. Other opportunities include therapeutic heating, laser-triggered therapeutic delivery, nanoparticle-induced electrical stimulation, and many others. Overall, the current work demonstrated a variety of benefits and successes of the US/PA imaging toolbox for tracking cells and particles *in vivo*, and results lay the groundwork to create theranostic platforms in the future.

REFERENCES

1. Schroeder, T. Imaging stem-cell-driven regeneration in mammals. *Nature* **453**, 345–351 (2008).

2. Nam, S. Y., Ricles, L. M., Suggs, L. J. & Emelianov, S. Y. Imaging Strategies for Tissue Engineering Applications. *Tissue Eng. Part B. Rev.* **21**, 1–44 (2014).

3. Santiesteban, D. Y. *et al.* Monitoring/Imaging and Regenerative Agents for Enhancing Tissue Engineering Characterization and Therapies. *Ann. Biomed. Eng.* **44**, 750–772 (2016).

4. Hoehn, M. *et al.* Monitoring of implanted stem cell migration in vivo: A highly resolved in vivo magnetic resonance imaging investigation of experimental stroke in rat. *Proc. Natl. Acad. Sci. U. S. A.* **99**, 16267–16272 (2002).

5. Lamanna, J. J. *et al.* Magnetic Resonance Imaging-Guided Transplantation of Neural Stem Cells into the Porcine Spinal Cord. *Stereotact. Funct. Neurosurg.* **95**, 60–68 (2017).

6. Kraitchman, D. L. *et al.* In vivo magnetic resonance imaging of mesenchymal stem cells in myocardial infarction. *Circulation* **107**, 2290–3 (2003).

7. Geuze, R. E. *et al.* Luciferase Labeling for Multipotent Stromal Cell Tracking in Spinal Fusion Versus Ectopic Bone Tissue Engineering in Mice and Rats. *Tissue Eng. Part A* **16**, 3343–3351 (2010).

8. Vilalta, M. *et al.* Dual luciferase labelling for non-invasive bioluminescence imaging of mesenchymal stromal cell chondrogenic differentiation in demineralized bone matrix scaffolds. *Biomaterials* **30**, 4986–4995 (2009).

9. Kim, T. *et al.* In Vivo Micro-CT Imaging of Human Mesenchymal Stem Cells Labeled with Gold-Poly- <scp>l</scp> -Lysine Nanocomplexes. *Adv. Funct. Mater.* **27**, 1604213 (2017).

10. Meir, R. *et al.* Nanomedicine for Cancer Immunotherapy: Tracking Cancer-Specific T-Cells *in Vivo* with Gold Nanoparticles and CT Imaging. *ACS Nano* **9**, 6363–6372 (2015).

11. Bartunek, J. *et al.* Intracoronary injection of CD133-positive enriched bone marrow progenitor cells promotes cardiac recovery after recent myocardial infarction: Feasibility and safety. *Circulation* **112**, (2005).

12. Mallidi, S., Luke, G. P. & Emelianov, S. Photoacoustic imaging in cancer detection, diagnosis, and treatment guidance. *Trends Biotechnol.* **29**, 213–221 (2011).

13. Emelianov, S. Y., Li, P.-C. & O'Donnell, M. Photoacoustics for molecular imaging and therapy. *Phys. Today* **62**, 34–39 (2009).

14. Wang, L. V & Hu, S. Photoacoustic tomography: in vivo imaging from organelles to organs. *Science* **335**, 1458–62 (2012).

15. Luke, G. P., Yeager, D. & Emelianov, S. Y. Biomedical Applications of Photoacoustic Imaging with Exogenous Contrast Agents. *Ann. Biomed. Eng.* **40**, 422–437 (2012).

16. Ricles, L. M. Investigating Mesenchymal Stem Cell Therapy for Ischemic Repair. *UT Diss.* (2014).

17. Nam, S. Y., Ricles, L. M., Suggs, L. J. & Emelianov, S. Y. In vivo Ultrasound and Photoacoustic Monitoring of Mesenchymal Stem Cells Labeled with Gold Nanotracers. *PLoS One* **7**, e37267 (2012).

18. Jokerst, J. V, Thangaraj, M., Kempen, P. J., Sinclair, R. & Gambhir, S. S. Photoacoustic Imaging of Mesenchymal Stem Cells in Living Mice via Silica-Coated Gold Nanorods. *ACS Nano* **6**, 5920–5930 (2012).

19. Sarvazyan, A. P., Rudenko, O. V, Swanson, S. D., Fowlkes, J. B. & Emelianov, S. Y. Shear wave elasticity imaging: a new ultrasonic technology of medical diagnostics.

20. Wang, L. V & Hu, S. Photoacoustic Tomography: In Vivo Imaging from Organelles to Organs. *Science (80-.).* **335**, 1458–1462 (2012).

21. Zhang, Y. S. *et al.* Labeling human mesenchymal stem cells with gold nanocages for in vitro and in vivo tracking by two-photon microscopy and photoacoustic microscopy. *Theranostics* **3**, 532–543 (2013).

22. Luke, G. P. *et al.* Silica-coated gold nanoplates as stable photoacoustic contrast agents for sentinel lymph node imaging. *Nanotechnology* **24**, 455101 (2013).

23. Chen, Y. S. *et al.* Silica-coated gold nanorods as photoacoustic signal nanoamplifiers. *Nano Lett.* **11**, 348–354 (2011).

24. Kubelick, K., Snider, E., Yoon, H., Ethier, C. R. & Emelianov, S. Y. Ultrasound and photoacoustic imaging to monitor ocular stem cell delivery and tissue regeneration (Conference Presentation). in (eds. Oraevsky, A. A. & Wang, L. V.) **10064**, 100640K (International Society for Optics and Photonics, 2017).

25. Gao, Y. *et al.* Controlled Synthesis of Multilayered Gold Nanoshells for Enhanced Photothermal Therapy and SERS Detection. *Small* n/a-n/a (2014). doi:10.1002/smll.201402149

26. Xie, J., Lee, S. & Chen, X. Nanoparticle-based theranostic agents. *Adv. Drug Deliv.*

Rev. **62**, 1064–1079 (2010).

27. Luke, G. P., Nam, S. Y. & Emelianov, S. Y. Optical wavelength selection for improved spectroscopic photoacoustic imaging. *Photoacoustics* **1**, 36–42 (2013).

28. Nam, S. Y. Ultrasound and Photoacoustic Imaging to Monitor Stem Cells for Tissue Regeneration. *UT Diss.* (2014).

29. Kamkaew, A. *et al.* BODIPY dyes in photodynamic therapy. *Chem. Soc. Rev.* **42**, 77–88 (2013).

30. Quigley, H. A. & Broman, A. T. The number of people with glaucoma worldwide in 2010 and 2020. *Br. J. Ophthalmol.* **90**, 262–7 (2006).

31. Alvarado, J., Murphy, C. & Juster, R. Trabecular meshwork cellularity in primary open-angle glaucoma and nonglaucomatous normals. *Ophthalmology* **91**, 564–79 (1984).

32. Alvarado, J., Polansky, J., Murphey, C. & Juster, R. Age-related changes in trabecular meshwork cellularity. *Investig. Ophthalmol. Vis. Sci.* **21**, 714 (1981).

33. Liton, P. B., Liu, X., Challa, P., Epstein, D. L. & Gonzalez, P. Induction of TGF-beta1 in the trabecular meshwork under cyclic mechanical stress. *J. Cell. Physiol.* **205**, 364–71 (2005).

34. Zhu, W. *et al.* Transplantation of iPSC-derived TM cells rescues glaucoma phenotypes in vivo. *Proc. Natl. Acad. Sci. U. S. A.* **113**, E3492-500 (2016).

35. Abu-Hassan, D. W., Li, X., Ryan, E. I., Acott, T. S. & Kelley, M. J. Induced pluripotent stem cells restore function in a human cell loss model of open-angle glaucoma. *Stem Cells* **33**, 751–61 (2015).

36. Manuguerra-Gagné, R. *et al.* Transplantation of Mesenchymal Stem Cells Promotes Tissue Regeneration in a Glaucoma Model Through Laser-Induced Paracrine Factor Secretion and Progenitor Cell Recruitment. *Stem Cells* **31**, 1136–1148 (2013).

37. Roubeix, C. *et al.* Intraocular pressure reduction and neuroprotection conferred by bone marrow-derived mesenchymal stem cells in an animal model of glaucoma. *Stem Cell Res. Ther.* **6**, 177 (2015).

38. Fercher, A. F., Drexler, W., Hitzenberger, C. K. & Lasser, T. Optical coherence tomography - principles and applications. *Reports Prog. Phys.* **66**, 239–303 (2003).

39. Schuman, J. S. *et al.* Optical coherence tomography: a new tool for glaucoma diagnosis. *Curr. Opin. Ophthalmol.* **6**, 89–95 (1995).

40. Hu, S., Rao, B., Maslov, K. & Wang, L. V. Label-free photoacoustic ophthalmic angiography. *Opt. Lett.* **35**, 1 (2010).

41. Silverman, R. H. *et al.* High-resolution photoacoustic imaging of ocular tissues. *Ultrasound Med. Biol.* **36**, 733–42 (2010).

42. Konstantopoulos, A., Hossain, P. & Anderson, D. F. Recent advances in ophthalmic anterior segment imaging: a new era for ophthalmic diagnosis? *Br. J. Ophthalmol.* **91**, 551–7 (2007).

43. Donnelly, E. M., Lamanna, J. & Boulis, N. M. Stem cell therapy for the spinal cord. *Stem Cell Res. Ther.* **3**, 24 (2012).

44. Glass, J. D. *et al.* Lumbar Intraspinal Injection of Neural Stem Cells in Patients with Amyotrophic Lateral Sclerosis: Results of a Phase I Trial in 12 Patients. *Stem Cells* **30**, 1144–1151 (2012).

45. Feldman, E. L. *et al.* Intraspinal neural stem cell transplantation in amyotrophic lateral sclerosis: Phase 1 trial outcomes. *Ann. Neurol.* **75**, 363–373 (2014).

46. Lamanna, J. J., Miller, J. H., Riley, J. P., Hurtig, C. V & Boulis, N. M. Cellular therapeutics delivery to the spinal cord: technical considerations for clinical application. *Ther. Deliv.* **4**, 1397–1410 (2013).

47. Riley, J. *et al.* Intraspinal Stem Cell Transplantation in Amyotrophic Lateral Sclerosis. *Neurosurgery* **74**, 77–87 (2014).

48. Wang, X., Pang, Y., Ku, G., Stoica, G. & Wang, L. V. Three-dimensional laser-induced photoacoustic tomography of mouse brain with the skin and skull intact. *Opt. Lett.* **28**, 1739 (2003).

49. Wu, W., Wang, P., Cheng, J.-X. & Xu, X.-M. Assessment of White Matter Loss Using Bond-Selective Photoacoustic Imaging in a Rat Model of Contusive Spinal Cord Injury. *J. Neurotrauma* **31**, 1998–2002 (2014).

50. Guzman, R. *et al.* Long-term monitoring of transplanted human neural stem cells in developmental and pathological contexts with MRI. *Proc. Natl. Acad. Sci. U. S. A.* **104**, 10211–10216 (2007).

51. Lamanna, J. J. *et al.* Ferumoxytol Labeling of Human Neural Progenitor Cells for Diagnostic Cellular Tracking in the Porcine Spinal Cord with Magnetic Resonance Imaging. *Stem Cells Transl. Med.* **6**, 139–150 (2017).

52. Bulte, J. W. M. *et al.* Neurotransplantation of magnetically labeled oligodendrocyte progenitors: Magnetic resonance tracking of cell migration and myelination. *Proc. Natl. Acad. Sci.* **96**, 15256–15261 (1999).

53. Nam, S. Y., Ricles, L. M., Suggs, L. J. & Emelianov, S. Y. In vivo ultrasound and photoacoustic monitoring of mesenchymal stem cells labeled with gold nanotracers. *PLoS One* **7**, 1–9 (2012).

54. Leleux, J. A., Pradhan, P. & Roy, K. Biophysical Attributes of CpG Presentation Control TLR9 Signaling to Differentially Polarize Systemic Immune Responses. *Cell Rep.* **18**, 700–710 (2017).

55. Pradhan, P. *et al.* The effect of combined IL10 siRNA and CpG ODN as pathogen-mimicking microparticles on Th1/Th2 cytokine balance in dendritic cells and protective immunity against B cell lymphoma. *Biomaterials* **35**, 5491–5504 (2014).

56. Pai Kasturi, S. *et al.* Prophylactic anti-tumor effects in a B cell lymphoma model with DNA vaccines delivered on polyethylenimine (PEI) functionalized PLGA microparticles. *J. Control. Release* **113**, 261–270 (2006).

57. Kasturi, S. P., Sachaphibulkij, K. & Roy, K. Covalent conjugation of polyethyleneimine on biodegradable microparticles for delivery of plasmid DNA vaccines. *Biomaterials* **26**, 6375–6385 (2005).

58. Leleux, J. & Roy, K. Micro and Nanoparticle-Based Delivery Systems for Vaccine Immunotherapy: An Immunological and Materials Perspective. *Adv. Healthc. Mater.* **2**, 72–94 (2013).

59. Leleux, J., Atalis, A. & Roy, K. Engineering immunity: Modulating dendritic cell subsets and lymph node response to direct immune-polarization and vaccine efficacy. *J. Control. Release* **219**, 610–621 (2015).

60. Germain, R. N., Robey, E. A. & Cahalan, M. D. A decade of imaging cellular motility and interaction dynamics in the immune system. *Science* **336**, 1676–81 (2012).

61. Germain, R. N., Miller, M. J., Dustin, M. L. & Nussenzweig, M. C. Dynamic imaging of the immune system: progress, pitfalls and promise. *Nat. Rev. Immunol.* **6**, 497–507 (2006).

62. Luke, G. P., Myers, J. N., Emelianov, S. Y. & Sokolov, K. V. Sentinel lymph node biopsy revisited: ultrasound-guided photoacoustic detection of micrometastases using molecularly targeted plasmonic nanosensors. *Cancer Res.* **74**, 5397–408 (2014).

63. Homan, K. a. *et al.* Silver nanoplate contrast agents for in vivo molecular photoacoustic imaging. *ACS Nano* **6**, 641–650 (2012).

64. Luke, G. P. & Emelianov, S. Y. Label-free Detection of Lymph Node Metastases with US-guided Functional Photoacoustic Imaging. *Radiology* **277**, 435–442 (2015).

65. Sun, I.-C., Dumani, D. & Emelianov, S. Y. Ultrasound-guided photoacoustic imaging of lymph nodes with biocompatible gold nanoparticles as a novel contrast agent (Conference Presentation). in (eds. Osiński, M., Parak, W. J. & Liang, X.-J.) **10078**, 100780E (International Society for Optics and Photonics, 2017).

66. Ramos, J. L. B., Li, Y. & Huang, D. Clinical and research applications of anterior segment optical coherence tomography - a review. *Clin. Experiment. Ophthalmol.* **37**, 81–89 (2009).

67. Zysk, A. M., Nguyen, F. T., Oldenburg, A. L., Marks, D. L. & Boppart, S. A. Optical coherence tomography: a review of clinical development from bench to bedside. *J. Biomed. Opt.* **12**, 051403 (2007).

68. Bianciotto, C. *et al.* Assessment of Anterior Segment Tumors with Ultrasound Biomicroscopy versus Anterior Segment Optical Coherence Tomography in 200 Cases. *Ophthalmology* **118**, 1297–1302 (2011).

69. Dada, T. *et al.* Comparison of anterior segment optical coherence tomography and ultrasound biomicroscopy for assessment of the anterior segment. *J. Cataract Refract. Surg.* **33**, 837–840 (2007).

70. Radhakrishnan, S. *et al.* Comparison of Optical Coherence Tomography and Ultrasound Biomicroscopy for Detection of Narrow Anterior Chamber Angles. *Arch. Ophthalmol.* **123**, 1053 (2005).

71. Huang, D. *et al.* Optical coherence tomography. *Science* **254**, 1178–81 (1991).

72. Hee, M. R. *et al.* Optical Coherence Tomography of the Human Retina. *Arch. Ophthalmol.* **113**, 325 (1995).

73. Swanson, E. A. *et al.* In vivo retinal imaging by optical coherence tomography. *Opt. Lett.* **18**, 1864 (1993).

74. Pavlin, C. J., Harasiewicz, K., Sherar, M. D. & Foster, F. S. Clinical Use of Ultrasound Biomicroscopy. *Ophthalmology* **98**, 287–295 (1991).

75. Konstantopoulos, A., Hossain, P. & Anderson, D. F. Recent advances in ophthalmic anterior segment imaging: a new era for ophthalmic diagnosis? *Br. J. Ophthalmol.* **91**, 551–7 (2007).

76. Radhakrishnan, S. *et al.* Real-Time Optical Coherence Tomography of the Anterior Segment at 1310 nm. *Arch. Ophthalmol.* **119**, 1179–1185 (2001).

77. Cense, B., Chen, T. C., Park, B. H., Pierce, M. C. & de Boer, J. F. Thickness and Birefringence of Healthy Retinal Nerve Fiber Layer Tissue Measured with Polarization-Sensitive Optical Coherence Tomography. *Investig. Opthalmology Vis. Sci.* **45**, 2606 (2004).

78. Grulkowski, I. *et al.* Retinal, anterior segment and full eye imaging using ultrahigh speed swept source OCT with vertical-cavity surface emitting lasers. *Biomed. Opt. Express* **3**, 2733 (2012).

79. Potsaid, B. *et al.* Ultrahigh speed 1050nm swept source / Fourier domain OCT

retinal and anterior segment imaging at 100,000 to 400,000 axial scans per second. *Opt. Express* **18**, 20029 (2010).

80. Diebold, Y. & Calonge, M. Applications of nanoparticles in ophthalmology. *Prog. Retin. Eye Res.* **29**, 596–609 (2010).

81. Boppart, S. A., Oldenburg, A. L., Xu, C. & Marks, D. L. Optical probes and techniques for molecular contrast enhancement in coherence imaging. *J. Biomed. Opt.* **10**, 041208 (2005).

82. Oldenburg, A. L. *et al.* Molecular Optical Coherence Tomography Contrast Enhancement and Imaging 47. doi:10.1007/978-3-319-06419-2_48

83. Manapuram, R. K. *et al.* In vivo estimation of elastic wave parameters using phase-stabilized swept source optical coherence elastography. *J. Biomed. Opt.* **17**, 1005011 (2012).

84. Mehrmohammadi, M., Oh, J., Mallidi, S. & Emelianov, S. Y. Pulsed magneto-motive ultrasound imaging using ultrasmall magnetic nanoprobes. *Mol. Imaging* **10**, 102–10 (2011).

85. Lapierre-Landry, M., Gordon, A. Y., Penn, J. S. & Skala, M. C. In vivo photothermal optical coherence tomography of endogenous and exogenous contrast agents in the eye. *Sci. Rep.* **7**, 9228 (2017).

86. Lapierre-Landry, M. *et al.* Imaging Melanin Distribution in the Zebrafish Retina Using Photothermal Optical Coherence Tomography. *Transl. Vis. Sci. Technol.* **7**, 4 (2018).

87. Lapierre-Landry, M., Connor, T. B., Carroll, J., Tao, Y. K. & Skala, M. C. Photothermal optical coherence tomography of indocyanine green in ex vivo eyes. *Opt. Lett.* **43**, 2470 (2018).

88. Lapierre-Landry, M., Gordon, A. Y., Penn, J. S., Skala, M. C. & Skala, M. C. In vivo Photothermal Optical Coherence Tomography of Gold Nanorods in the Mouse Eye. in *Optics in the Life Sciences Congress* BoM3A.2 (OSA, 2017). doi:10.1364/BODA.2017.BoM3A.2

89. Bell, A. G. LXVIII. Upon the production of sound by radiant energy. *London, Edinburgh, Dublin Philos. Mag. J. Sci.* **11**, 510–528 (1881).

90. Xu, M. & Wang, L. V. Photoacoustic imaging in biomedicine. *Rev. Sci. Instrum.* **77**, 041101 (2006).

91. Luke, G. P., Yeager, D. & Emelianov, S. Y. Biomedical Applications of Photoacoustic Imaging with Exogenous Contrast Agents. *Ann. Biomed. Eng.* **40**, 422–437 (2012).

92. Pavlin, C. J., Harasiewicz, K. & Foster, F. S. Ultrasound biomicroscopy of anterior segment structures in normal and glaucomatous eyes. *Am J Ophthalmol* **113**, 381–389 (1992).

93. Jiao, S. *et al.* Photoacoustic ophthalmoscopy for in vivo retinal imaging. *Opt. Express* **18**, 3967 (2010).

94. Song, W. *et al.* Integrating photoacoustic ophthalmoscopy with scanning laser ophthalmoscopy, optical coherence tomography, and fluorescein angiography for a multimodal retinal imaging platform. *J. Biomed. Opt.* **17**, 061206 (2012).

95. Bayer, C. L. *et al.* Multiplex photoacoustic molecular imaging using targeted silica-coated gold nanorods. *Biomed. Opt. Express* **2**, 1828 (2011).

96. Homan, K. *et al.* Silver nanosystems for photoacoustic imaging and image-guided therapy. *J. Biomed. Opt.* **15**, 021316 (2015).

97. Su, J., Karpiouk, A., Wang, B. & Emelianov, S. Photoacoustic imaging of clinical metal needles in tissue. *J. Biomed. Opt.* **15**, 021309 (2010).

98. Silverman, R. H. *et al.* High-Resolution Photoacoustic Imaging of Ocular Tissues. *Ultrasound Med. Biol.* **36**, 733–742 (2010).

99. Nam, S. Y. & Emelianov, S. Y. Array-Based Real-Time Ultrasound and Photoacoustic Ocular Imaging. *J. Opt. Soc. Korea* **18**, 151–155 (2014).

100. de la Zerda, A. *et al.* Photoacoustic ocular imaging. *Opt. Lett.* **35**, 270 (2010).

101. Maslov, K., Zhang, H. F. & Wang, L. V. Effects of wavelength-dependent fluence attenuation on the noninvasive photoacoustic imaging of hemoglobin oxygen saturation in subcutaneous vasculature in vivo. *Inverse Probl.* **23**, S113 (2007).

102. Sturm, R. A. & Larsson, M. Genetics of human iris colour and patterns. *Pigment Cell Melanoma Res.* **22**, 544–62 (2009).

103. Imesch, P. D., Wallow, I. H. L. & Albert, D. M. The color of the human eye: A review of morphologic correlates and of some conditions that affect iridial pigmentation. *Surv. Ophthalmol.* **41**, S117–S123 (1997).

104. Snider, E. J., Vannatta, R. T., Schildmeyer, L., Stamer, W. D. & Ethier, C. R. Characterizing differences between MSCs and TM cells: Toward autologous stem cell therapies for the glaucomatous trabecular meshwork. *J. Tissue Eng. Regen. Med.* **12**, 695–704 (2018).

105. Abu-Hassan, D. W., Li, X., Ryan, E. I., Acott, T. S. & Kelley, M. J. Induced Pluripotent Stem Cells Restore Function in a Human Cell Loss Model of Open-Angle Glaucoma. *Stem Cells* **33**, 751–761 (2015).

106. Jacques, S. L. Optical properties of biological tissues: a review. *Phys. Med. Biol.* **58**, R37-61 (2013).

107. Jacques, S. L., Glickman, R. D. & Schwartz, J. A. Internal absorption coefficient and threshold for pulsed laser disruption of melanosomes isolated from retinal pigment epithelium. in (ed. Jacques, S. L.) **2681**, 468 (International Society for Optics and Photonics, 1996).

108. Jacques, S. L. & McAuliffe, D. J. The melanosome: threshold temperature for explosive vaporization and internal absorption coefficient during pulsed laser irradiation. *Photochem. Photobiol.* **53**, 769–775 (1991).

109. Moaveni, M. K. A Multiple Scattering Field Theory Applied to Whole Blood. *Ph.D. Diss. Dept. Electr. Eng. Univ. Washingt.* (1970).

110. Schmitt, J. M. Optical Measurement of Blood Oxygenation by Implantable Telemetry. *Tech. Rep. G5558-15, Stanford*

111. Takatani, S. & Graham, M. D. Theoretical Analysis of Diffuse Reflectance from a Two-Layer Tissue Model. *IEEE Trans. Biomed. Eng.* **BME-26**, 656–664 (1979).

112. Scott Prahl. Optical Absorption of Hemoglobin. (1999). Available at: https://omlc.org/spectra/hemoglobin/index.html. (Accessed: 11th July 2018)

113. Porter, K. M., Epstein, D. L. & Liton, P. B. Up-Regulated Expression of Extracellular Matrix Remodeling Genes in Phagocytically Challenged Trabecular Meshwork Cells. *PLoS One* **7**, e34792 (2012).

114. Epstein, D. L., Freddo, T. F., Anderson, P. J., Patterson, M. M. & Bassett-Chu, S. Experimental obstruction to aqueous outflow by pigment particles in living monkeys. *Invest. Ophthalmol. Vis. Sci.* **27**, 387–395 (1986).

115. Bowen, T., Nasoni, R. L., Pifer, A. E. & Sembroski, G. H. Some Experimental Results on the Thermoacoustic Imaging of Tissue Equivalent Phantom Materials. in *1981 Ultrasonics Symposium* 823–827 (IEEE, 1981). doi:10.1109/ULTSYM.1981.197738

116. Kruger, R. A. & Liu, P. Photoacoustic ultrasound: Pulse production and detection in 0.5% Liposyn. *Med. Phys.* **21**, 1179–1184 (1994).

117. Oraevsky, A. A., Esenaliev, R. O., Jacques, S. L. & Tittel, F. K. Laser-based optoacoustic imaging in biological tissues. in *Laser-Tissue Interaction V; and Ultraviolet Radiation Hazards* **2134**, 16 (SPIE, 1994).

118. Cox, B., Laufer, J. G., Arridge, S. R. & Beard, P. C. Quantitative spectroscopic photoacoustic imaging: a review. *J. Biomed. Opt.* **17**, 061202 (2012).

119. Flock, S. T., Jacques, S. L., Wilson, B. C., Star, W. M. & van Gemert, M. J. C.

Optical properties of intralipid: A phantom medium for light propagation studies. *Lasers Surg. Med.* **12**, 510–519 (1992).

120. van Staveren, H. J., Moes, C. J. M., van Marie, J., Prahl, S. A. & van Gemert, M. J. C. Light scattering in lntralipid-10% in the wavelength range of 400–1100 nm. *Appl. Opt.* **30**, 4507 (1991).

121. Wang, X. *et al.* Noninvasive laser-induced photoacoustic tomography for structural and functional in vivo imaging of the brain. *Nat. Biotechnol.* **21**, 803–806 (2003).

122. Wang, L. V. Photoacoustic Imaging and Spectroscopy. *CRC Press* **144**, (2009).

123. Luke, G. P., Nam, S. Y. & Emelianov, S. Y. Optical wavelength selection for improved spectroscopic photoacoustic imaging. *Photoacoustics* **1**, 36–42 (2013).

124. Luke, G. P. & Emelianov, S. Y. Optimization of in vivo spectroscopic photoacoustic imaging by smart optical wavelength selection. *Opt. Lett.* **39**, 2214 (2014).

125. Schuman, J. S., Puliafito, C. A., Fujimoto, J. G. & Duker, J. S. *Optical Coherence Tomography of Ocular Diseases*. (2004).

126. Snider, E. J. *et al.* Improving Stem Cell Delivery to the Trabecular Meshwork Using Magnetic Nanoparticles. *Sci. Rep.* **8**, 12251 (2018).

127. Izatt, J. A. *et al.* Micrometer-Scale Resolution Imaging of the Anterior Eye In Vivo With Optical Coherence Tomography. *Arch. Ophthalmol.* **112**, 1584 (1994).

128. Silverman, R. H. High-resolution ultrasound imaging of the eye - a review. *Clin. Experiment. Ophthalmol.* **37**, 54–67 (2009).

129. Radhakrishnan, S. *et al.* Comparison of Optical Coherence Tomography and Ultrasound Biomicroscopy for Detection of Narrow Anterior Chamber Angles. *Arch. Ophthalmol.* **123**, 1053 (2005).

130. Radhakrishnan, S. *et al.* Real-Time Optical Coherence Tomography of the Anterior Segment at 1310 nm. *Arch. Ophthalmol.* **119**, 1179 (2001).

131. Hoerauf, H. *et al.* First Experimental and Clinical Results With Transscleral Optical Coherence Tomography. *Ophthalmic Surgery, Lasers Imaging Retin.* **31**, 218–222 (2000).

132. Hoerauf, H. *et al.* Transscleral Optical Coherence Tomography. *Arch. Ophthalmol.* **120**, 816 (2002).

133. Jiao, S. *et al.* Photoacoustic ophthalmoscopy for in vivo retinal imaging. *Opt. Express* **18**, 3967 (2010).

134. Song, W. *et al.* Integrating photoacoustic ophthalmoscopy with scanning laser

ophthalmoscopy, optical coherence tomography, and fluorescein angiography for a multimodal retinal imaging platform. *J. Biomed. Opt.* **17**, 061206 (2012).

135. Hariri, A. *et al.* In vivo photoacoustic imaging of chorioretinal oxygen gradients. *J. Biomed. Opt.* **23**, 1 (2018).

136. Ricles, L. M., Nam, S. Y., Treviño, E. A., Emelianov, S. Y. & Suggs, L. J. A dual gold nanoparticle system for mesenchymal stem cell tracking. *J. Mater. Chem. B* **2**, 8220–8230 (2014).

137. Donnelly, E. M., Kubelick, K. P., Dumani, D. S. & Emelianov, S. Y. Photoacoustic Image-Guided Delivery of Plasmonic-Nanoparticle-Labeled Mesenchymal Stem Cells to the Spinal Cord. *Nano Lett.* **18**, 6625–6632 (2018).

138. Kim, T., Lemaster, J. E., Chen, F., Li, J. & Jokerst, J. V. Photoacoustic Imaging of Human Mesenchymal Stem Cells Labeled with Prussian Blue–Poly(l -lysine) Nanocomplexes. *ACS Nano* **11**, 9022–9032 (2017).

139. Chung, E., Nam, S. Y., Ricles, L. M., Emelianov, S. Y. & Suggs, L. J. Evaluation of gold nanotracers to track adipose-derived stem cells in a PEGylated fibrin gel for dermal tissue engineering applications. *Int. J. Nanomedicine* **8**, 325–336 (2013).

140. Snider, E. J., Vannatta, R. T., Schildmeyer, L., Stamer, W. D. & Ethier, C. R. Characterizing differences between MSCs and TM cells: Toward autologous stem cell therapies for the glaucomatous trabecular meshwork. *J. Tissue Eng. Regen. Med.* **12**, (2018).

141. Turkevich, J., Stevenson, P. C. & Hillier, J. A study of the nucleation and growth processes in the synthesis of colloidal gold. *Discuss. Faraday Soc.* **11**, 55–75 (1951).

142. Ricles, L. M., Nam, S. Y., Sokolov, K., Emelianov, S. Y. & Suggs, L. J. Function of mesenchymal stem cells following loading of gold nanotracers. *Int. J. Nanomedicine* **6**, 407–16 (2011).

143. Zucker, R. M., Massaro, E. J., Sanders, K. M., Degn, L. L. & Boyes, W. K. Detection of TiO2 nanoparticles in cells by flow cytometry. *Cytom. Part A* **77A**, 677–685 (2010).

144. Cook, J. R., Bouchard, R. R. & Emelianov, S. Y. Tissue-mimicking phantoms for photoacoustic and ultrasonic imaging. *Biomed. Opt. Express* **2**, 3193–3206 (2011).

145. Bhattacharya, S. K., Gabelt, B. T., Ruiz, J., Picciani, R. & Kaufman, P. L. Cochlin Expression in Anterior Segment Organ Culture Models after TGFβ2 Treatment. *Investig. Opthalmology Vis. Sci.* **50**, 551 (2009).

146. Bachmann, B., Birke, M., Kook, D., Eichhorn, M. & Lütjen-Drecoll, E. Ultrastructural and Biochemical Evaluation of the Porcine Anterior Chamber Perfusion Model. *Investig. Opthalmology Vis. Sci.* **47**, 2011 (2006).

147. Kubelick, KP, Snider, EJ, Ethier, CR, Emelianov, S. Photoacoustic properties of anterior ocular tissues. *J. Biomed. Opt.* **In Print**, (2019).

148. Cook, J. R., Dumani, D. S., Kubelick, K. P., Luci, J. & Emelianov, S. Y. Prussian blue nanocubes: multi-functional nanoparticles for multimodal imaging and image-guided therapy. in *SPIE Photonics West Symposium, Proc. SPIE 10064, Photons Plus Ultrasound: Imaging and Sensing* (2017).

149. Nam, S. Y., Ricles, L. M., Suggs, L. J. & Emelianov, S. Y. Nonlinear photoacoustic signal increase from endocytosis of gold nanoparticles. *Opt. Lett.* **37**, 4708–10 (2012).

150. Ricles, L. M., Nam, S. Y., Sokolov, K., Emelianov, S. Y. & Suggs, L. J. Function of mesenchymal stem cells following loading of gold nanotracers. *Int. J. Nanomedicine* **6**, 407–416 (2011).

151. Laffey, M., Kubelick, K., Donnelly, E. & Emelianov, S. Effects of freezing on mesenchymal stem cells labeled with gold nanoparticles. *Tissue Eng. Part C Methods*

152. McMenamin, P. G. & Steptoe, R. J. Normal anatomy of the aqueous humour outflow system in the domestic pig eye. *J. Anat.* **178**, 65–77 (1991).

153. Ruiz-Ederra, J. *et al.* The pig eye as a novel model of glaucoma. *Exp. Eye Res.* **81**, 561–569 (2005).

154. Su, J., Karpiouk, A., Wang, B. & Emelianov, S. Photoacoustic imaging of clinical metal needles in tissue. *J. Biomed. Opt.* **15**, 021309 (2010).

155. Wang, C. *et al.* Protamine Functionalized Single-Walled Carbon Nanotubes for Stem Cell Labeling and In Vivo Raman/Magnetic Resonance/Photoacoustic Triple-Modal Imaging. *Adv. Funct. Mater.* **22**, 2363–2375 (2012).

156. Yin, C. *et al.* Organic Semiconducting Polymer Nanoparticles for Photoacoustic Labeling and Tracking of Stem Cells in the Second Near-Infrared Window. *ACS Nano* **12**, 12201–12211 (2018).

157. Zheng, S. *et al.* Noninvasive photoacoustic and fluorescent tracking of optical dye labeled T cellular activities of diseased sites at new depth. *J. Biophotonics* **11**, e201800073 (2018).

158. Ricles, L. M., Nam, S. Y., Treviño, E. A., Emelianov, S. Y. & Suggs, L. J. A dual gold nanoparticle system for mesenchymal stem cell tracking. *J. Mater. Chem. B* **2**, 8220–8230 (2014).

159. Alkilany, A. M. *et al.* Cellular Uptake and Cytotoxicity of Gold Nanorods: Molecular Origin of Cytotoxicity and Surface Effects. *Small* **5**, 701–708 (2009).

160. Chen, Y.-S. *et al.* Enhanced thermal stability of silica-coated gold nanorods for photoacoustic imaging and image-guided therapy. *Opt. Express* **18**, 8867 (2010).

161. Latina, M. A., Sibayan, S. A., Shin, D. H., Noecker, R. J. & Marcellino, G. Q-switched 532-nm Nd:YAG laser trabeculoplasty (selective laser trabeculoplasty): A multicenter, pilot, clinical study. *Ophthalmology* **105**, 2082–2090 (1998).

162. Juzych, M. S. *et al.* Comparison of long-term outcomes of selective laser trabeculoplasty versus argon laser trabeculoplasty in open-angle glaucoma. *Ophthalmology* **111**, 1853–1859 (2004).

163. Ursea, R. & Silverman, R. H. Anterior-segment imaging for assessment of glaucoma. *Expert Rev. Ophthalmol.* **5**, 59–74 (2010).

164. Dakhal, K. *et al.* Ultrafast laser induced retinal degeneration model in macaque using adaptive optics. *J. Vis.* **19**, 14 (2019).

165. Selective laser trabeculoplasty for glaucoma treatment. *Lumenis* (2019).

166. Physician eduation: Learn how to perform MicroPulse Laser Trabeculoplasty (MLT). *IRIDEX* (2019).

167. Leahy, K. E. & White, A. J. Selective laser trabeculoplasty: current perspectives. *Clin Ophthalmol* **9**, 833–841 (2015).

168. Kubelick, KP, Snider, E, Karpiouk, A, Ethier, CR, & Emelianov, S. Ultrasound/Photoacoustic Imaging Platform to Expedite Development of Novel Glaucoma Treatments. *IEEE Int. Ultrason. Symp.* (2018).

169. Lindvall, O. & Kokaia, Z. Stem cells in human neurodegenerative disorders--time for clinical translation? *J. Clin. Invest.* **120**, 29–40 (2010).

170. Lindvall, O., Kokaia, Z. & Martinez-Serrano, A. Stem cell therapy for human neurodegenerative disorders–how to make it work. *Nat. Med.* **10**, S42–S50 (2004).

171. Boulis, N. M. *et al.* Translational stem cell therapy for amyotrophic lateral sclerosis. *Nat. Rev. Neurol.* **8**, 172–176 (2012).

172. Lunn, J. S. *et al.* Stem cell technology for the study and treatment of motor neuron diseases. *Regen. Med.* **6**, 201–213 (2011).

173. Glass, J. D. *et al.* Lumbar Intraspinal Injection of Neural Stem Cells in Patients with Amyotrophic Lateral Sclerosis: Results of a Phase I Trial in 12 Patients. *Stem Cells* **30**, 1144–1151 (2012).

174. Donnelly, E. M. ., Kubelick, K. P. ., Dumani, D. S. & Emelianov, S. Y. Photoacoustic Image-Guided Delivery of Plasmonic-Nanoparticle-Labeled Mesenchymal Stem Cells to the Spinal Cord. *Nano Lett.* **18**, 6625–6632 (2018).

175. Lamanna, J. J., Miller, J. H., Riley, J. P., Hurtig, C. V & Boulis, N. M. Cellular therapeutics delivery to the spinal cord: technical considerations for clinical application. *Ther. Deliv.* **4**, 1397–1410 (2013).

176. Lamanna, J. J. *et al.* Ferumoxytol Labeling of Human Neural Progenitor Cells for Diagnostic Cellular Tracking in the Porcine Spinal Cord with Magnetic Resonance Imaging. *Stem Cells Transl. Med.* **6**, 139–150 (2017).

177. Callera, F. & de Melo, C. M. T. P. Magnetic Resonance Tracking of Magnetically Labeled Autologous Bone Marrow CD34 $^{+}$ Cells Transplanted into the Spinal Cord via Lumbar Puncture Technique in Patients with Chronic Spinal Cord Injury: CD34 $^{+}$ Cells' Migration into the Injured Site. *Stem Cells Dev.* **16**, 461–466 (2007).

178. Chotivichit, A., Ruangchainikom, M., Chiewvit, P., Wongkajornsilp, A. & Sujirattanawimol, K. Chronic spinal cord injury treated with transplanted autologous bone marrow-derived mesenchymal stem cells tracked by magnetic resonance imaging: a case report. *J. Med. Case Rep.* **9**, 79 (2015).

179. Syková, E. & Jendelová, P. Magnetic Resonance Tracking of Transplanted Stem Cells in Rat Brain and Spinal Cord. *Neurodegener. Dis.* **3**, 62–67 (2006).

180. Netuka, D., Ostry, S., Belsan, T., Kramar, F. & Benes, V. Intraoperative MR imaging in a case of a cervical spinal cord lesion. *J. Neurosurg. Spine* **14**, 754–757 (2011).

181. Jolesz, F. A., Golby, A. J. & Orringer, D. A. Magnetic Resonance Image-Guided Neurosurgery. in *Intraoperative Imaging and Image-Guided Therapy* 451–463 (Springer New York, 2014). doi:10.1007/978-1-4614-7657-3_32

182. Duprez, T. P. *et al.* Intraoperative 3T MR Imaging for Spinal Cord Tumor Resection: Feasibility, Timing, and Image Quality Using a 'Twin' MR-Operating Suite. *Am. J. Neuroradiol.* **20**, 1547–1553 (2008).

183. Zhu, W. *et al.* Mn $^{2+}$ -Doped Prussian Blue Nanocubes for Bimodal Imaging and Photothermal Therapy with Enhanced Performance. *ACS Appl. Mater. Interfaces* **7**, 11575–11582 (2015).

184. Emelianov, S. Y., Li, P.-C. & O'Donnell, M. Photoacoustics for molecular imaging and therapy. *Phys. Today* **62**, 34–39 (2009).

185. Wang, L. V & Hu, S. Photoacoustic tomography: in vivo imaging from organelles to organs. *Science* **335**, 1458–62 (2012).

186. Paul, C., Samdani, A. F., Betz, R. R., Fischer, I. & Neuhuber, B. Grafting of human bone marrow stromal cells into spinal cord injury: a comparison of delivery methods. *Spine (Phila. Pa. 1976).* **34**, 328–34 (2009).

187. Raore, B. *et al.* Cervical Multilevel Intraspinal Stem Cell Therapy: Assessment of

Surgical Risks in Gottingen Minipigs. *Spine (Phila. Pa. 1976).* **36**, E164–E171 (2011).

188. Jänicke, R. U., Sprengart, M. L., Wati, M. R. & Porter, A. G. Caspase-3 is required for DNA fragmentation and morphological changes associated with apoptosis. *J. Biol. Chem.* **273**, 9357–9360 (1998).

189. Atherton, E., Logan, C. J. & Sheppard, R. C. Peptide synthesis. Part 2. Procedures for solid-phase synthesis using Nα-fluorenylmethoxycarbonylamino-acids on polyamide supports. Synthesis of substance P and of acyl carrier protein 65-74 decapeptide. *J. Chem. Soc. Perkin Trans. 1* 538–546 (1981). doi:10.1039/P19810000538

190. Riley, J. *et al.* Targeted Spinal Cord Therapeutics Delivery: Stabilized Platform and Microelectrode Recording Guidance Validation. *Stereotact. Funct. Neurosurg.* **86**, 67–74 (2008).

191. Wang, L. & Hu, S. Photoacoustic Tomography: in Vivo Imaging Fro Organelles To Organs. *Science (80-.).* **335**, 1458–1462 (2012).

192. Mehrmohammadi, M., Oh, J., Mallidi, S. & Emelianov, S. Y. Pulsed Magneto-motive Ultrasound Imaging Using Ultrasmall Magnetic Nanoprobes. *Mol. Imaging* **10**, 102–110 (2011).

193. Tyas, L., Brophy, V. A., Pope, A., Rivett, A. J. & Tavaré, J. M. Rapid caspase-3 activation during apoptosis revealed using fluorescence-resonance energy transfer. *EMBO Rep.* **1**, 266–270 (2000).

194. Razansky, D., Vinegoni, C. & Ntziachristos, V. Multispectral photoacoustic imaging of fluorochromes in small animals. *Opt. Lett.* **32**, 2891 (2007).

195. Zackrisson, S., Van De Ven, S. M. W. Y. & Gambhir, S. S. Light In and Sound Out: Emerging Translational Strategies for Photoacoustic Imaging. (2014). doi:10.1158/0008-5472.CAN-13-2387

196. Dragulescu-Andrasi, A., Kothapalli, S.-R., Tikhomirov, G. A., Rao, J. & Gambhir, S. S. Activatable Oligomerizable Imaging Agents for Photoacoustic Imaging of Furin-Like Activity in Living Subjects. *J. Am. Chem. Soc.* **135**, 11015–11022 (2013).

197. Wang, L. V. & Yao, J. A practical guide to photoacoustic tomography in the life sciences. *Nature Methods* **13**, 627–638 (2016).

198. Mehier-Humbert, S., Bettinger, T., Yan, F. & Guy, R. H. Plasma membrane poration induced by ultrasound exposure: Implication for drug delivery. *J. Control. Release* **104**, 213–222 (2005).

199. Hallam, K. A., Donnelly, E. M., Karpiouk, A. B., Hartman, R. K. & Emelianov, S.

Y. Laser-activated perfluorocarbon nanodroplets: a new tool for blood brain barrier opening. *Biomed. Opt. Express* **9**, 4527 (2018).

200. Hess, K. L., Medintz, I. L. & Jewell, C. M. Designing inorganic nanomaterials for vaccines and immunotherapies. *Nano Today* (2019). doi:10.1016/j.nantod.2019.04.005

201. Bachmann, M. F. & Jennings, G. T. Vaccine delivery: A matter of size, geometry, kinetics and molecular patterns. *Nature Reviews Immunology* **10**, 787–796 (2010).

202. Swartz, M. A., Hubbell, J. A. & Reddy, S. T. Lymphatic drainage function and its immunological implications: From dendritic cell homing to vaccine design. *Seminars in Immunology* **20**, 147–156 (2008).

203. Reddy, S. T., Rehor, A., Schmoekel, H. G., Hubbell, J. A. & Swartz, M. A. In vivo targeting of dendritic cells in lymph nodes with poly(propylene sulfide) nanoparticles. *J. Control. Release* **112**, 26–34 (2006).

204. Gerner, M. Y., Torabi-Parizi, P. & Germain, R. N. Strategically Localized Dendritic Cells Promote Rapid T Cell Responses to Lymph-Borne Particulate Antigens. *Immunity* **42**, 172–185 (2015).

205. Santiesteban, D. Y., Dumani, D. S., Profili, D. & Emelianov, S. Y. Copper Sulfide Perfluorocarbon Nanodroplets as Clinically Relevant Photoacoustic/Ultrasound Imaging Agents. *Nano Lett.* **17**, 5984–5989 (2017).

206. Kroemer, G. *et al.* Classification of cell death: Recommendations of the Nomenclature Committee on Cell Death 2009. *Cell Death and Differentiation* **16**, 3–11 (2009).

207. Wei, C. *et al.* Magnetomotive photoacoustic imaging: in vitro studies of magnetic trapping with simultaneous photoacoustic detection of rare circulating tumor cells. *J. Biophotonics* **6**, 513–22 (2013).

208. Demissie, A., VanderLaan, D., Islam, M. S., Emelianov, S. & Dickson, R. Synchronously Amplified Photoacoustic Image Recovery (SAPhIRe). *Submitted* (2019).

209. Yoon, S. J. Photoacoustic Imaging using Nanoclusters. *UT Diss.* (2014).